THESIS

INVESTIGATION OF CHIRAL PORPHYRIN AGGREGATES WITH HETERODYNE-DETECTED VIBRATIONAL SUM FREQUENCY GENERATION SPECTROSCOPY

Submitted by

Kathryn A. Lindberg

Department of Chemistry

In partial fulfillment of the requirements

For the Degree of Master of Science

Colorado State University

Fort Collins, Colorado

Fall 2018

Master's Committee:

Advisor: Amber Krummel

Nancy Levinger
Justin Sambur
Martin Gelfand

ABSTRACT

INVESTIGATION OF CHIRAL PORPHYRIN AGGREGATES WITH HETERODYNE-DETECTED VIBRATIONAL SUM FREQUENCY GENERATION SPECTROSCOPY

In nature, photosynthetic organisms harvest and transport solar energy through the finely-tuned interplay between vibrational, electronic, and excitonic characteristics within photosynthetic reaction centers. These characteristics depend intimately on the precise arrangement of the reaction centers' molecular building blocks. Further knowledge of the relationship between structure and function in these natural systems is key to advancing synthetic solar technologies like dye-sensitized solar cells and artificial photosynthesis. Photosynthetic pigments, such as chlorophyll and bacteriochlorophyll, are of particular interest since their absorptive role is the first step in the solar harvesting process. Porphyrins, a group of macrocyclic organic compounds closely related to these pigments, have gained attention as simpler models for their more complicated natural counterparts. Tetra(4-sulfonatophenyl) porphyrin (TSPP), which closely resembles bacteriochlorophyll, is particularly valuable because it forms molecular aggregates analogous to the highly quantum-efficient light-harvesting "antennae" present in green sulfur bacteria chlorosomes. Imaging and spectroscopic studies indicate that the helical nanotubular TSPP aggregates are chiral and have distinct exciton contributions along different axes. However, the precise arrangement of TSPP monomers within the aggregate walls is still debated, prompting further, more detailed studies. Heterodyne-detected vibrational sum frequency generation (HD-VSFG) spectroscopy is a phase-sensitive, second-order nonlinear technique which probes the vibrational characteristics of

noncentrosymmetric molecular environments. HD-VSFG experiments can also probe excitonic and vibronic characteristics via experimental double resonance. By use of polarization conditions, theoretical modeling, and computational fitting, detailed information on the orientation of vibrational, vibronic, and excitonic transition dipoles can be extracted from HD-VSFG spectra. This work presents doubly-resonant HD-VSFG spectra of TSPP thin films drop-cast on gold, which demonstrates the technique's sensitivity to the relationship between complex phase and excitonic versus monomeric characteristics. HD-VSFG is then used to compare spectra of TSPP thin films prepared from racemic and chiral aqueous solutions. This comparison includes a polarization condition sensitive to only chiral environments, further demonstrating HD-VSFG as a valuable tool in the structural investigation of TSPP aggregates.

ACKNOWLEDGEMENTS

To Amber, for helping me grow a thick skin yet taking care not to break me in the process. Thank you for recognizing my strengths and pruning my weaknesses, and for offering support and compassion when I struggled. I truly appreciate it. I will miss having you as my boss lady.

To Chris Rich, for seeing me through the transformation from a scared first year to a researcher confident enough to stand on her own two legs. Thank you for being a patient teacher and for mentoring me in your own quiet way. I will always look up to you.

To Max and Kat, for making me feel like a part of the group as early as visitation weekend. Thank you for helping me find my research home and for supporting me through all the grad school hurdles. May your paths take you to wonderful places.

To Yusef, for taking up the SFG baton. Thank you for always being a kind and positive presence. Frustrating dilemmas in the lab were not nearly as bad with you around. I know you'll take excellent care of the table, just as I know your enthusiasm for science will take you far.

To everyone in the Krummel group, for making it possible to learn ultrafast spectroscopy without a single drop of previous experience. Thank you for being teachers and learners for all of us. Don't ever change that.

To Evan, for being the seatbelt on my emotional rollercoaster. Thank you for sharing my joyous times and bracing me in my most fragile moments, for keeping me on track when motivation waned and distractions beckoned, and for never hesitating to support my decisions when they were the right ones to make. Your genuine curiosity about my work brought us together and I'll never forget that. Thank you for being you.

To my parents and my brothers, for supporting my decision to move halfway across the country and study things that are intimidating to even pronounce. Just letting me share my passion with you, regardless of how much you understand it, means more than you know. Thank you for everything you've done that's gotten me where I am today, and for visiting every so often to make sure I stayed sane.

To my precious cat, Snickerdoodle, for never failing to warm my lap while I worked. Your love and companionship are the best antidepressants. Thank you for always returning to my side.

DEDICATION

This work is dedicated to the pursuit of knowledge. The more I learn, the more I realize I don't know. May this text help its readers take a step forward, no matter how small, in their own pursuits.

TABLE OF CONTENTS

ABSTRACT ii

ACKNOWLEDGEMENTS iv

DEDICATION vi

LIST OF FIGURES x

DEFINITION OF TERMS xi

Chapter 1: Introduction 1

1.1 Reaction Centers and Pigments 1

1.2 Light-Matter Interactions and Structure 4

1.3 Polarization Conditions in HD-VSFG 8

References 10

Chapter 2: Materials & Methods 13

2.1 Chemical Sample Preparation 13

2.2 Linear Spectral Data Acquisition & Processing 14

2.3 Ultrafast Spectrometer Setup & Spectral Acquisition 16

2.4 HD-VSFG Spectral Processing 19

References 23

Chapter 3: Linear Spectroscopy of TSPP Aggregates 24

3.1 Electronic Structure of Porphyrin Aggregates 24

3.2 pH-Dependence of TSPP UV-Vis Spectra 26

3.3 ATR-FTIR Spectra of TSPP Thin Films 29

References 32

Chapter 4: Phase Acrobatics: The Influence of Excitonic Resonance and Gold Nonresonant Background on Heterodyne-Detected Vibrational Sum Frequency Generation Emission 34

Disclaimer 34

4.1 Introduction 34

4.2 HD-VSFG Experimental Setup and TSPP Sample System 35

4.3 Theory on Resonance and Phase in HD-VSFG 39

4.4 HD-VSFG Results and Discussion 43

4.5 Conclusion 50

4.7 Supporting Information 50

References 58

Chapter 5: HD-VSFG Comparison of Racemic- and Chiral-Prepared TSPP Thin Films 61

5.1 Introduction 61

5.2 Absorptive and Dispersive Features 61

5.3 Comparison of Racemic and Chiral Thin Films 63

5.4 HD-VSFG Results & Discussion 66

5.5 Conclusion 72

References 75

Appendix: Python Scripts 76

ATR-FTIR & UV-Vis Spectral Processing 76

HD-VSFG Fourier Filtering 77

List of Selected Abbreviations 85

LIST OF FIGURES

1.1 Bacteriochlorophyll *a* and TSPP....3
1.2 STM of TSPP nanotubes....3
1.3 SFG energy transitions....7
1.4 Isotropic vs. ordered distributions....7
2.1 20x images and ATR-FTIR of TSPP aggregate thin film....15
2.2 HD-VSFG spectrometer schematic....17
2.3 HD-VSFG raw spectrum and temporal interferogram....20
2.4 HD-VSFG filtered spectrum and normalized spectrum....22
3.1 Gouterman model x- and y- porphyrin axes....25
3.2 TSPP protonation conformational change....25
3.3 pH-dependent UV-Vis of aqueous TSPP....28
3.4 ATR-FTIR of TSPP aggregate thin film....31
4.1 TSPP diacid and aggregate Q-bands and postulated aggregate structure....38
4.2 HD-VSFG PPP and SSP spectra of TSPP aggregate thin film....44
4.3 PPP spectrum phase acrobatics....46
4.4 SSP spectrum phase acrobatics....47
4.5 Homodyne-detected SFG spectrum of bare gold....52
4.6 HD-VSFG spectrometer diagram....52
4.7 Representative Fourier filtering plots....54
4.8 Complex refractive index of aqueous TSPP....56
4.9 Electronic resonance phase spectrum....56
4.10 Phased and non-phased HD-VSFG spectra of TSPP....57
5.1 Simple HD-VSFG of 0^o and 90^o phase offsets....62
5.2 Simple HD-VSFG of 180^o and 270^o phase offsets....64
5.3 PPP HD-VSFG spectra of racemic and chiral thin films....67
5.4 SSP HD-VSFG spectra of racemic and chiral thin films....68
5.5 PSP HD-VSFG spectra of racemic and chiral thin films....70
5.6 Racemic and chiral $\left|\chi^{(2)}\right|^2$ comparisons....73

DEFINITION OF TERMS

B-band: Strong ultraviolet-region absorption band characteristic of porphyrin spectra arising from the S_0-S_2 electronic transition.

Blue shift: Change in an observed spectral feature towards shorter wavelengths (higher frequencies).

Centrosymmetric: Environment which has an inversion center.

Chiral: Molecule or aggregate which is non-superimposable on its mirror image.

Diacid: Porphyrin with a fully-protonated, cationic core.

Double resonance: HD-VSFG experiment in which incident electric fields are resonant with the energies of two separate vibrational or electronic excited states in the sample.

Exciton: Delocalized electronic excitation across monomer units in an aggregate arising from transition dipole coupling.

Fourier filtering: Data processing method for isolating sample signal from local oscillator contribution in HD-VSFG spectra.

Free base: Porphyrin with a neutral core, having only two protonated nitrogens.

Heterodyne detection: Method of spectral detection in which the sample HD-VSFG signal is detected collinearly with a time-delayed local oscillator.

Isotropic distribution: Molecular environment with uniformity in all orientations.

Local oscillator: Non-resonant sum frequency signal generated for heterodyne detection.

P-polarized: Light which has been polarized parallel to the laser table surface.

Porphyrin: Group of organic compounds with cores consisting of four pyrroles connected by methane bridges at their α carbons.

Q-bands: Weak visible-region absorption bands characteristic of porphyrin spectra, arising from the electronically-forbidden, vibronically-allowed S_0-S_1 electronic transitions.

Q-switched: Laser composed of pulses with higher peak power than a continuous wave laser and shorter duration than an ultrafast laser.

Racemic: Containing equal amounts of dextro- and levo-enantiomers of a chiral molecule or aggregate.

Red shift: Change in an observed spectral feature towards longer wavelengths (lower frequencies).

S-polarized: Light which has been polarized perpendicular to the laser table surface.

Second-order nonlinear susceptibility, $\chi^{(2)}$: Third-rank tensor describing the molecular response of a system in the x-, y-, and z-directions in an HD-VSFG experiment.

Ti:Sapphire: Titanium-doped Sapphire ($Ti:Al_2O_3$) crystal.

Vibronic: Interaction between electronic and nuclear vibrational motion.

Zwitterion: Molecule with separate cationic and anionic locations.

Chapter 1: Introduction

1.1 Reaction Centers and Pigments

In nature, photosynthetic organisms harvest solar energy via complex photosynthetic reaction centers (PRCs).[1] Pigments, molecules which begin the photosynthetic process by absorbing light from the sun, are an integral component of PRCs. The energy from the absorbed light is then transferred through intricate mechanisms in the PRC and ultimately converted into usable energy for the organism, completing the photosynthetic process. Further understanding of these highly efficient natural light-harvesting systems and their pigments directly benefits the continued development and improvement of synthetic solar technology.[2,3] However, a thorough understanding of the structure and function of these natural systems can be hindered by their sheer variety and complexity. Thus, there is great interest in advancing scientific understanding of these systems through the application of advanced analytical techniques to suitable model systems.[4,5]

Photosynthetic organisms such as plants, algae, and cyanobacteria employ a variety of different pigment molecules depending on the organism's needs.[6] Chlorophylls, bacteriochlorophylls, and carotenoids are examples of photosynthetic pigment families which absorb solar energy.[7,8] Although these pigment families share a role in photosynthesis, their structure and characteristics have evolved in accordance with their organisms' environments, resulting in a wide range of different molecular structures. The general structure of these natural pigments has been well documented.[9,10] However, it is also important to understand their detailed vibrational characteristics and electronic structure. Transportation and conversion of absorbed solar energy into other usable energy forms is governed by the vibrational characteristics and

electronic structure of not only the photosynthetic pigment molecules, but also the arrangement of pigment molecules in the supramolecular aggregates that the molecules form in the PRCs.[5,11,12] In these aggregates, pigment molecules are the building blocks for larger structures which enhance the PRC's ability to capture and transfer solar energy. For example, in green sulfur bacteria (GSB), bacteriochlorophyll pigment molecules are found in nanoscopic aggregates in the PRC, which are dubbed "solar antennae" for their long, rod-like shape.[13] The antennae are theorized to be a key reason behind GSB's incredible solar efficiency. These structures are fined-tuned such that, upon absorption of a photon, the resulting vibrational and electronic responses in the aggregates can funnel the photon's energy to the next step in the photosynthetic process. Thus, in the pursuit of more efficient synthetic solar technologies, it is important to understand the structure of light-harvesting molecules and their aggregates.

As previously stated, photosynthetic pigments like bacteriochlorophylls are highly diverse and their structures are often very complex. While the diversity and complexity of each unique pigment no doubt serves an evolutionary advantage for each organism, it renders the molecules extremely difficult to study with techniques that could determine their detailed structure. Therefore, simpler model compounds that mimic the structure and function of their more complicated natural counterparts are extremely valuable for research purposes.[2] One such model is tetra(4-sulfonatophenyl)porphyrin (henceforth referred to as TSPP), a member of the well-studied porphyrin family. Porphyrins resemble the molecular cores of their chlorophyll and bacteriochlorophyll cousins (**Figure 1.1**).[2,14] TSPP bears a striking resemblance to bacteriochlorophyll *a*, a major absorptive pigment in GSB. In acidic conditions, TSPP molecules self-aggregate into nanotubular structures that closely resemble the solar "antennae" found in GSB PRCs.[15] These TSPP nanotubes have been characterized extensively by imaging

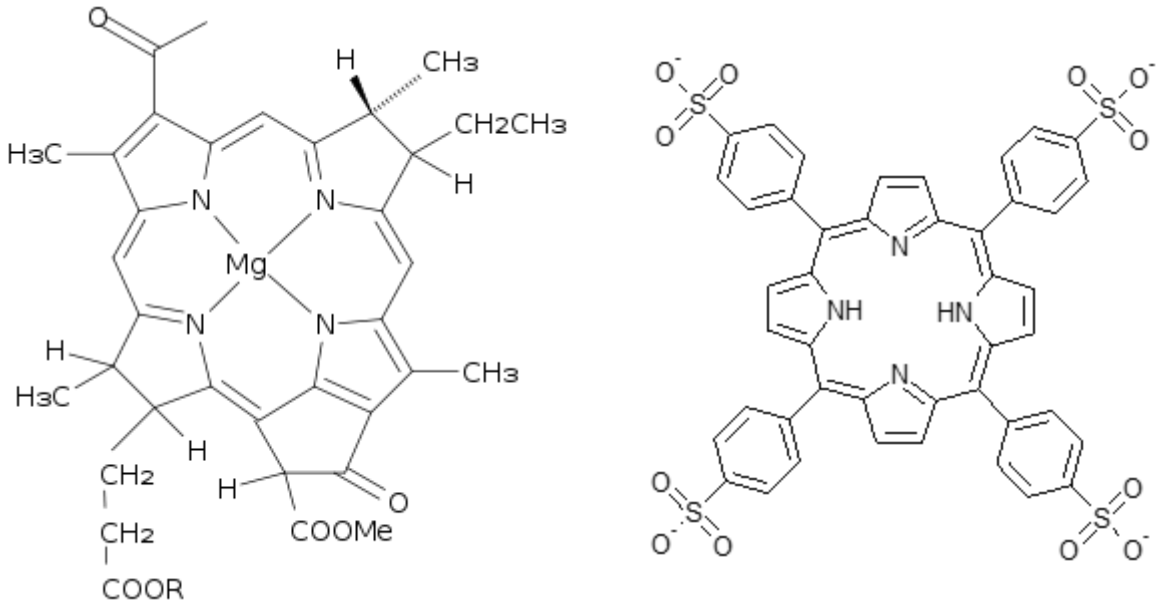

Figure 1.1 Bacteriochlorophyll *a* (left, *R* = phytane), and tetra(4-sulfonatophenyl)porphyrin (TSPP, right).

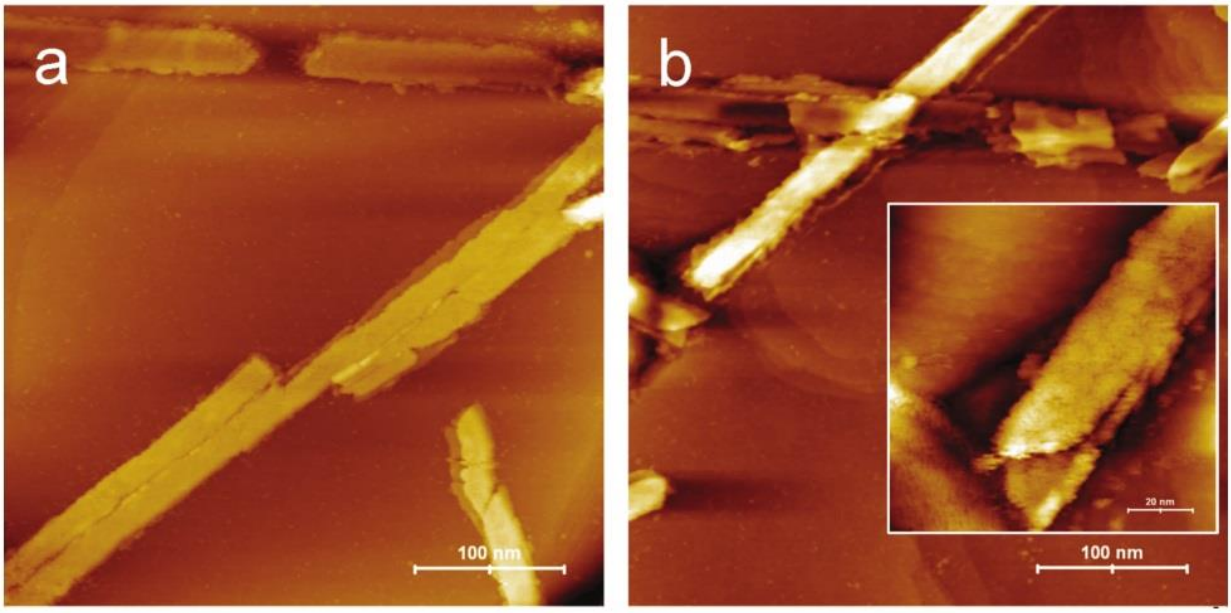

Figure 1.2 Scanning tunneling microscopy images of collapsed TSPP nanotubes on a gold surface.[16]

techniques. Scanning tunneling microscopy (STM, **Figure 1.2**)[16] and atomic force microscopy (AFM)[17] reveal that the aggregates have a highly consistent shape and width. The next step towards understanding the link between structure and function is to investigate the molecular-level structure of the aggregates. How the molecules are arranged within the aggregate determines aggregate vibrational characteristics and electronic structure. Consequently, molecular arrangement directly impacts energy transport mechanisms. Therefore, it is necessary to continue the investigation with analytical techniques capable of discerning more detailed information.

1.2 Light-Matter Interactions and Structure

Spectroscopic techniques are capable of shedding light on detailed molecular structure. Spectroscopy is broadly defined as the study of the quantum-mechanical interactions between light and matter. Different wavelengths of light interact in different ways with molecules; analysis of how that light is changed by those interactions yields rich structural information. Infrared light, for example, is converted into vibrational energy when absorbed by a molecule. Molecular bonds of differing strength and atomic composition absorb different wavelengths of infrared light. Fourier-transform infrared (FTIR) spectroscopy is a common analytical technique that uses these vibrational properties to determine molecular composition of samples. Similarly, ultraviolet-visible (UV-Vis) spectroscopy probes electronic structural information because absorption of ultraviolet or visible light typically changes the way electron density on a molecule is arranged.

Spectroscopic techniques like FTIR,[18] Raman spectroscopy,[19] and UV-Vis[20] have been used extensively to study the TSPP aggregate system. Despite providing important

complimentary information to what has been established by imaging techniques, these spectroscopies still lack the ability to determine the exact molecular structure of the aggregates; thus, nonlinear spectroscopies have become the next step in the investigation. Nonlinear spectroscopies utilize multiple high-intensity electromagnetic fields, typically in the form of ultrafast pulsed lasers, to extract quantitative molecular-level information from chemical systems. The nonlinear technique used in this body of work is heterodyne-detected vibrational sum frequency generation spectroscopy (HD-VSFG).[21]

HD-VSFG uses both visible and infrared (IR) laser pulses to probe specific structures in chemical samples. "Heterodyne-detected" refers to the way signal is detected in the experiment. Instead of only detecting the signal generated by the sample, the signal is combined with a local oscillator (LO). The LO is an SFG signal generated in a nonlinear crystal; this signal is virtually identical no matter what wavelengths are used to produce it and is typically much stronger than the signal from the sample. The LO amplifies the signal from the sample, making it easier to detect. More importantly, the interference between signal and LO preserves valuable phase information which helps to determine the orientation of the sample molecules. "Vibrational" refers to the fact that the technique probes vibrational characteristics of the sample.

"Sum frequency generation" refers to the way in which signal is generated in an HD-VSFG experiment. The visible and IR pulses in the experiment are designed to encounter the sample in the same place and at the same time. Therefore, absorption of the visible and IR photons occurs simultaneously. The IR photon initiates an energy transition to a vibrationally-excited state within the molecule. Then, the visible photon promotes the molecule to an excited electronic state, after which the molecule relaxes back to its ground electronic and vibrational states. This latter series of transitions is identical to an anti-Stokes Raman experiment. The

relaxation from high to low energy levels causes emission of a new photon (**Figure 1.3**). The frequency of the emitted photon is equal to the sum of the frequencies of the incident visible and IR photons. For example, in a VSFG experiment where 790 nm visible light and 6.5 μm IR light (frequencies of 12 660 cm^{-1} and 1540 cm^{-1}, respectively) are used, a signal at 704 nm (14 200 cm^{-1}) is detected.

Generation of HD-VSFG signal involves simultaneous IR and Raman vibrational transitions. Fourier-transform infrared (FTIR) spectroscopy and Raman spectroscopy encompass a majority of linear vibrational spectroscopic studies and are generally considered to be mutually exclusive due to vibrational symmetry-based transition rules.[22] This holds true for centrosymmetric molecules and environments. A molecule is said to be centrosymmetric if it has a central point through which all other points in the molecule can be transcribed an equal distance to the other side and, in doing so, recreate an exact replica of the original molecule. This central point is called an inversion center. Bulk sample environments are centrosymmetric if the molecules in the bulk are isotropically distributed (**Figure 1.4**). In a centrosymmetric chemical system, IR-active vibrational modes are not Raman-active, and vice versa. Environments that do not have an inversion center are non-centrosymmetric and are the exception to this rule; in this case, both IR and Raman transitions are allowed. Therefore, SFG, which involves simultaneous IR and Raman transitions, can only occur in non-centrosymmetric environments.

SFG is often employed as an interface-selective nonlinear technique because it requires both IR and Raman activity in a vibrational mode.[23,24] At an interface (liquid-liquid, air-solid, liquid-air, etc.), molecules can be arranged differently than in the bulk because of their interaction with the interface. The presence of an interface breaks the centrosymmetry seen in the bulk sample (Figure 1.4). However, SFG signal does not solely arise from interfaces. In some

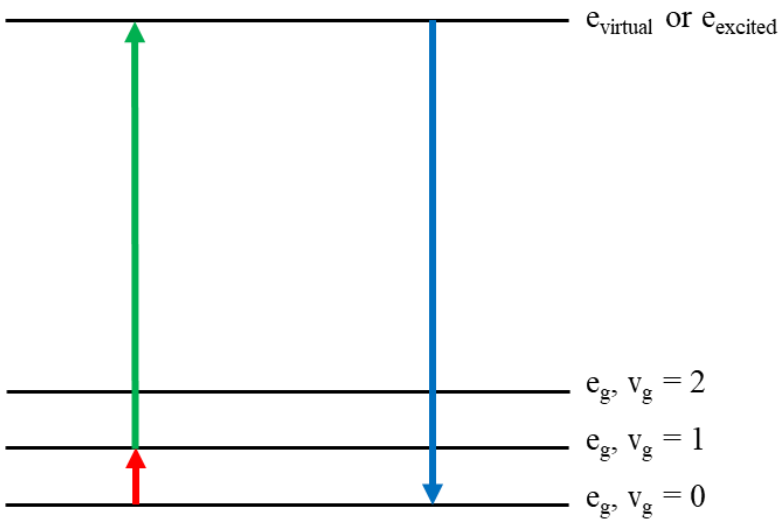

Figure 1.3 Energy transitions in SFG. IR (red) and visible (green) promote system to a virtual or excited electronic state. SFG signal (blue) is emitted upon relaxation back to the ground state.

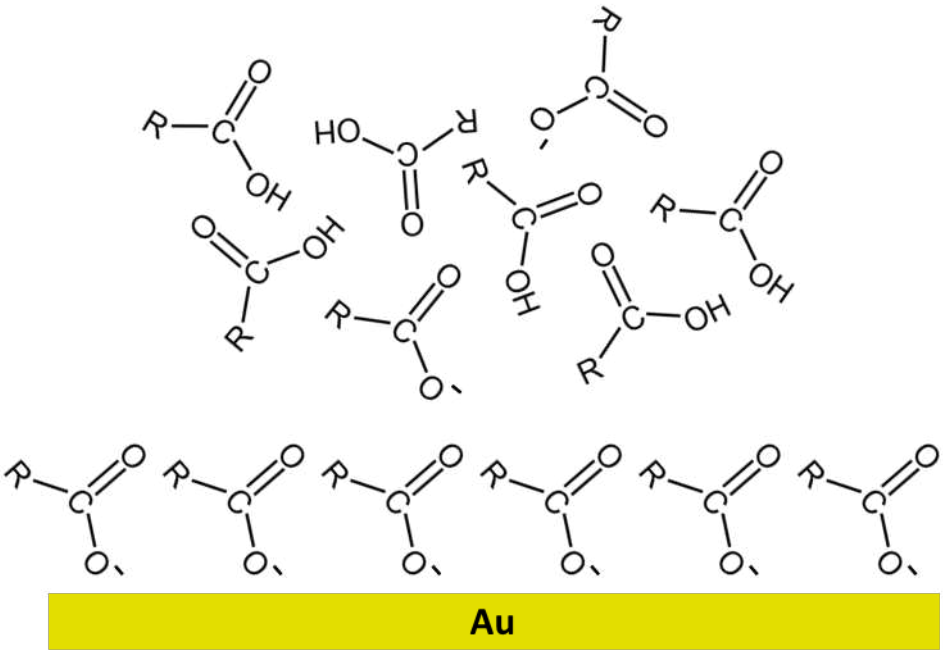

Figure 1.4 Simplified depiction of isotropic molecular distribution in a bulk sample (top) compared to ordered orientation at a gold surface (bottom).

cases, SFG signal can be generated in the bulk. This occurs when the arrangement of molecules in the bulk does not create an overall centrosymmetric environment. Aggregation, like in a TSPP nanotube, creates order within the bulk. TSPP aggregate nanotubes do not possess an inversion center; therefore, SFG signal from bulk aggregates is allowed. Furthermore, TSPP nanotubes are chiral.[19] That is, a mirror image of a TSPP nanotube cannot be superimposed in any way upon the original. As discussed in the next section, SFG is also particularly useful for probing chiral compounds and the unique properties associated with their chirality.

1.3 Polarization Conditions in HD-VSFG

The usefulness of HD-VSFG goes far beyond its non-centrosymmetric-specific properties. At interfaces, the technique can determine the absolute orientation of molecules. For example, it has been used to determine the orientation of *cis*-bis(isothiocyanato) bis(2,2′-bipyridyl-4,4′-dicarboxylato) ruthenium(II), or N3 dye, on gold and TiO_2 surfaces.[25] The results contribute information towards a better understanding of why N3 is an excellent dye for dye-sensitized solar cells. HD-VSFG is also capable of probing structural information along different axes in the TSPP aggregate system. The technique employs polarization conditions to access this information. In spectroscopy, it is often advantageous to control the polarization of the light sources used in the experiment. On the HD-VSFG laser table, laser pulses are set to oscillate either parallel (P) or perpendicular (S) to the table surface. The polarization of the IR and visible laser pulses can be set independently. Likewise, while the VSFG signal can consist of both P and S polarized light, the detection scheme is set to receive only one or the other.

Structure and orientation information is gained by careful selection of different polarization combinations of the IR, visible, and VSFG signal pulses. The vibrational and

electronic responses of a molecule, or an aggregate as is the case with TSPP, directly correspond to the direction in which the incident IR and visible EM waves are oscillating. The second-order nonlinear susceptibility, $\chi^{(2)}$, of the aggregate is a three-dimensional matrix which describes the VSFG response in each x, y, and z direction that arises from incident IR and visible light in each direction.[26] Different polarization combinations will probe different components of $\chi^{(2)}$. In an experiment where the IR and visible pulses are both P polarized, the experiment initiates vibrational and electronic responses in the same direction along the aggregate. Conversely, with P polarized IR light and S polarized visible light, the vibrational and electronic responses are perpendicular to each other. These two experiments probe different components of $\chi^{(2)}$. Furthermore, there are certain $\chi^{(2)}$ components which are only present in chiral systems. Specific chiral-only polarization conditions are used to probe these components in chiral molecules or aggregates like TSPP.[27] Chiral VSFG experiments on chiral compounds provide even more detailed spectroscopic information to be used for structural determination.

The components of the $\chi^{(2)}$ tensor are directly dependent on the vibrational characteristics and electronic structure of the sample. Calculated spectra based on theoretical aggregate exciton models are key to deciphering $\chi^{(2)}$ information from experimental HD-VSFG spectra.[28] By finding the calculated structure which best replicates experimental signal strength, phase, peak location, and other characteristics resulting from different polarization combinations, it is possible to determine the structure of the real sample. In this work, FTIR, UV-Vis, and HD-VSFG experiments were performed on thin film samples of TSPP aggregates with this goal in mind.

References

(1) Allen, J. P.; Williams, J. C. Photosynthetic Reaction Centers. *FEBS Lett.* **1998**, *438*, 5–9.

(2) Otsuki, J. Supramolecular Approach towards Light-Harvesting Materials Based on Porphyrins and Chlorophylls. *J. Mater. Chem. A* **2018**, *6* (16), 6710–6753.

(3) Brédas, J.; Sargent, E. H.; Scholes, G. D. Photovoltaic Concepts Inspired by Coherence Effects in Photosynthetic Systems. *Nat. Mater.* **2017**, *16* (1), 35–44.

(4) Cook, L. P.; Brewer, G.; Wong-ng, W. Structural Aspects of Porphyrins for Functional Materials Applications. *Crystals* **2017**, *7* (223), 1–22.

(5) Brixner, T.; Hildner, R.; Köhler, J.; Lambert, C.; Würthner, F. Exciton Transport in Molecular Aggregates – From Natural Antennas to Synthetic Chromophore Systems. *Adv. Energy Mater.* **2017**, *7*, 1–33.

(6) Ruban, A. V. Evolution under the Sun: Optimizing Light Harvesting in Photosynthesis. *J. Exp. Bot.* **2015**, *66* (1), 7–23.

(7) Richhariya, G.; Kumar, A.; Tekasakul, P.; Gupta, B. Natural Dyes for Dye Sensitized Solar Cell : A Review. *Renew. Sustain. Energy Rev.* **2017**, *69* (November 2016), 705–718.

(8) Günther, L. M.; Jendrny, M.; Bloemsma, E. A.; Tank, M.; Oostergetel, G. T.; Bryant, D. A.; Knoester, J.; Köhler, J. Structure of Light-Harvesting Aggregates in Individual Chlorosomes. *J. Phys. Chem. B* **2016**, *120* (24), 5367–5376.

(9) Senge, M. O.; Ryan, A. A.; Letchford, K. A.; MacGowan, S. A.; Mielke, T. Chlorophylls, Symmetry, Chirality, and Photosynthesis. *Symmetry (Basel).* **2014**, *6* (3), 781–843.

(10) Boichenko, V. A. Photosynthetic Units of Phototrophic Organisms. *Biochem.* **2004**, *69* (5), 581–596.

(11) Mirkovic, T.; Ostroumov, E. E.; Anna, J. M.; Van Grondelle, R.; Govindjee; Scholes, G. D. Light Absorption and Energy Transfer in the Antenna Complexes of Photosynthetic Organisms. *Chem. Rev.* **2017**, *117* (2), 249–293.

(12) Linnanto, J. M.; Korppi-Tommola, J. E. I. Investigation on Chlorosomal Antenna Geometries: Tube, Lamella and Spiral-Type Self-Aggregates. *Photosynth. Res.* **2008**, *96* (3), 227–245.

(13) Orf, G. S.; Blankenship, R. E. Chlorosome Antenna Complexes from Green Photosynthetic Bacteria. *Photosynth. Res.* **2013**, *116*, 315–331.

(14) Gouterman, M.; Wagnière, G. H.; Snyder, L. C. Spectra of Porphyrins: Part II. Four Orbital Model. *J. Mol. Spectrosc.* **1963**, *11* (1), 108–127.

(15) Schwab, A. D.; Smith, D. E.; Rich, C. S.; Young, E. R.; Smith, W. F.; de Paula, J. C.; Paula, J. C. De; de Paula, J. C. Porphyrin Nanorods. *J. Phys. Chem. B* **2003**, *107* (41), 11339–11345.

(16) Friesen, B. a.; Rich, C. C.; Mazur, U.; McHale, J. L. Resonance Raman Spectroscopy of Helical Porphyrin Nanotubes. *J. Phys. Chem. C* **2010**, *114* (39), 16357–16366.

(17) Schwab, A. D.; Smith, D. E.; Bond-Watts, B.; Johnston, D. E.; Hone, J.; Johnson, A. T.; De Paula, J. C.; Smith, W. F. Photoconductivity of Self-Assembled Porphyrin Nanorods. *Nano Lett.* **2004**, *4* (7), 1261–1265.

(18) Zhang, Y.-H.; Chen, D.-M.; He, T.; Liu, F.-C. Raman and Infrared Spectral Study of Meso-Sulfonatophenyl Substituted Porphyrins (TPPSn, N=1, 2A, 2O, 3, 4). *Spectrochim. Acta Part A Mol. Biomol. Spectrosc.* **2003**, *59* (1), 87–101.

(19) Wan, Y.; Stradomska, A.; Fong, S.; Guo, Z.; Schaller, R. D.; Wiederrecht, G. P.; Knoester, J.; Huang, L. Exciton Level Structure and Dynamics in Tubular Porphyrin Aggregates. *J. Phys. Chem. C* **2014**, *118* (43), 24854–24865.

(20) Leishman, C. W.; McHale, J. L. Morphologically Determined Excitonic Properties of Porphyrin Aggregates in Alcohols with Variable Acidity. *J. Phys. Chem. C* **2016**, *120* (28), 15496–15508.

(21) Stiopkin, I. V; Jayathilake, H. D.; Bordenyuk, A. N.; Benderskii, A. V. Heterodyne-Detected Vibrational Sum Frequency Generation Spectroscopy. *J. Am. Chem. Soc.* **2008**, *130* (2), 2271–2275.

(22) Harris, D. C.; Bertolucci, M. D. Vibrational Spectroscopy: Infrared and Raman Spectra. In *Symmetry and Spectroscopy: An Introduction to Vibrational and Electronic Spectroscopy*; Dover Publications, 1989; pp 93–100.

(23) Hung, K.-K.; Stege, U.; Hore, D. K. IR Absorption, Raman Scattering, and IR-Vis Sum-Frequency Generation Spectroscopy as Quantitative Probes of Surface Structure. *Appl. Spectrosc. Rev.* **2014**, *4928* (October), 00–00.

(24) Jubb, A. M.; Hua, W.; Allen, H. C. Environmental Chemistry at Vapor / Water Interfaces: Insights from Vibrational Sum Frequency Generation Spectroscopy. *Annu. Rev. Phys. Chem.* **2012**, *63*, 107–130.

(25) Rich, C. C.; Mattson, M. A.; Krummel, A. T. Direct Measurement of the Absolute Orientation of N3 Dye at Gold and Titanium Dioxide Surfaces with Heterodyne-Detected Vibrational SFG Spectroscopy. *J. Phys. Chem. C* **2016**.

(26) Lambert, A. G.; Davies, P. B.; Neivandt, D. J. Implementing the Theory of Sum Frequency Generation Vibrational Spectroscopy: A Tutorial Review. *Appl. Spectrosc. Rev.* **2005**, *40*, 103–145.

(27) Okuno, M.; Ishibashi, T. A. Chirality Discriminated by Heterodyne-Detected Vibrational Sum Frequency Generation. *J. Phys. Chem. Lett.* **2014**, *5* (16), 2874–2878.

(28) Vlaming, S. M.; Augulis, R.; Stuart, M. C. A.; Knoester, J.; Van Loosdrecht, P. H. M. Exciton Spectra and the Microscopic Structure of Self-Assembled Porphyrin Nanotubes. *J. Phys. Chem. B* **2009**, *113* (8), 2273–2283.

Chapter 2: Materials & Methods

2.1 Chemical Sample Preparation

Meso-tetra(4-sulfonatophenyl)porphine dihydrochloride (TSPP diacid salt) was acquired from Frontier Scientific. Aqueous TSPP diacid was prepared by dissolving the appropriate mass of TSPP diacid salt in deionized (DI) water for the desired concentration in a volumetric flask and inverting several times to ensure mixing. Samples were prepared in the 5-100 μM range. In this range, resulting aqueous diacid samples have a blue-green color and a pH of approximately 4. At this pH the TSPP is assumed to be monomeric.

Aqueous TSPP free base was prepared by addition of sodium hydroxide to the aqueous diacid until a pH of at least 6 was reached. Above pH 6, the blue-green color of the diacid changes to a deep red color, indicating conversion of the porphyrin to its free-base form. Racemic mixtures of aqueous TSPP aggregates were prepared by addition of concentrated hydrochloric acid to the aqueous diacid until the pH was below 1. Below pH 1, a subtle color change from blue-green to green-yellow is observed. At this pH, the porphyrin is assumed to be fully protonated and aggregated. Chiral aqueous TSPP aggregates were prepared by addition of the appropriate mass of TSPP diacid salt to DI water in a beaker on a stir plate kept at a constant 700 rpm.[1] The solution was continuously stirred while concentrated hydrochloric acid was added to bring the pH below 1. The solution was left to stir for approximately 24 hours before stirring was stopped.

Liquid samples for ultraviolet-visible (UV-Vis) spectroscopy were prepared by the above-mentioned aqueous methods, then pipetted into plastic cuvettes for analysis. Thin film racemic and chiral aggregate samples for attenuated total reflection Fourier-transform infrared

(ATR-FTIR) spectroscopy and heterodyne-detected vibrational sum frequency generation (HD-VSFG) spectroscopy were prepared by the drop-cast method.[2,3] One to two pipette drops of aqueous racemic or chiral TSPP aggregate solutions were dropped onto the surface of a clean, unprotected gold mirror (ThorLabs PF10-03-M03). The droplets were left to air dry for approximately 24 hours with a large upturned beaker covering the mirror to prevent accumulation of dust on the surface. The resulting drop-cast films had an outer matte greenish "coffee ring" and a more reflective, greener inner area.

2.2 Linear Spectral Data Acquisition & Processing

UV-Vis spectra were acquired using a Thermo Scientific Evolution 300 UV-Vis spectrophotometer. Spectra were acquired with a 2 nm resolution in Absorbance mode. DI water was used as a blank before each sample measurement. Blank and samples were measured in plastic cuvettes. ATR-FTIR spectra were acquired using a Bruker FTIR spectrometer with an MCT detector and a Bruker ATR 20x objective at a resolution of 0.5 cm^{-1}. Microscope images were acquired with a Bruker Hyperion 3000. Measurement locations on the aggregate drop-cast samples were selected to acquire a representative sample set from visually different sample areas. The bare gold surface of the gold mirror was used to measure reference spectra. Linear spectra were processed using a custom Python script (Appendix I) and were self-normalized. No significant differences were seen between spectra acquired at different locations on the thin film, which is shown in **Figure 2.1**. Spectra were acquired at the edge of the film (2.1A) and several points in the center of the film (2.1B-D). Fringes due to gaseous water absorption can be seen in the region above 1300 cm^{-1} because the ATR-FTIR experimental setup did not allow for purging.

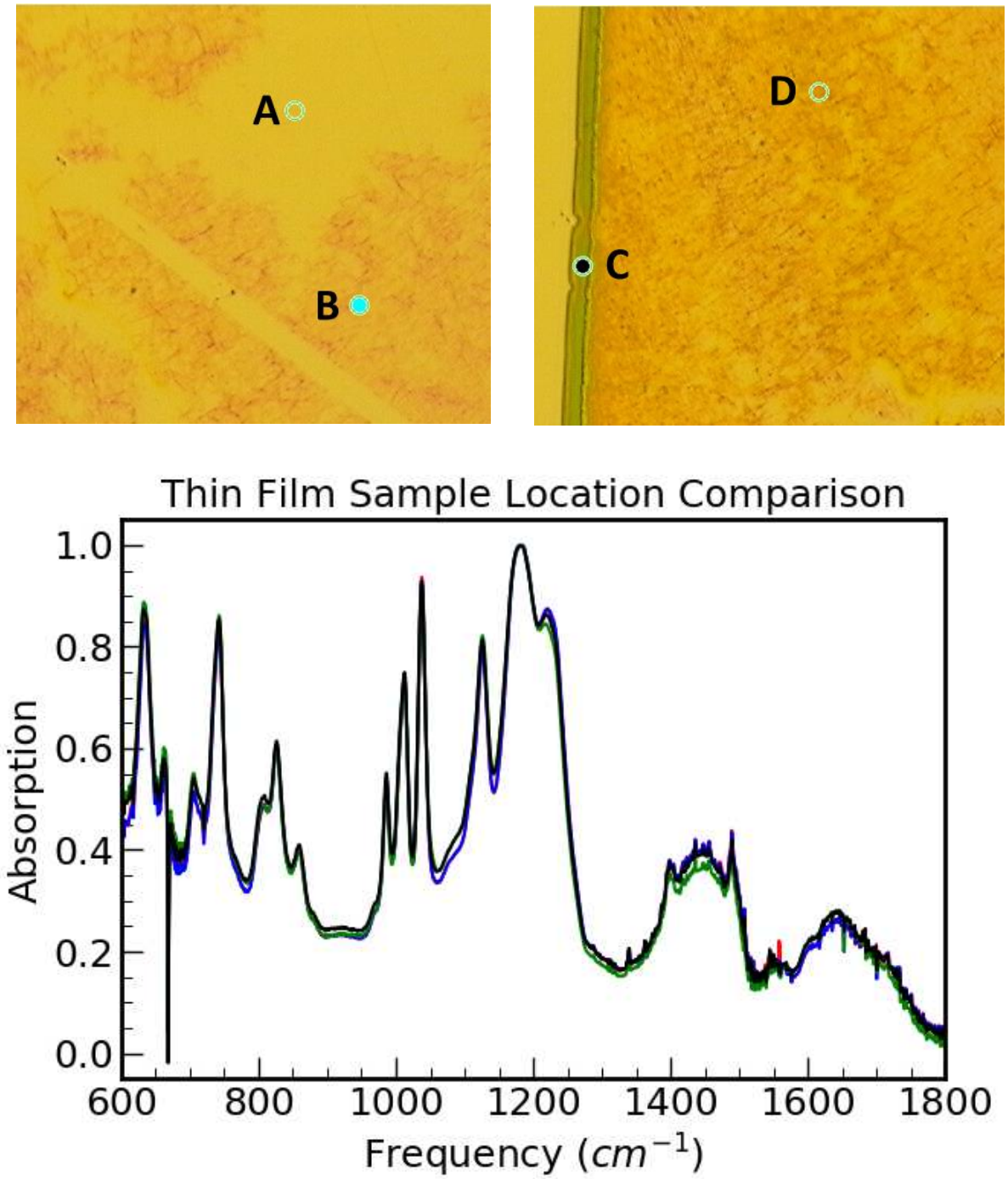

Figure 2.1 20x microscope images marked with ATR-FTIR spectral acquisition locations (top) and corresponding spectra (bottom). A = red, B = blue, C = black, D = green.

2.3 Ultrafast Spectrometer Setup & Spectral Acquisition

Heterodyne-detected vibrational sum frequency generation (HD-VSFG) spectra were acquired with a home-built ultrafast spectrometer (**Figure 2.2**).[4,5] A Ti:Sapphire Kerr-lens-modelocked oscillator (Griffin-W, KM Labs) pumped by a 532 nm, 3.50 W, continuous-wave (CW) laser (Sprout-H, Lighthouse Photonics) produces pulses centered at 790 nm with an average power of 250 mW. A Ti:Sapph regenerative amplifier (Wyvern-1000, KM Labs) pumped by a Q-switched Lee Laser (Coherent) is then used to amplify the pulses to 3.50 W at a repetition rate of 1 kHz. The resulting pulses are 45 fs in duration. After the regenerative amplifier, the pulse train is split by an 80/20 beam splitter.

The 80% leg is directed to a tunable optical parametric amplification system (TOPAS Prime, Light Conversion) which produces mid-infrared (IR) pulses centered at 6500 nm via difference frequency generation in a silver gallium selenide crystal. A computer-controlled precision translation stage is used to keep the timing of the IR pulses static. Next, the mid-IR passes through a half-waveplate and wire grid polarizer pair, which controls the polarization of the light. The last IR-only optic is an off-axis parabolic mirror with a focal length of 6 inches, which focuses the IR beam onto a 200 nm sputter-coated zinc oxide thin film on a 1 mm calcium fluoride window, where it meets with the visible line.

The visible line begins with the 20% leg transmitted through the post-regenerative amplifier beam splitter. The visible beam is directed along a length of the table equivalent to the distance traveled by the IR leg in the TOPAS system. Accounting for distance traveled assures temporal alignment of the visible and IR pulses. The visible line is then retroreflected on a manually-controlled translational stage, which can be adjusted for fine-tuning of temporal overlap between the IR and visible pulses at the sample location. Next, an interference filter

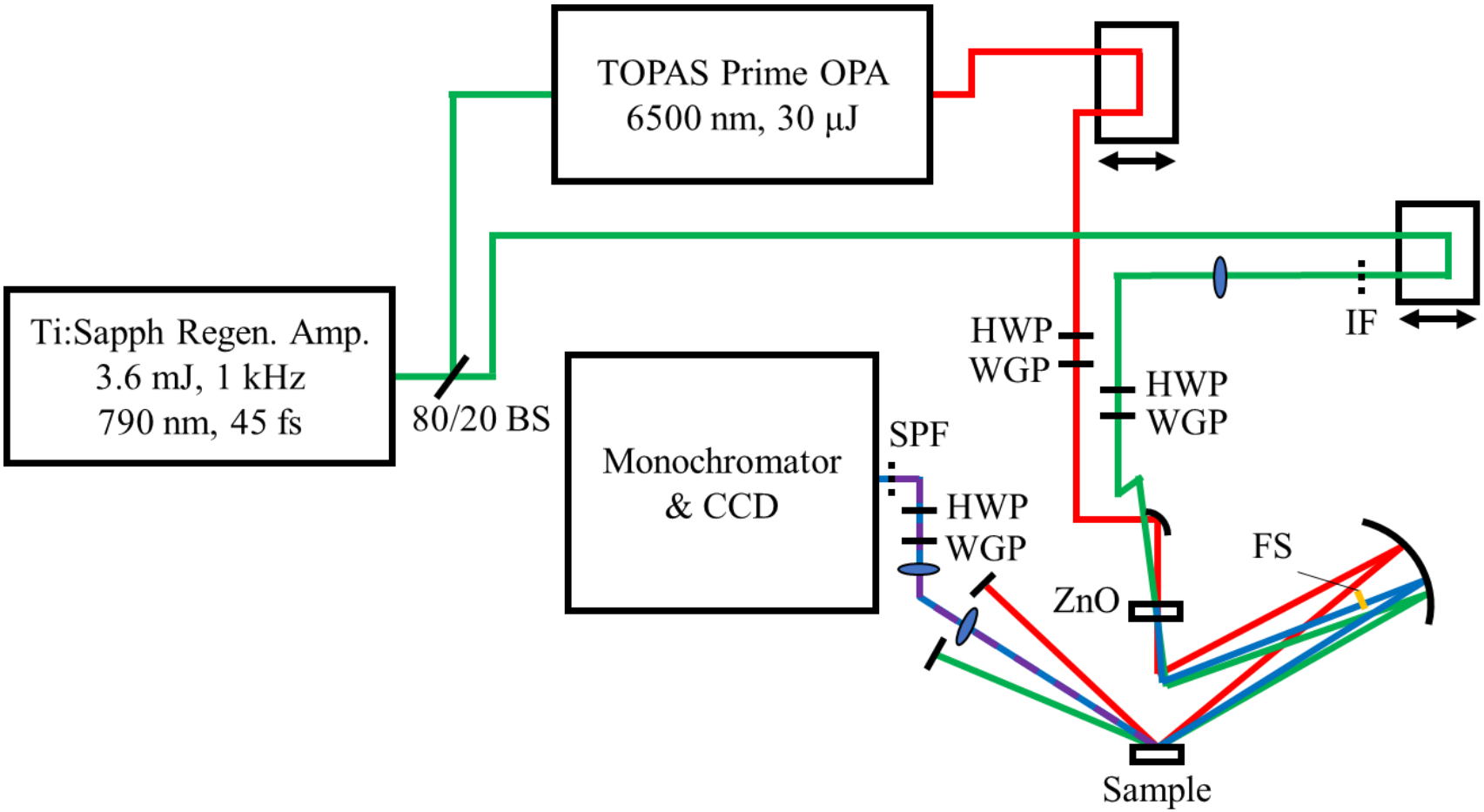

Figure 2.2 HD-VSFG spectrometer schematic. Wavelengths: visible = green, IR = red, LO = blue, VSFG signal = purple. Optics: BS = beam splitter; IF = interference filter; HWP = half waveplate; WGP = wire grid polarizer; ZnO = 200 nm zinc oxide thin film on calcium fluoride; FS = fused silica; SPF = short pass filter.

converts the broadband, temporally short visible pulse into a narrowband, temporally long visible pulse with a spectral FWHM of 10 cm^{-1}. The visible line then passes through a lens, a half-waveplate and wire grid polarizer pair, and finally is overlapped with the IR at the zinc oxide thin film. Here, non-resonant sum frequency signal is generated by spatial and temporal overlap of the IR and visible pulses in the zinc oxide film; this signal is henceforth referred to as the local oscillator (LO).[4,6]

The IR, visible, and LO are then reflected on to a 200 mm focal length curved mirror. Before the curved mirror, the LO passes through a 3 mm fused silica window which delays the LO pulses in time by 5 ps. The curved mirror focuses all three beams onto the sample surface, where SFG signal is generated collinearly with the temporally-delayed LO in a reflection geometry. The signal is then collimated and passed through a half waveplate and wire grid polarizer to control detected signal polarization and account for the monochromator (iHR550, Horiba) grating polarization bias. Residual visible line is blocked by a short-pass filter before the detector. Finally, the signal is spectrally resolved with either a 600 or 1200 line/mm grating by the monochromator and detected with a CCD camera (Synapse, Horiba).

The detector is calibrated with a neon lamp and comparison to a known neon emission spectrum. The visible pulse is measured before each experiment to determine FWHM and center frequency. The center frequency is then used to calculate the relative IR frequency of the detected SFG signal. SFG signal is produced at approximately 700 nm in these experiments; however, because the spectral features of interest are vibrational, we want to know the IR wavelength dependence of the signal. Thus, the relative IR frequencies are calculated by subtracting the visible frequency from the detected SFG frequencies.

2.4 HD-VSFG Spectral Processing

Raw spectral intensities are recorded for relative IR frequencies as described previously. Raw data is in the form of a spectral interferogram because the non-resonant local oscillator (LO) and sample sum frequency signal are detected collinearly and the LO is delayed in time by 5 ps. The raw spectra are processed with a custom Python code (Appendix I) using a Fourier Filtering process.[4] First, the raw spectrum (**Figure 2.3**) is converted to a temporal interferogram via Fast Fourier Transform (FFT). The temporal interferogram has a large DC component at the origin and a pair of smaller features at ±5 ps arising from the LO and sample signal, respectively. Fourier filtering is performed to isolate the signal feature. First, a time window which encapsulates the feature (typically approximately 3 to 6.5 ps) is chosen (**Figure 2.4**). The filtered interferogram is then transformed back into the frequency domain via inverse FFT. The resulting filtered spectrum is complex, having both real and imaginary components (Figure 2.4).

Spectral acquisition is repeated on a bare gold surface to be used as a reference. The Fourier filtering process is repeated for the raw gold reference spectrum. To account for phase differences between the sample and the gold reference, the filtered sample and reference spectral interferograms are plotted together and compared. Either the real or imaginary spectra of the sample and reference can be plotted as long as it is the same for both. Then a phase factor is chosen and applied to the complex sample spectrum to align the phase of the sample spectrum to the reference spectrum:

$$\chi_S^{(2)} = \chi_S^{(2)} \cdot e^{-i\phi_{offset}} \tag{1}$$

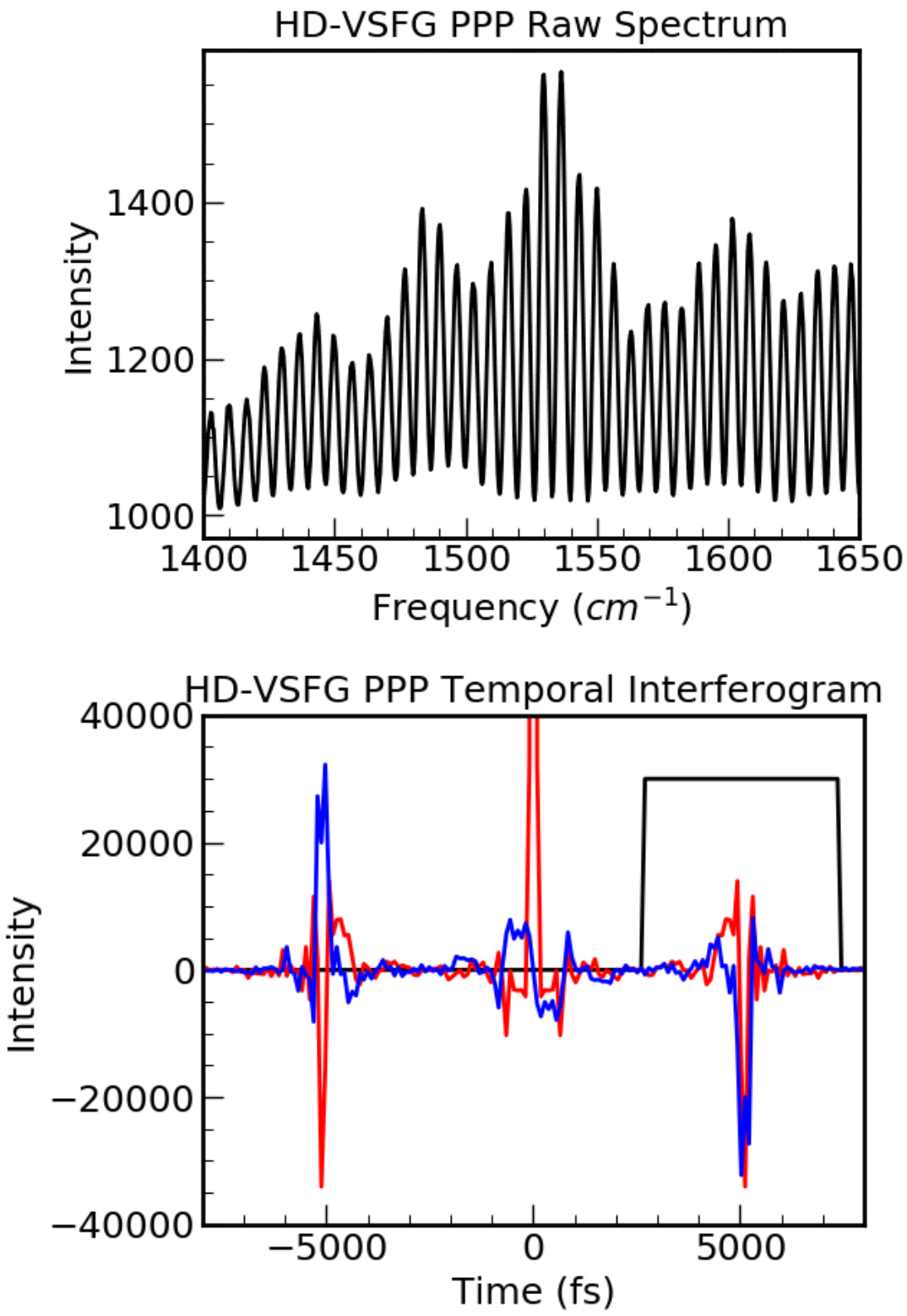

Figure 2.3 Raw TSPP sample spectral interferogram (top) and corresponding Fourier-transformed temporal interferogram (bottom). Real component = red, imaginary component = blue, Fourier Filtering window = black.

where $\chi_s^{(2)}$ is the complex sample signal and ϕ_{offset} is the observed phase offset between the filtered sample and reference spectra. Phase is compared in a spectral region where no sample features are present.

After the sample has been phased to the reference, the sample spectrum is normalized by dividing it by the reference spectrum. The resulting HD-VSFG spectrum (Figure 2.4) is representative of the complex $\chi^{(2)}$ tensor; thus, it is necessary to plot both the real and imaginary components of the spectrum for analysis. HD-VSFG spectra are baseline-corrected by calculating a linear fit for two frequency values at which no vibrational features are observed. The linear fit is then subtracted from the processed HD-VSFG spectrum, resulting in a baseline-corrected spectrum. Finally, the $|\chi^{(2)}|$ spectrum is calculated by squaring the absolute value of the baseline-corrected spectrum.

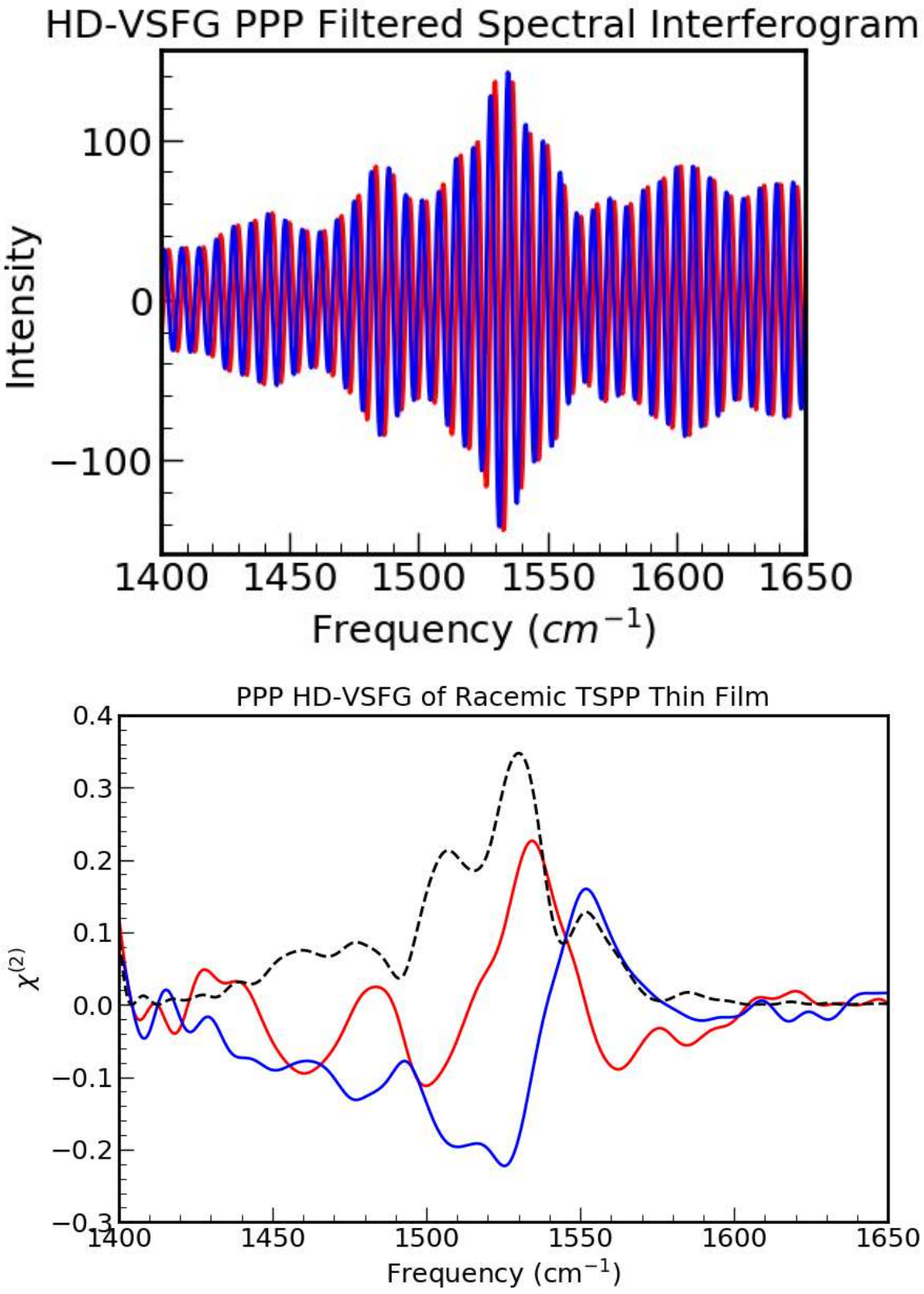

Figure 2.4 Fourier-filtered spectral interferogram of a TSPP sample (top) and normalized, baseline-corrected HD-VSFG spectrum (bottom). Real component = red, imaginary component = blue.

References

(1) Ohno, O.; Kaizu, Y.; Kobayashi, H. J-Aggregate Formation Aqueous Media of a Water-Soluble Porphyrin in Acidic. *J. Chem. Phys.* **1993**, *99* (September), 4128.

(2) Rotomskis, R.; Augulis, R.; Snitka, V.; Valiokas, R.; Liedberg, B. Hierarchical Structure of TPPS $_4$ J-Aggregates on Substrate Revealed by Atomic Force Microscopy. *J. Phys. Chem. B* **2004**, *108* (9), 2833–2838.

(3) Miura, A.; Shibata, Y.; Chosrowjan, H.; Mataga, N.; Tamai, N. Femtosecond Fluorescence Spectroscopy and Near-Field Spectroscopy of Water-Soluble Tetra(4-Sulfonatophenyl)Porphyrin and Its J-Aggregate. *J. Photochem. Photobiol. A Chem.* **2006**, *178* (2–3 SPEC. ISS.), 192–200.

(4) Yamaguchi, S.; Tahara, T. Heterodyne-Detected Electronic Sum Frequency Generation: "Up" versus "down" Alignment of Interfacial Molecules. *J. Chem. Phys.* **2008**, *129* (10), 1–4.

(5) Stiopkin, I. V; Jayathilake, H. D.; Bordenyuk, A. N.; Benderskii, A. V. Heterodyne-Detected Vibrational Sum Frequency Generation Spectroscopy. *J. Am. Chem. Soc.* **2008**, *130* (2), 2271–2275.

(6) Nihonyanagi, S.; Yamaguchi, S.; Tahara, T.; Nihonyanagi, S.; Yamaguchi, S. Direct Evidence for Orientational Flip-Flop of Water Molecules at Charged Interfaces : A Heterodyne-Detected Vibrational Sum Frequency Generation Study. **2015**, *204704* (2009).

Chapter 3: Linear Spectroscopy of TSPP Aggregates

Attenuated total reflection Fourier-transform infrared (ATR-FTIR) and ultraviolet-visible (UV-Vis) spectra of TSPP were obtained by the methods described in Chapter 2. These techniques were used to confirm linear electronic and vibrational properties of the TSPP system and to compare the results to those published in the literature. UV-Vis spectra were taken of TSPP at different pHs to observe spectral changes upon protonation and aggregation of the molecule. ATR-FTIR spectra were collected to observe TSPP infrared vibrational responses in the spectral region of interest.

3.1 Electronic Structure of Porphyrin Aggregates

The electronic structure of porphyrins has been a subject of much interest for over half a century. Gouterman's simple yet comprehensive 1961 review of porphyrin spectra established a model for porphyrin electronic structure that is still used to this day.[1] The Gouterman model hypothesizes that the distinct pattern of features observed in different porphyrin spectra arises from transitions between the two HOMO and two LUMO states of the molecule. The electronically-allowed S_0-S_2 transition results in the observed B (or Soret) spectral bands. The porphyrin B-band is a strong feature seen in the ultraviolet region. The weaker set of Q-bands in the visible region arise from electronically-forbidden, vibronically-allowed S_0-S_1 transitions. The electronic and vibronic transitions occur in both the x- and y- directions, where the x-axis is defined as the axis intersecting the protonated nitrogens in a free-base porphyrin (**Figure 3.1**). Addition of substituents as well as changes in the protonation state of the porphyrin lead to

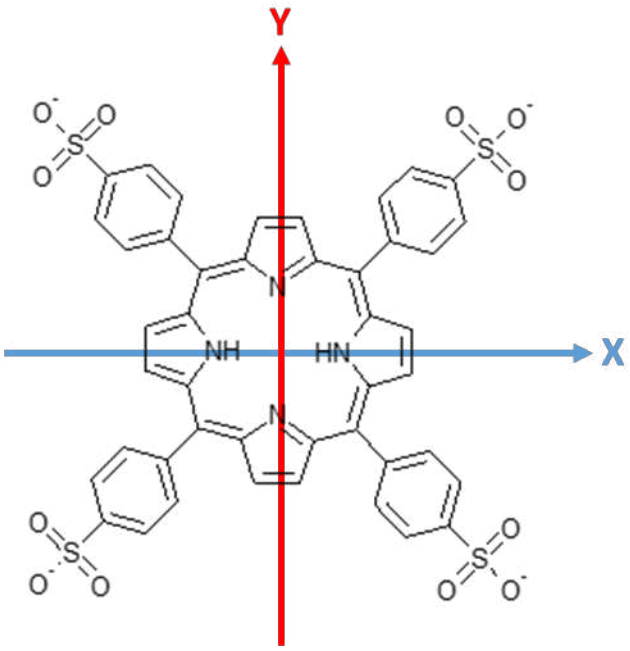

Figure 3.1 Free-base TSPP with corresponding Gouterman model x- and y-axes.

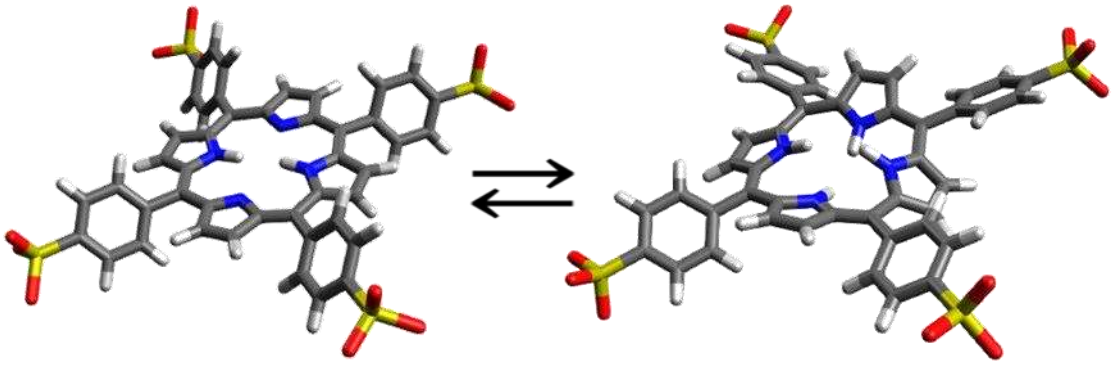

Figure 3.2 Illustration of conformational change in a TSPP monomer upon protonation of the free base (left) to create the diacid (right). Steric hindrance between hydrogens causes the "saddling" shape change.

symmetry changes in the molecule and thus shifts in energy of the four molecular orbitals involved in the B and Q bands. Subsequently, the spectral bands will shift. The conformational change upon protonation of the TSPP monomer is shown in **Figure 3.2** as an example.

Aggregation also has a significant effect on electronic structure. In an aggregate, molecules are close enough together for excitonic coupling to occur. Excitonic coupling is a result of individual molecular electronic transition dipoles interacting with each other along the aggregate, thus creating an exciton—an electronic state extending along the aggregate.[2] The contributions of the excitons to aggregate spectra depend on the arrangement of its monomer components. In an aggregate with a purely H-aggregate conformation, where transition dipoles are arranged parallel to one another, the spectral feature of the resulting exciton will occur at a higher energy than that of the monomer. In a purely J-aggregate conformation, with transition dipoles arrange head-to-head, the excitonic feature will occur at a lower energy. Monomers in real aggregates are rarely, if ever, aligned perfectly parallel or head-to-head. Thus, both H- and J-type features are typically present at different strengths depending on monomer orientation.

The presence of the discussed porphyrin and aggregate spectral features provide information on the symmetry, protonation, aggregation, and excitonic nature of TSPP aggregates. The observation of these contributions is discussed in the following section.

3.2 pH-Dependence of TSPP UV-Vis Spectra

UV-Vis spectra of aqueous TSPP were acquired at 25 different pH points, descending from 11.26 to 0.39. The purpose of this comparison was to observe the distinct spectral differences between the free base (only two protonated central nitrogens), diacid (fully

protonated central nitrogens), and aggregate forms of the TSPP molecule. Representative pH points are shown to best illustrate spectral changes.

No change in absorption was observed from pH 11.26 to 6.70. In this range, the aqueous TSPP is present as a free base. In the ultraviolet region, the strong free base B-band arising from the allowed S_0-S_2 transition is present at 413 nm. In the visible region, four weaker free base Q-bands appear at 516 nm, 550 nm, 583 nm, and 634 nm. These features are consistent with established literature results.[3,4]

As the pH of the solution was lowered, features indicative of the TSPP diacid begin to appear, as shown in **Figure 3.3**. At pH 6.70, the solution displays only free-base (FB) features as described above. At pH 5.51, the FB B-band at 413 nm loses intensity and the diacid B-band appears at 434 nm. The FB Q-bands also lose intensity as the diacid Q-bands grow in at 543 nm, 591 nm, and 644 nm. The shift from four FB to three diacid Q-bands is due to the molecular change in symmetry. As a free base, the x- and y-axes in the TSPP molecule are not equivalent due to the differing nitrogen protonation states. As a diacid, protonation of the second nitrogen pair increases the molecular symmetry and degeneracy in two of the vibronic transitions, reducing the number of Q-band features by one. Furthermore, it has been shown that upon diacid protonation of the TSPP core, steric hindrance causes the molecule to saddle. This conformational change leads to the observed spectral shifts.

FB features continue to decrease and diacid features continue to grow as the pH is further lowered. The first sign of aggregate features appears at pH 4.48 with a small peak at 490 nm. The diacid B- and Q-bands are strongest at pH 3.00, but the aggregate features can also clearly be seen. The 490 nm peak arises from the B-band of the TSPP J-aggregate exciton. J-aggregates, as described in the previous section, will have spectral features at lower energies

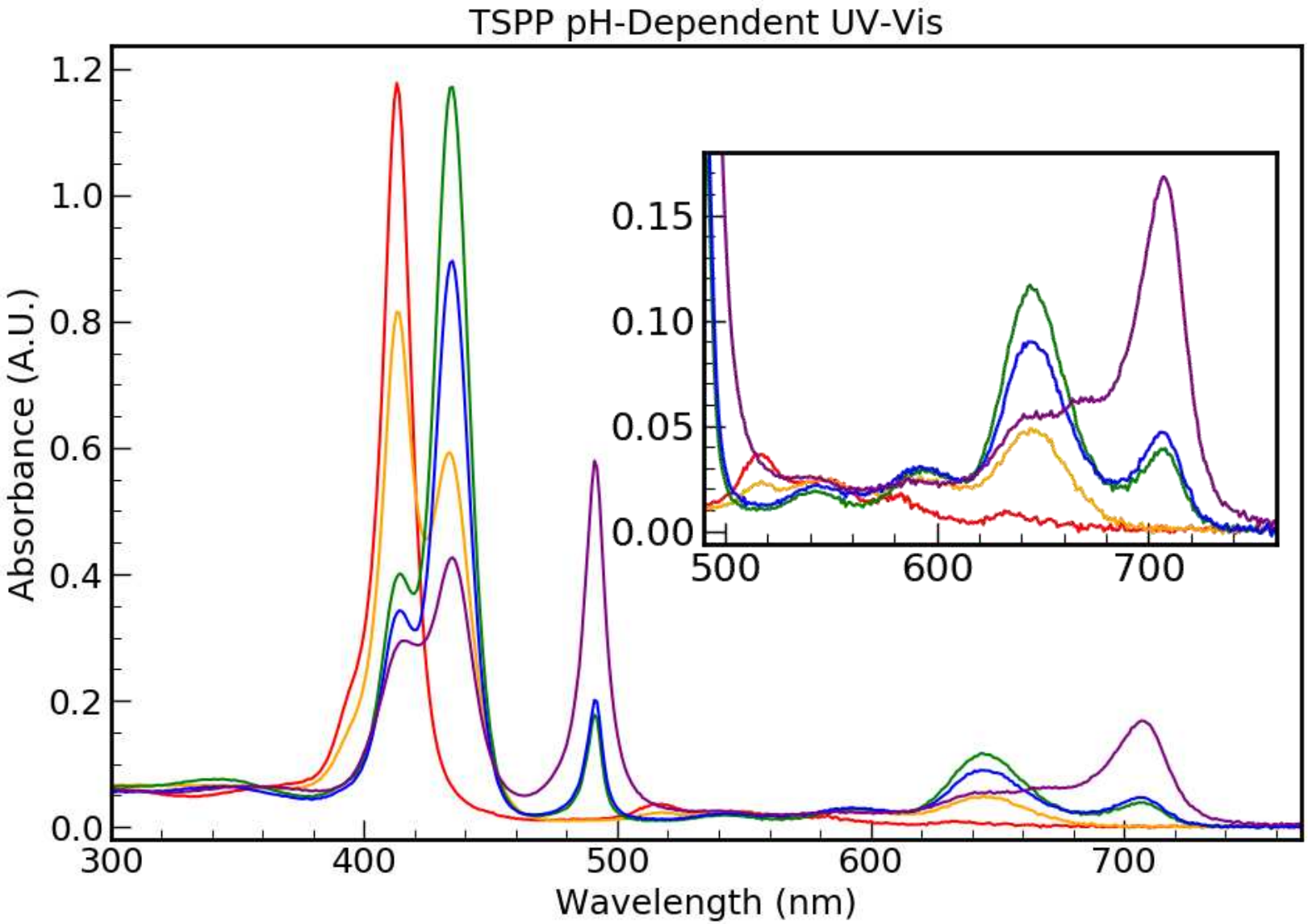

Figure 3.3 pH-dependent UV-Vis spectra of aqueous TSPP. pH values: 6.70 = red, 5.50 = orange, 3.00 = green, 1.31 = blue, 0.39 = purple. Inset: Q-band porphyrin features in the visible region.

compared to the associated monomer. This is clearly shown in the aggregate B-band at 490 nm as compared to the non-aggregated diacid B-band at 434 nm. The same is shown in the Q-band. A lower energy Q-band feature begins to grow in at 707 nm as the aggregate is formed. At pH 1.31, the diacid and FB features continue to lose strength in favor of the aggregate features. By pH 0.39, although FB and monomer diacid features are still present, the sharp 490 nm aggregate B-band and broad 707 nm Q-band have peaked in intensity.

These spectral changes are indicative of the changes occurring at the molecular level. The decrease in FB features and increase in diacid features as the solution is made more acidic shows the increasing presence of fully-protonated TSPP molecules in the solution. Aggregate features appear almost immediately after the diacid is present.[5] It has been shown that TSPP aggregates will continue to form in diacid solutions even at moderate pH levels when given enough time. In this experiment, spectra were obtained within one to two hours from titration of the solution, so aggregate formation due to time was assumed to be minimal. In increasingly acidic conditions, more FB is converted to diacid; the increased presence of the zwitterionic diacid species consequently results in an increase in aggregate presence. These observations are consistent with the observations reported in the literature.[5–7]

3.3 ATR-FTIR Spectra of TSPP Thin Films

TSPP is highly Raman active and thus has been extensively studied with Raman spectroscopies in pursuit of vibrational information.[8–13] While high Raman activity typically corresponds with low IR activity and vice versa, the HD-VSFG spectroscopy used in this study requires that the system possess modes with both Raman and IR activity; thus, it is important that IR activity is also investigated.

Thin films of TSPP aggregates were prepared on a gold mirror as described in Chapter 2. The films were observed with the ATR 20x microscope objective to select spots for spectral acquisition. Although the films were visually different in the center versus at the edge, no significant differences were observed in the FTIR spectra; see Figure 2.1 for comparison of spectra. **Figure 3.4** shows a representative ATR-FTIR spectrum of a TSPP thin film. Interference from atmospheric water absorption is observed in the higher-frequency region because the experimental setup did not allow for purging. The fingerprint region below 1300 cm^{-1} is densely populated with features; however, the region of interest in the nonlinear spectroscopic study described in the following chapters is approximately 1350 cm^{-1} to 1800 cm^{-1}, where several smaller features can be seen. These features arise from macrocycle C=C vibrations with transition dipole moments oriented in the plane of the TSPP porphyrin core. Broad features at approximately 1445 cm^{-1}, 1552 cm^{-1}, and 1642 cm^{-1}, as well as a sharper peak at 1490 cm^{-1}, were observed consistently in spectra recorded in different areas on the thin film sample. These vibrational features can be seen in the HD-VSFG results discussed in the following chapters.

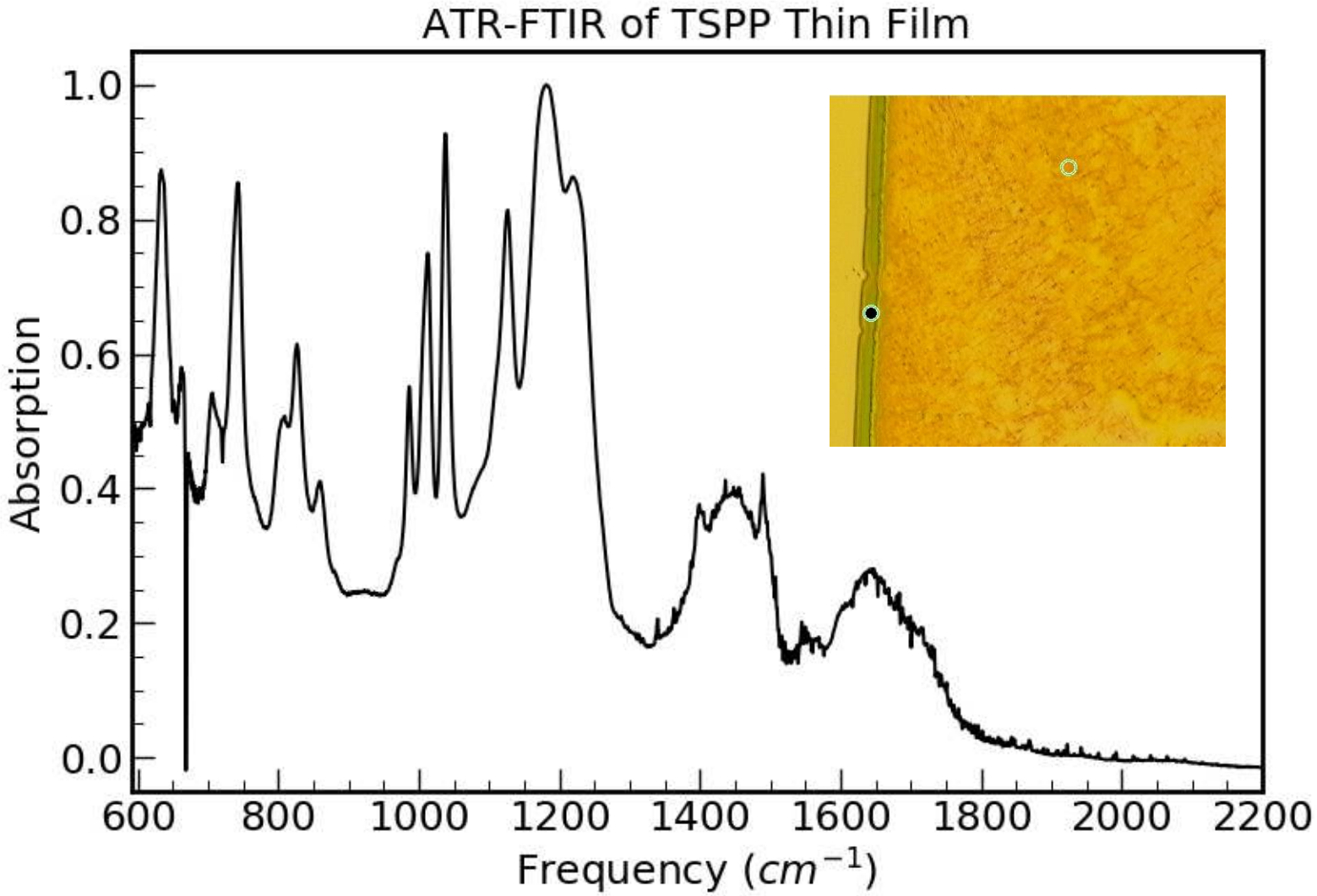

Figure 3.4 Representative ATR-FTIR spectrum of a TSPP aggregate thin film on a gold mirror substrate. Inset: 20x microscope image of the edge of the TSPP thin film including spectrum sample location (black dot).

References

(1) Gouterman, M. Spectra of Porphyrins. *J. Mol. Spec.* **1961**, *6*, 138–163.

(2) M. Kasha, H. R. R.; El-Bayoumi, M. A. The Exciton Model in Molecular Spectroscopy. *Pure Appl. Chem.* **1965**, *11* (3–4), 371–392.

(3) Rahman, M.; Harmon, H. J. Absorbance Change and Static Quenching of Fluorescence of Meso-Tetra(4-Sulfonatophenyl)Porphyrin (TPPS) by Trinitrotoluene (TNT). *Spectrochim. Acta - Part A Mol. Biomol. Spectrosc.* **2006**, *65* (3–4), 901–906.

(4) Ribó, J. M.; Crusats, J.; Farrera, J.-A.; Valero, M. L. Aggregation in Water Solutions of Tetrasodium Diprotonated Meso-Tetrakis(4-Sulfonatophenyl)Porphyrin. *J. Chem. Soc., Chem. Commun.* **1994**, *7* (6), 681–682.

(5) Hollingsworth, J. V; Richard, A. J.; Grac, M.; Vicente, H.; Russo, P. S. Characterization of the Self-Assembly of Meso -Tetra (4- Sulfonatophenyl) Porphyrin (H 2 TPPS 4 −) in Aqueous Solutions. *Biomacromolecules* **2011**, *13* (1), 60–62.

(6) Akins, D. L.; Akins, D. L.; Zhu, H.-R.; Zhu, H.-R.; Guo, C.; Guo, C. Aggregation of Tetraaryl-Substituted Porphyrins in Homogeneous Solution. *J. Phys. Chem.* **1996**, *100* (13), 5420–5425.

(7) Vlaming, S. M.; Augulis, R.; Stuart, M. C. A.; Knoester, J.; Van Loosdrecht, P. H. M. Exciton Spectra and the Microscopic Structure of Self-Assembled Porphyrin Nanotubes. *J. Phys. Chem. B* **2009**, *113* (8), 2273–2283.

(8) Rich, C. C.; McHale, J. L. Influence of Hydrogen Bonding on Excitonic Coupling and Hierarchal Structure of a Light-Harvesting Porphyrin Aggregate. *Phys. Chem. Chem. Phys.* **2012**, *14* (7), 2362.

(9) Mou, C.; Chen, D.; Wang, X.; Zhang, B.; He, T.; Xin, H.; Liu, F. C. Surface-Enhanced Raman Scattering of TSPP, Ag(II)TSPP, and Pb(II)TSPP Adsorbed on AgI and AGCl Colloids. *Spectrochim. Acta Part A Mol. Spectrosc.* **1991**, *47* (11), 1575–1581.

(10) Akins, D. L.; Zhu, H. R.; Guo, C. Absorption and Raman Scattering by Aggregated Meso-Tetrakis(p-Sulfonatophenyl)Porphine. *J. Phys. Chem.* **1994**, *98* (14), 3612–3618.

(11) Guo, C.; Ren, B.; Akins, D. L. Micro-Raman Spectroscopy of Meso -Tetrakis (p - Sulfonatophenyl) Porphine at Electrode Surfaces. *J. Phys. Chem. B* **1998**, 8751–8756.

(12) Friesen, B. a.; Rich, C. C.; Mazur, U.; McHale, J. L. Resonance Raman Spectroscopy of Helical Porphyrin Nanotubes. *J. Phys. Chem. C* **2010**, *114* (39), 16357–16366.

(13) Gogoleva, S. D.; Lavysh, a. V.; Motevich, I. G.; Askirka, V. F.; Strekal, N. D.; Sheinin, V. B.; Koifman, O. I.; Zenkevich, E. I.; Maskevicha, S. a. Surface-Enhanced Raman

Spectra of Tetra(4-Sulfonatophenyl)Porphyrin on the Surface of Plasmonic Silver Films. *J. Appl. Spectrosc.* **2016**, *83* (2), 159–164.

Chapter 4: Phase Acrobatics: The Influence of Excitonic Resonance and Gold Nonresonant Background on Heterodyne-Detected Vibrational Sum Frequency Generation Emission

Disclaimer

This chapter is a reproduction of a previous publication[a] of the same title authored by Christopher C. Rich, Kathryn A. Lindberg, and Amber T. Krummel. Kathryn Lindberg's contributions to this publication were assistance with sample preparation, spectral acquisition, operating and maintaining the laser table, and building optical lines in the home-built spectrometer.

4.1 Introduction

Recently, heterodyne-detected vibrational sum frequency generation (HD-VSFG) spectroscopy has garnered much attention because of its utility in probing molecular properties at surfaces and interfaces.[1–9] In general, sum frequency generation (SFG) spectroscopy techniques are nonlinear spectroscopic techniques sensitive to the macroscopic polarization formed in noncentrosymmetric media or at the interface between media under the electric dipole approximation. Double-resonance varieties of SFG spectroscopy (DRSFG), in particular when applied to VSFG, allow for the measurement of the vibrational, electronic, and vibronic coupling properties of interfacial molecular systems.[10–14] The incorporation of heterodyne detection and phase sensitivity in recent implementations of the technique have given rise to new discoveries

[a] Rich, C., Lindberg, K., Krummel, A. *Journal of Physical Chemistry Letters* (**2017**) *8*, 1331-1337

affiliated with absolute molecular orientation at complex molecular interfaces as well as debate on the characterization of the phase of the SFG emission.[5,8,9,15−20]

The debate on phase characterization of SFG is warranted because proper description of the phase of the emission and contributions made to that phase is necessary for assigning the absolute orientation of vibrational and electronic transition dipole moments at interfaces and in inherently noncentrosymmetric materials. In this Letter, we will demonstrate the utility of combining double-resonance conditions and polarization schemes to reveal both excitonic and monomeric properties of porphyrin-based molecular aggregates. Moreover, the influence of gold nonresonant SFG and double resonance on the phase of HD-VSFG emission will be discussed. We will show how additive phase contributions can be detected and resolved in HD-VSFG and present a comprehensive description for handling phase contributions in HD-VSFG. When taken together, the experimental results and analysis in this work reveal the ability to probe both monomeric and excitonic properties of porphyrin-based molecular aggregates in a single set of experiments.

4.2 HD-VSFG Experimental Setup and TSPP Sample System

In VSFG spectroscopy, specifically in frequency-domain applications, short pulse duration, broad bandwidth, mid-IR pulses are overlapped spatially and temporally with long pulse duration and narrow bandwidth visible pulses at the sample. In samples which do not exhibit inversion symmetry (i.e., noncentrosymmetric), sum frequency generation can occur, and the emitted light is the sum of the visible pulse frequencies and the mid-infrared (mid-IR) pulse frequencies which are resonant with a simultaneously IR- and Raman-active vibrational transition. In these experiments, the visible pulses are 5 ps in duration, generating a narrow

bandwidth [10 cm^{-1} full width at half-maximum (fwhm)] with a center wavelength of 787.75 nm, and the mid-IR pulses are <50 fs in duration with a center frequency of 1540 cm^{-1}; the mid-IR has 230 cm^{-1} fwhm bandwidth as estimated from the fwhm of the SFG spectrum (see **Figure 4.5** in the Supporting Information). The combination of these visible and mid-IR wavelengths are useful for probing the macrocycle vibrations of TSPP (tetra(4- sulfonatophenyl)porphyrin) aggregates. To accomplish heterodyne detection, a so-called "LO-first", passively phase-stabilized geometry is implemented.[2,7,8,21,22] The design of the HD-VSFG spectrometer used in this work is fully described in the Supporting Information (see **Figure 4.6**). Briefly, prior to the sample, the mid-IR and visible pulses are focused into a 150 μm thick ZnO film supported on a 1 mm thick CaF_2 window, which produces a nonresonant SFG emission used as the local oscillator (LO). Using common reflective optics, all three pulses (mid-IR, visible, and LO) are refocused onto the sample while delaying the LO pulse by passing it through 3 mm of fused silica. As a result, the SFG emission of the sample and the LO are spatially overlapped and exhibit a 5 ps delay between each other that, when measured on a spectrometer, produces a spectrum with fringes that are indicative of interference. Fourier filtering is employed to extract phase-sensitive SFG spectra and is described in detail in the Supporting Information (see **Figure 4.7**). Polarization of the visible pulses is controlled using a half waveplate and wire grid polarizer. Consequently, this allows for tuning the energy of the visible pulses, which is critical in the doubly resonant regime. Collecting a specific polarization of the SFG emission and LO is achieved with a wire grid polarizer. In this study, we measure PPP (P-polarized SFG, P-polarized visible, P-polarized mid-IR) and SSP (S-polarized SFG, S- polarized visible, and P-polarized mid-IR) polarization configurations.

TSPP molecular aggregates are a water-soluble model system that are analogous to chlorophyll aggregates found in the chlorosomes of photosynthetic green sulfur bacteria, thus generating interest for their potential in photochemical applications.[23−25] These aggregates have been determined to take on a nanotubular structure by a wide variety of experiments; the nanotubular structures have exhibited chiral signatures indicative of a helical internal structure.[26−31] The chiral, nanotube structure of these assemblies, as well as the similarity between the molecular geometry and electronic properties of porphyrin and chlorophyll, make this model system an interesting platform to examine the utility of HD-VSFG spectroscopy and doubly resonant conditions to reveal the interplay between vibrational, electronic, and vibronic coupling in interfacial systems. The TSPP aggregates were prepared by dissolving solid TSPP diacid salt in 0.75 M hydrochloric acid solution, thus producing a cloudy green solution. The TSPP molecular aggregates were then drop-cast on gold substrates. A precise molecular level description of the internal structure of TSPP aggregates has been debated in the literature.[13,26,28,32,33] The experiments presented here demonstrate the ability to probe both the monomeric and excitonic properties in a single experimental platform. However, the structural details of the TSPP aggregates are beyond the scope of this Letter and will be presented in depth in a subsequent publication.

Information on the aggregation and molecular structure of porphyrin can be extracted from their ultraviolet−visible (UV−vis) absorption spectra. Shown in **Figure 4.1** are the UV−vis absorption spectra of the Q-band region for monomeric diacid TSPP dissolved in water and TSPP aggregates. Briefly, for porphyrin there are two primary electronic transitions observed in the UV−vis spectrum: the B-band in the blue part of the spectrum and the Q-band in the red-part of the spectrum. In an idealized porphyrin, which are 4-fold symmetric and planar, the B-band

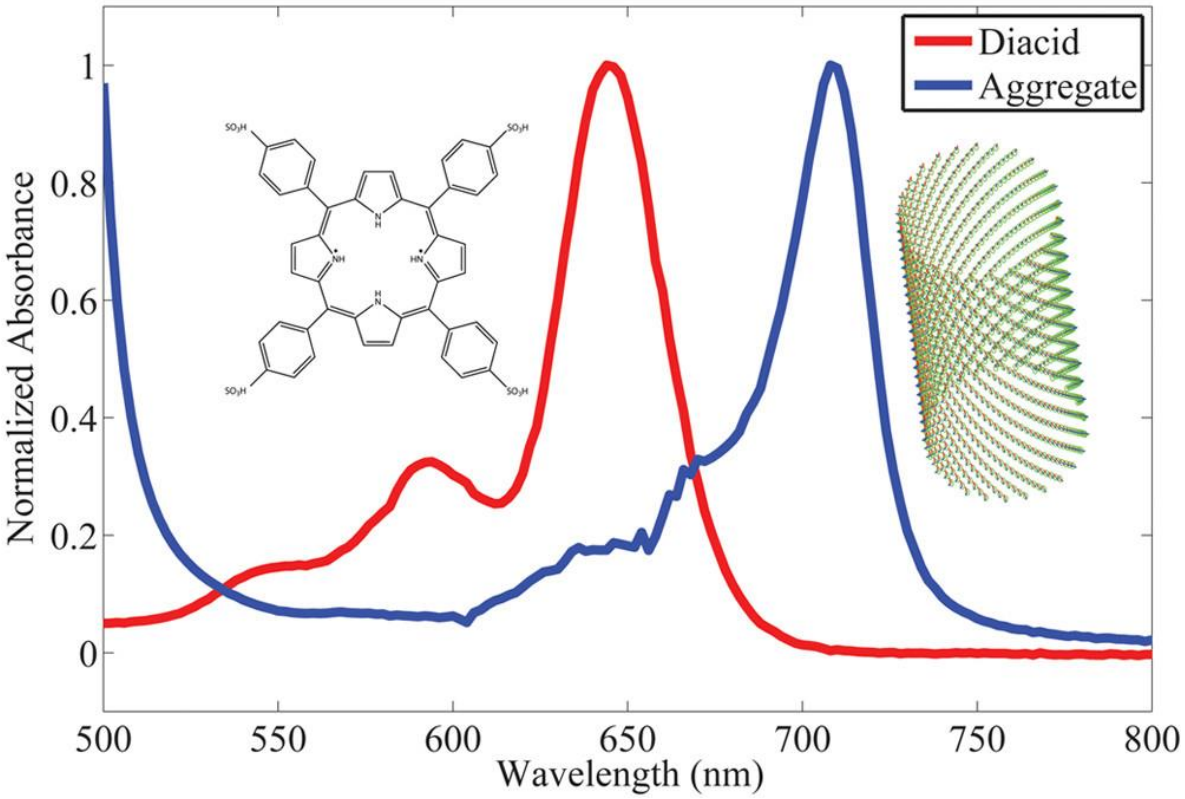

Figure 4.1 Normalized UV–vis absorption spectra of the diacid form of TSPP (red) and the TSPP aggregate (blue) in the Q-band region. To the left of the diacid Q-band is a drawing of the TSPP diacid monomer. To the right of the aggregate Q-band is a postulated aggregate structure, where each green circle represents a monomer and each monomer has corresponding transition dipole moments that lie parallel (red arrows) and perpendicular (blue arrows) with respect to the nanotube wall.

carries the majority of the oscillator strength while the Q-band is only weakly allowed primarily through vibronic sideband transitions. As the symmetry of the porphyrin is perturbed, either by breaking of the 4-fold symmetry or through out-of-plane distortions, intensity borrowing between the Q-band and the B-band takes place and the 0−0 transition in the Q-band takes on more oscillator strength at the expense of the B-band. Of note for this study in particular is the spectral red shift the Q-band transition between the spectra of the TSPP diacid monomer and that of the aggregate (see Figure 4.1). The spectral shift is typically indicative of J-type aggregation and potential molecular deformation which leads to intensity borrowing from the B-band to the Q-band.[34,35] As a consequence of this red shift, both vibrational resonance and electronic resonance in this VSFG experiment may be attainable, as the SFG frequency [12 694 cm^{-1} (visible frequency) + 1540 cm^{-1} (center IR frequency) = 14 234 cm^{-1} or 702.5 nm] is now resonant with the center wavelength of the Q-band at 707 nm. If double-resonance conditions are met, both the vibrational properties of these aggregates and their coupling to electronic excitonic properties may be examined in these HD-VSFG experiments.

4.3 Theory on Resonance and Phase in HD-VSFG

An important component of the discussion of the HD-VSFG spectra is the influence of gold on the phase of the VSFG emission. Often the SFG emission associated with gold is labeled as a nonresonant SFG. However, this is not always true in many VSFG experiments where the SFG wavelength is visible, allowing for access of the d band to s band transition in gold.15,[36] In this study, the SF frequency is significantly preresonant of this transition, which occurs at 480 nm; thus, the SFG emission of gold in these experiments is a nonresonant emission that will impart close to a $\pi/2$ phase shift in the emitted field. Although chemisorption to the gold surface

can cause deviations in this phase, the deviations are not so substantial as to drastically change the lineshapes of real and imaginary second-order susceptibility ($\chi^{(2)}$) spectra.[9,15] As a result, the gold SFG emission from the sample can be used as an internal phase reference. The signal of a singly resonant VSFG field from a molecule interfering with the SFG field from gold can be generally expressed by the following equation:

$$|E_{tot}|^2 = |E_s + E_{Au}|^2 = |E_s|^2 + |E_{Au}|^2 + E_s E_{Au}^* + E_{Au} E_s^* \tag{1}$$

where E_{tot}, E_s, and E_{Au} represent the electric fields of the total, sample, and gold SFG emission, respectively. Each field is proportional to the magnitude of the second-order susceptibility, which will be denoted as $\chi^{(2)}$, and its associated phase:

$$|E_s|^2 + |E_{Au}|^2 + E_s E_{Au}^* + E_s^* E_{Au} \propto \left|\chi_s^{(2)}\right|^2 + \left|\chi_{Au}^{(2)}\right|^2 + \left(\chi_{s,Re}^{(2)} + i\chi_{s,Im}^{(2)}\right)\left(-i\chi_{Au}^{(2)}\right) +$$

$$\left(\chi_{s,Re}^{(2)} - i\chi_{s,Im}^{(2)}\right) i\chi_{Au}^{(2)} = \left|\chi_s^{(2)}\right|^2 + \left|\chi_{Au}^{(2)}\right|^2 + 2\chi_{s,Im}^{(2)}\chi_{Au}^{(2)} \tag{2}$$

Removing the small contribution of the sample and subtracting the spectrum of gold from eq 2 produces the cross term $2\chi_{s,Im}^{(2)}\chi_{Au}^{(2)}$. Dividing the cross term by $2\chi_{Au}^{(2)}$ produces a spectrum which is directly proportional to the imaginary part of the second-order susceptibility. Kramers−Kronig transformation of $\chi_{s,Im}^{(2)}$ produces the real part of the susceptibility. If the VSFG emission of the sample is doubly resonant such that the sum frequency of the mid-IR and visible pulses are resonant with an electronic transition, a sum frequency-dependent phase, ϕ_{el}, is applied to $\chi_s^{(2)}$. When close to resonance with the Q-band, the SF frequencies involved in this phase term can be simplified to a constant phase of $\pi/2$, which we justify in the Supporting Information:

$$\left(\chi_{s,Re}^{(2)} + i\chi_{s,Im}^{(2)}\right)e^{i\phi_{el}} \approx \left(\chi_{s,Re}^{(2)} + i\chi_{s,Im}^{(2)}\right)e^{i\pi/2} = i\left(\chi_{s,Re}^{(2)} + \chi_{s,Im}^{(2)}\right) = i\chi_{s,Re}^{(2)} - \chi_{s,Im}^{(2)}$$

(3)

As a result, eq 2 would be rewritten as

$$|E_s|^2 + |E_{Au}|^2 + E_s E_{Au}^* + E_s^* E_{Au} \propto \left|\chi_s^{(2)}\right|^2 + \left|\chi_{Au}^{(2)}\right|^2 + \left(i\chi_{s,Re}^{(2)} - \chi_{s,Im}^{(2)}\right)\left(-i\chi_{Au}^{(2)}\right) +$$

$$\left(-i\chi_{s,Re}^{(2)} - \chi_{s,Im}^{(2)}\right)i\chi_{Au}^{(2)} = \left|\chi_s^{(2)}\right|^2 + \left|\chi_{Au}^{(2)}\right|^2 + 2\chi_{s,Re}^{(2)}\chi_{Au}^{(2)}$$

(4)

Thus, as a result of double resonance in the VSFG experiment, a 90° phase flip in the spectra of $\chi_s^{(2)}$ should be observed. However, it should be made clear that this 90° flip is applicable only when the SF frequency is as close to resonance as the vibrational frequencies are in this study. Further from resonance and this approximation could not be made.

The previous discussion details how an internal LO derived from the SFG emission of gold can produce phase-sensitive HD-VSFG spectra. However, this method can be used only in the PPP polarization configuration. For other polarization configurations like SSP, no second-order polarization is generated from gold; thus, the internal LO method cannot be performed. For the SSP experiment, an external LO HD-VSFG spectroscopy variation described above is used to generate phase-sensitive spectra. Similar to the internal LO heterodyne detection methodology, the interference between the sample SFG and LO is measured while incorporating a time delay, *T*, between the two fields in the cross terms:

$$\left|E_s + E_{LO}e^{i\omega T}\right|^2 = |E_s|^2 + |E_{LO}|^2 + E_s E_{LO}^* e^{-i\omega T} + E_s^* E_{LO} e^{i\omega T}$$

$$\propto \left|\chi_s^{(2)}\right|^2 + \left|\chi_{Au}^{(2)}\right|^2 + \left(\chi_{s,Re}^{(2)} + i\chi_{s,Im}^{(2)}\right)\chi_{LO}^{(2)} e^{-i\phi_{LO}} e^{-i\omega T} + \left(\chi_{s,Re}^{(2)} - i\chi_{s,Im}^{(2)}\right)\chi_{LO}^{(2)} e^{i\phi_{LO}} e^{i\omega T}$$

(5)

Equation 5 is valid for a singly resonant transition. For a doubly resonant transition, this equation changes to

$$\left|E_s + E_{LO}e^{i\omega T}\right|^2 = |E_s|^2 + |E_{LO}|^2 + E_s E_{LO}^* e^{-i\omega T} + E_s^* E_{LO} e^{i\omega T}$$

$$\propto \left|\chi_s^{(2)}\right|^2 + \left|\chi_{Au}^{(2)}\right|^2 + \left(i\chi_{s,Re}^{(2)} - \chi_{s,Im}^{(2)}\right)\chi_{LO}^{(2)} e^{-i\phi_{LO}} e^{-i\omega T} + \left(-i\chi_{s,Re}^{(2)} - \chi_{s,Im}^{(2)}\right)\chi_{LO}^{(2)} e^{i\phi_{LO}} e^{i\omega T}$$

(6)

In the temporal interferogram of the SSP HD-VSFG spectrum, which is produced through Fourier transform of the frequency domain spectrum, three features are observed (see Figure 4.7c). The DC component contains information related to the first two terms of eqs 5 and 6. The other two features occur at time delays $+T$ and $-T$ between the LO and sample SFG emission and correspond to each of the cross terms in eqs 5 and 6. By isolating one of these features by Fourier filtering, we can produce the spectral interferogram of one of the cross terms. To extract the spectrum of the complex susceptibility of the sample, the spectral interferogram is normalized by that of a chosen phase reference; for these experiments, the phase reference is the PPP polarization HD-SFG spectrum of a gold mirror. Taking into account the $\pi/2$ phase shift of the gold SFG emission, the terms in eq 5 which correspond to $+T$ can be normalized:

$$\frac{\left(\chi_{s,Re}^{(2)} - i\chi_{s,Im}^{(2)}\right)\chi_{LO}^{(2)} e^{i\phi_{LO}} e^{i\omega T}}{-i\chi_{Au}^{(2)}\chi_{LO}^{(2)} e^{i\phi_{LO}} e^{i\omega T}} = \frac{i\left(\chi_{s,Re}^{(2)} - i\chi_{s,Im}^{(2)}\right)}{\chi_{Au}^{(2)}} = \frac{i\chi_{s,Re}^{(2)} + \chi_{s,Im}^{(2)}}{\chi_{Au}^{(2)}}$$

(7)

For doubly resonant SFG, normalization of the same term in eq 6 takes on the form

$$\frac{\left(-i\chi_{s,Re}^{(2)} - \chi_{s,Im}^{(2)}\right)\chi_{LO}^{(2)} e^{i\phi_{LO}} e^{i\omega T}}{-i\chi_{Au}^{(2)}\chi_{LO}^{(2)} e^{i\phi_{LO}} e^{i\omega T}} = \frac{i\left(-i\chi_{s,Re}^{(2)} - \chi_{s,Im}^{(2)}\right)}{\chi_{Au}^{(2)}} = \frac{\chi_{s,Re}^{(2)} - i\chi_{s,Im}^{(2)}}{\chi_{Au}^{(2)}}$$

(8)

In both cases, we note that direct normalization to the spectral interferogram of gold results in cancelation of the LO contribution as well as a $\pi/2$ phase flip of the signal. The contribution of gold is removed from these expressions by multiplying the Fourier filtered HD-VSFG spectra by

the square root of the amplitude of the homodyne-detected gold SFG spectrum. From eqs 7 and 8, one of two conclusions can be made from the SSP-polarized VSFG spectrum: (1) The imaginary part of the spectrum reports on the imaginary part of the susceptibility under doubly resonant conditions. (2) The real part of the spectrum reports on the imaginary part of the susceptibility under singly resonant conditions.

4.4 HD-VSFG Results and Discussion

Figure 4.2 shows the resulting complex HD-VSFG spectra of TSPP aggregates on gold for PPP and SSP polarization configurations. The PPP spectrum was produced via internal LO heterodyne detection, and the SSP spectrum was produced via external LO heterodyne detection. As Fourier filtering removes a considerable amount of noise from the spectrum, the SSP spectra appear smoother than that of the PPP spectrum. Both PPP and SSP spectra are normalized to a PPP homodyne-detected VSFG spectrum of gold exposed to the same mid-IR and visible pulse energies. The $\left|\chi_s^{(2)}\right|^2$ spectra (Figure 4.2c) of both polarization configurations are determined directly by the absolute square of the complex spectra. The component of the HD-VSFG spectrum which carries information related to the imaginary part of the second-order susceptibility should contain peaks which appear in the corresponding $\left|\chi_s^{(2)}\right|^2$ spectrum. On the basis of this observation, $\chi_{s,Im}^{(2)}$ is represented in both the PPP HD-VSFG spectrum and the SSP HD-VSFG spectrum by the real spectrum. This implies that the PPP polarization configuration produces a spectrum which reflects doubly resonant VSFG, whereas the SSP polarization configuration produces a spectrum which reflects only resonance with the vibrational transition. Remarkably, this suggests that VSFG spectroscopy can relay aspects of the electronic exciton of

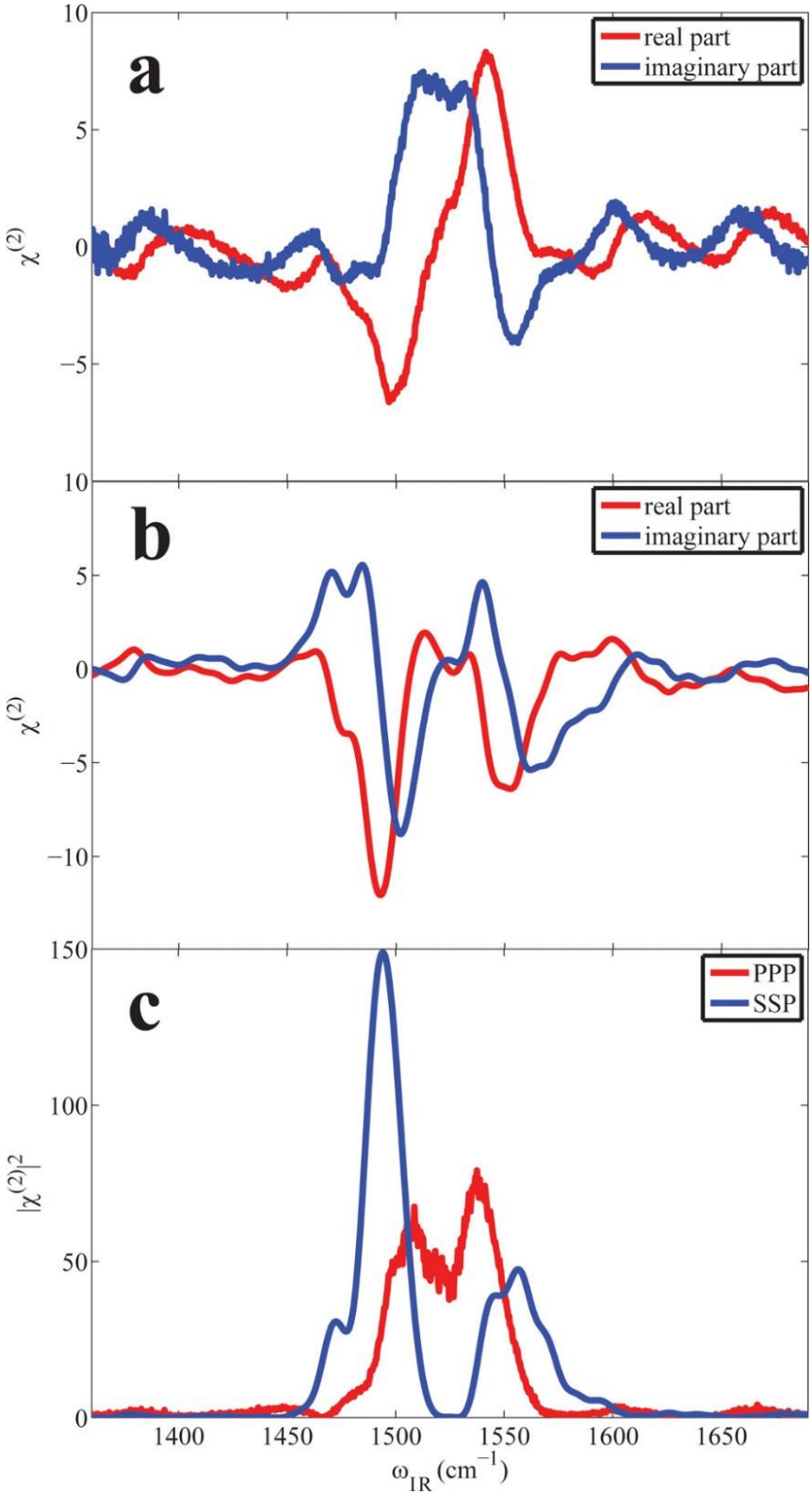

Figure 4.2 (a) Real (red) and imaginary (blue) HD-VSFG spectra of the TSPP aggregates on gold using the PPP polarization configuration. (b) Same as in panel a for the SSP configuration. (c) The $|\chi_s^{(2)}|^2$ spectra for the PPP (red) and SSP (blue) polarization configurations.

these molecular aggregates in one polarization scheme and the molecular geometry of the monomeric species in the assembly in another polarization scheme. Thus, we have shown that phase-sensitive VSFG can uniquely provide excitonic, vibronic, and structural information on molecular assemblies. The fascinating revelations associated with these spectra require in-depth discussions which will be addressed in a subsequent article. However, these VSFG measurements effectively establish the vibrational modes associated with delocalized molecular excitons and the molecular geometry associated with the internal structure of the molecular aggregate.

Figures 4.3 and **4.4** show the "phase acrobatics" which must be applied to the HD-VSFG spectra for the PPP and SSP polarization configurations, respectively, to produce spectra directly related to the complex second-order susceptibility of the molecular system. For PPP polarization, multiplying the complex HD-VSFG spectrum by $-i$ negates the phase shift due to the resonance of the sum frequency with the transition to the Q-band electronic state. This 90° phase flip produces the complex phase-sensitive VSFG spectrum which reflects the second-order susceptibility derived solely from the molecular vibrations. For SSP polarization, the complex second-order susceptibility spectra is derived by taking the HD-VSFG spectra and compensating for the phase of the gold SFG phase reference and the change in the sign of the imaginary part of the susceptibility.

For chiral nanotube aggregates such as TSPP aggregates, three excitonic states, neglecting nonadiabatic phenomena, should arise from degenerate monomeric electronic or vibrational states through excitonic coupling: a nondegerate exciton state, whose transition dipole is oriented along the nanotube long axis, and a doubly degenerate pair of exciton states, whose transition dipoles are oriented along *x*- and *y*- short axes of the nanotube. The vibrations

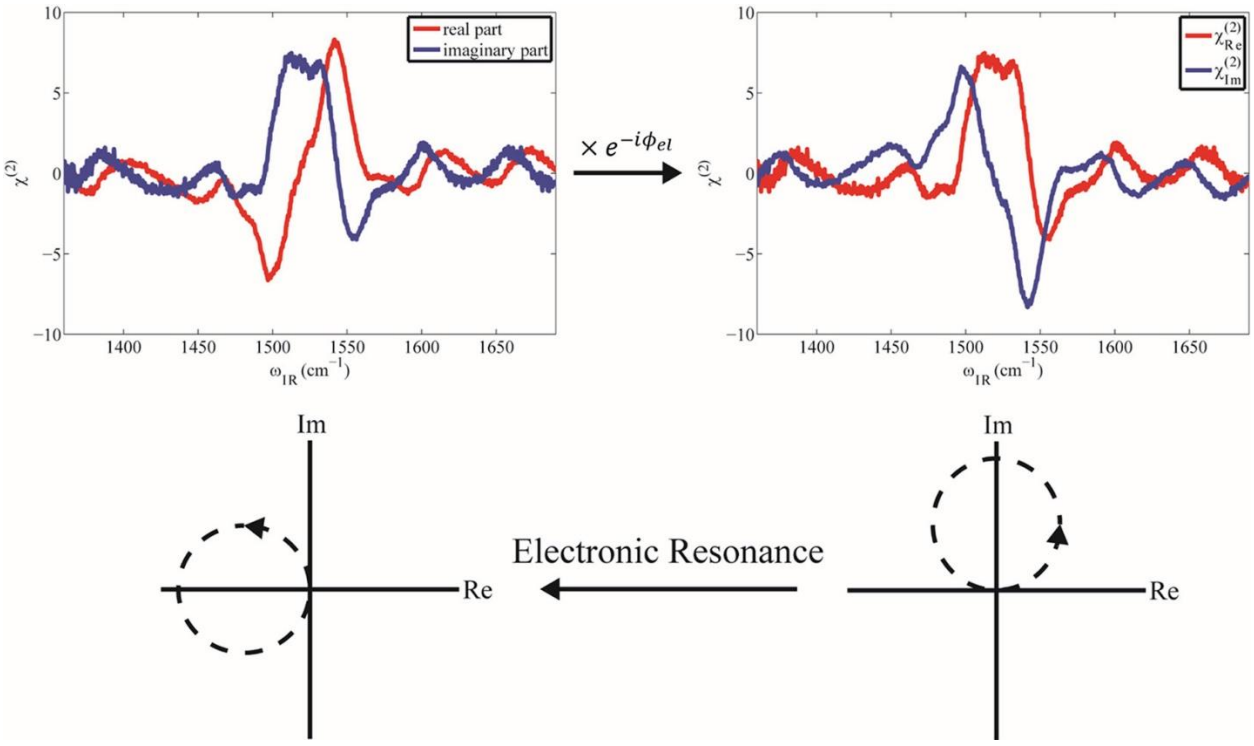

Figure 4.3 (Top) Original PPP HD-VSFG spectra of TSPP aggregates deposited on gold (left) and the phase shift to compensate for resonance with the electronic excited state (right). (Bottom) Schematic representation of the Argand plot associated with a single vibrational mode (right) and the π/2 phase shift associated with electronic resonance (left).

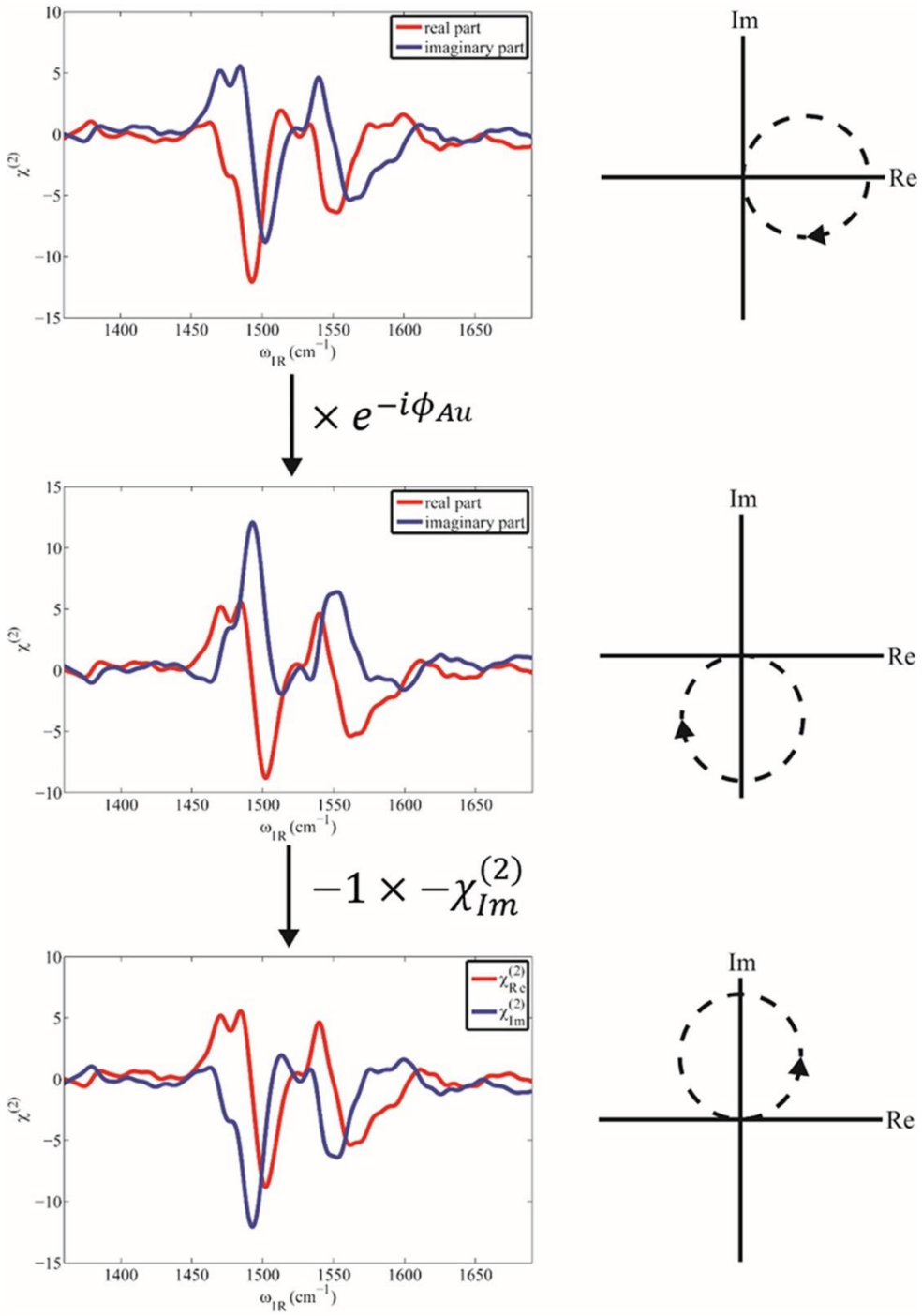

Figure 4.4 (Left) Original SSP HD-VSFG spectra of TSPP aggregates deposited on gold (top) and the phase shifts to compensate for the influence gold phase reference (middle) and with the negative sign of χs,Im(2) (bottom). To the right of each set of spectra are representative schematics of the Argand plot of a single vibrational mode reflecting the effect of each phase flip.

of concern in this work are associated with macrocycle C=C vibrations whose transition dipole moments lie within the plane of the porphyrin ring. If these transition dipoles are oriented parallel (or near parallel) to the transition dipoles associated with one of the excitonic transition dipole moments, the PPP-polarized spectra, where the polarization of the IR and visible fields are identical, should be sensitive to doubly resonant effects. However, for SSP-polarized spectra, where the polarization of the IR and visible fields are perpendicular, the observed vibrational and electronic dipole moments are orthogonal, which would result in singly resonant spectra which reflect only vibrational excitation.

A considerable number of vibrational resonances are apparent in both sets of spectra, but this discussion will be confined to the two most prominent features in each spectrum: the high-frequency peak at 1542 cm^{-1} (1553 cm^{-1}) and the low-frequency mode at 1497 cm^{-1} (1493 cm^{-1}) for the PPP (SSP) polarization configuration. Three main differences are observed between the PPP and SSP $\chi^{(2)}_{s,Im}$ spectra: (1) The high (low) frequency peaks blue (red) shifts between the PPP and SSP $\chi^{(2)}_{s,Im}$ spectra. (2) The low-frequency peak flips sign between the PPP and SSP $\chi^{(2)}_{s,Im}$ spectra. (3) The low-frequency mode in the SSP $\chi^{(2)}_{s,Im}$ spectrum is about 1.4 times more intense (based on integrated intensity) than that in the PPP $\chi^{(2)}_{s,Im}$ spectrum, while the high-frequency mode in the SSP $\chi^{(2)}_{s,Im}$ spectrum is about 3/4 times weaker than that in the PPP $\chi^{(2)}_{s,Im}$ spectrum. Shifts in the frequency of these vibrations have been shown to occur in resonance Raman spectra of TSPP upon aggregation; therefore, induced frequency shifts due to coupling to the resonant exciton state may be possible. The low-frequency mode sign flip in the PPP spectrum with respect to the SSP low-frequency mode reveals an interesting consequence of coupling to the resonant exciton state and may reflect the relative orientation between the transition dipole moment of the vibration and that of the exciton.

The analysis described above of the phase of the SFG emission for the PPP and SSP spectra reflect double resonance in the former and single resonance in the latter, which one would expect to result in considerable intensity disparity between the PPP and SSP spectral features as observed in resonance Raman spectra. However, no such resonance enhancement is apparent. We postulate two possible reasons for this observation. First, the macrocycle vibrations associated with these spectral features may not be totally symmetric vibrations; thus, resonance enhancement is not observed because of the lack of displacement between the electronic potential surfaces of the ground and excited exciton states along those normal coordinates. These modes would be identified as Franck−Condon inactive but can be observed under a few conditions: (1) a substantial frequency shift in the vibrational frequency between the ground- and excited-state frequencies; (2) a change in the symmetry, i.e., the point group, between the ground and excited states upon excitation, which can arise via Duschinsky rotation; (3) vibronic coupling, particularly between bright and dark exciton states, which results in the mixing of Born−Oppenheimer states via nontotally symmetric vibrations. A second plausible reason for the differences in intensity and frequency between the PPP and SSP spectra is the nature of the delocalization of the exciton. With the PPP spectrum probing the excitonic nature of the aggregate, rather than the porphyrin monomer in the SSP, the delocalization of the electronic wavefuction may reduce the oscillator strength of the probed molecular vibration which may not be as delocalized. This electronic delocalization could also change the force constant associated with the molecular vibration and thus change the vibrational frequency. However, it is important to note that whether these vibrations are localized to individual porphyrin or are delocalized over several porphyrin is not necessarily understood. Clearly, HD-VSFG spectroscopy has the capacity to reveal considerable information about molecular excitonics.

4.5 Conclusion

To conclude this Letter, we have discovered that HD-VSFG spectroscopy combined with utilization of double-resonance conditions and various polarization schemes can reveal both excitonic and monomeric properties in molecular aggregates. By carefully keeping track of the phase of the resulting HD- VSFG emission of TSPP aggregates under different polarization conditions, we have determined that the PPP spectrum measures a doubly resonant VSFG phenomenon which exhibits coupling of the molecular vibrations to the delocalized molecular exciton, whereas the SSP spectrum measures a singly resonant VSFG phenomenon which does not. For the field of molecular aggregates, this is an important discovery because it demonstrates that phase-sensitive vibrational sum frequency generation is sensitive to the delocalized nature of the exciton, the geometry of the monomers of which the aggregate is composed, and the vibronic coupling which can give rise to nonadiabatic phenomena. In a forthcoming contribution, we delve deeper into the molecular details unveiled by these results as well as the structure of the exciton.

4.7 Supporting Information

A diagram of our home-built HD-VSFG spectrometer is illustrated in **Figure 4.6**. To generate our mid-IR and visible pulses for this spectrometer we use a Ti:Sapphire based regenerative amplifier (Wyvern 1000, KM Labs) which produces 45 fs duration pulses at a 1 kHz repetition rate centered at 790 nm. Using a beamsplitter, 80% of this output is directed to a two stage collinear optical parametric amplifier (OPA, TOPAS Prime, Light Conversion), from which the signal and idler are collinearly combined in a silver gallium selenide ($AgGaSe_2$) crystal. The angle of the $AgGaSe_2$ crystal and the BBO crystal angles in the OPA tuned to

produce mid-IR pulses with a center frequency of 1540 cm^{-1} (center wavelength 6493.5 nm). The transmitting 20% of the Ti:Sapphire output is used for the visible light in this experiment and is sent through an interference filter (Andover Corp) in order to frequency narrow the pulses to a FWHM of 10 cm^{-1} (0.5 nm).

The spectrometer in this study utilizes a passively phase stabilized sample geometry in which the LO is generated prior to the sample and the mid-IR, visible, and LO pulses reflect off common optics following LO generation. Using a silver 6 inch focal length off axis parabolic mirror and 750 mm focal length fused silica lens, the mid-IR and visible pulses, respectively, are focused and overlapped in space and time on a 150 μm thick film of ZnO deposited on a 1 mm thick CaF_2 window to produce an SFG emission which is used as the local oscillator. All three beams, mid-IR, visible, and LO, are reflected by a common silver mirror towards a 200 mm focal length concave silver mirror. The LO is delayed by 5 ps with respect to the IR and visible pulses with a 3 mm thick fused silica window. The mid-IR, visible, and LO are then focused on the sample by the concave mirror at 60.7°, 66.2°, and 65.6° with respect to the sample surface normal. The sample is mounted on a translation stage which can translate in X, Y, and Z directions. A half waveplate and wire grid polarizer in the visible beam path control the polarization and energy of the visible pulses. The energies of the mid-IR and visible pulses at the sample are maintained at 5 μJ and 900 nJ, respectively. The emitted SFG from the sample and collinear delayed LO are directed through a wire grid polarizer to collect a specific polarization of SFG and LO, followed a waveplate to orient the polarization of the light into the P polarization to account for the polarization bias of the grating in the monochromator. The light is dispersed with an iHR550 monochromator (Horiba) and detected with a back illuminated TEC CCD detector (Synapse, Horiba). Polarization configurations used in this study are labeled in

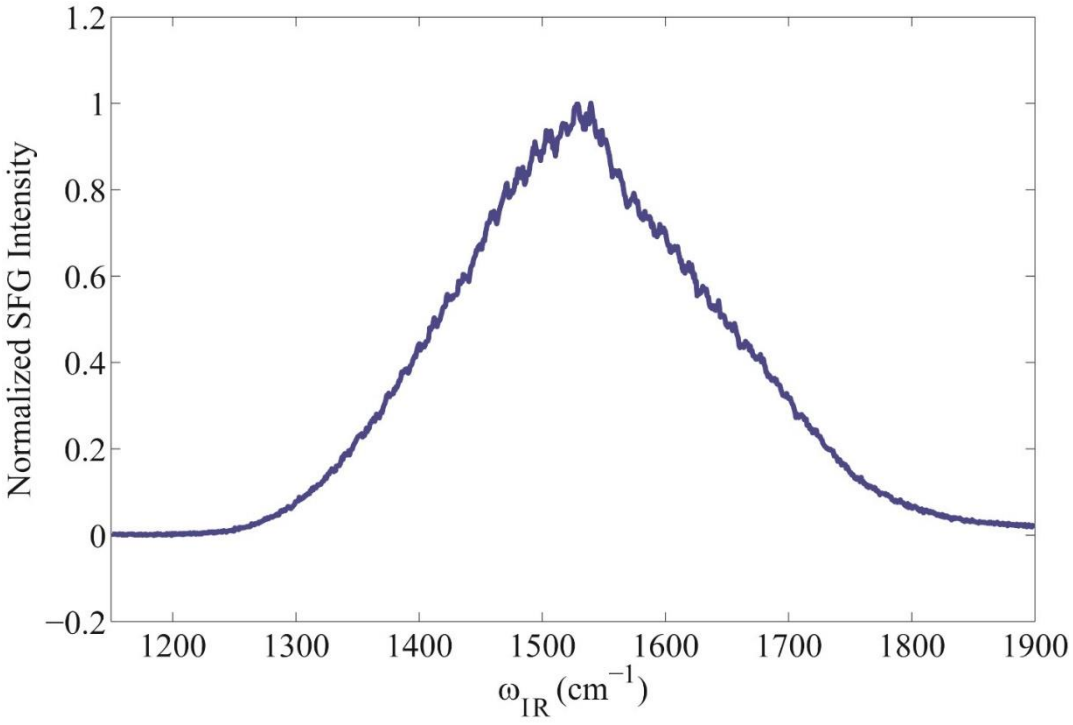

Figure 4.5 SFG spectrum of bare gold using 600 lines/mm grating.

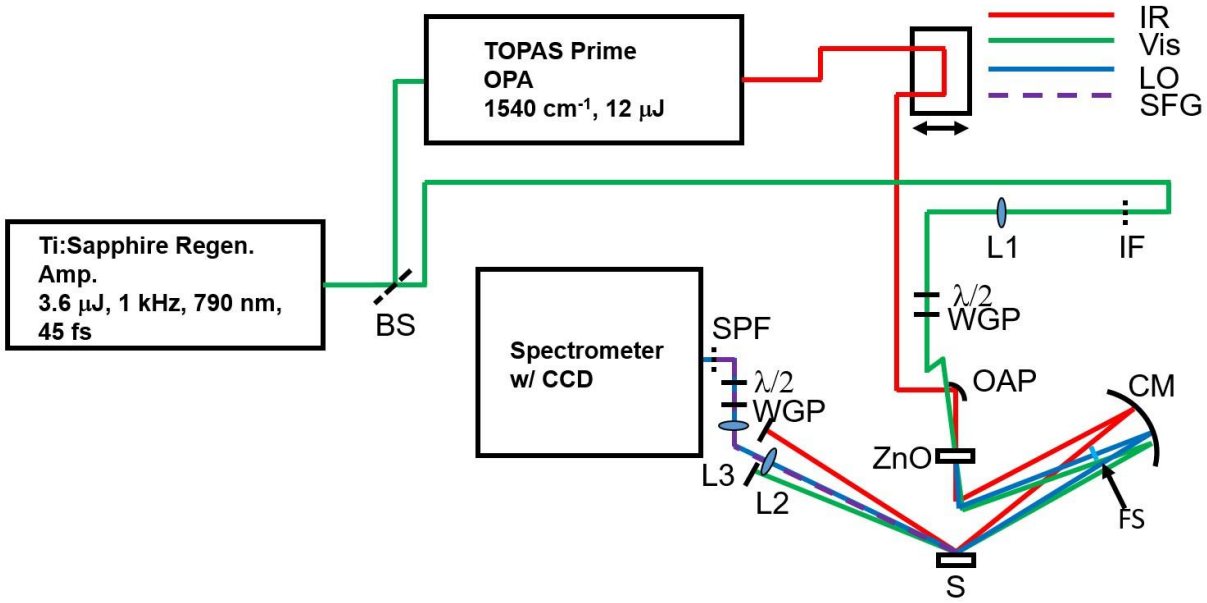

Figure 4.6 Diagram of the HD-VSFG spectrometer. BS = 80/20 beamsplitter; IF = interference filter; L1 = 750 mm focal length lens; l/2 = half waveplate; WGP = wire grid polarizer; OAP = 6 inch focal length 90° off axis parabolic silver mirror; ZnO = 150 μm thin film deposited on a CaF_2 window; FS = 3 mm thick fused silica window; CM = 200 mm silver concave mirror; S = sample; L2, L3 = 200 mm focal length lenses; SPF = 750 nm cut-off wavelength shortpass filter; red line = mid-IR beam path; green line = visible beam path; blue line = LO beam path; purple dashed line = sample SFG path.

order of descending frequency (SFG, visible, mid-IR). In this study, PPP and SSP polarization schemes are used. For experiments where gold in the sample is used to produce an internal LO, the nonresonant SFG produced from the ZnO is blocked. To ensure a consistent phase relationship between the sample and reference for both internal and external LO implementations, samples were prepared such that the TSPP aggregate and gold reference spectra could be collected on the same substrate. To this end samples were prepared by drop-casting the TSPP aggregate solution on to a small portion of the gold surface, leaving a considerable amount of the surface bare. Switching between measurements of the sample and reference HD-VSFG spectra was then accomplished by laterally translating the sample stage to assure consistent phase relationship between measurements.

Figure 4.7 presents the Fourier filtering process for producing external LO HD-VSFG spectra. The measured raw spectrum (a) is first Fourier transformed into the time domain (c). Three features are observed in temporal interferogram: an intense DC component at 0 fs, which contains information on the amplitude of the sample VSFG and the LO SFG emission, and two features at $+T$ and $-T$ where T is the delay between the VSFG from the sample and the LO. Applying a filter function window to select one of the latter features (as shown by the red plot in Fig. 4.7c) which correspond to the interference between the VSFG emission from the sample and the LO. Fourier transformation of the filtered temporal interferogram produces the spectral interferogram in Fig. 4.7e. To obtain the phase-sensitive HD-VSFG spectrum, the spectral interferogram of the sample must be normalized with the spectral interferogram of a phase reference, which in this case is the PPP HD-VSFG spectrum of bare gold (see Figs. 4.7b, 4.7d, and 4.7f).

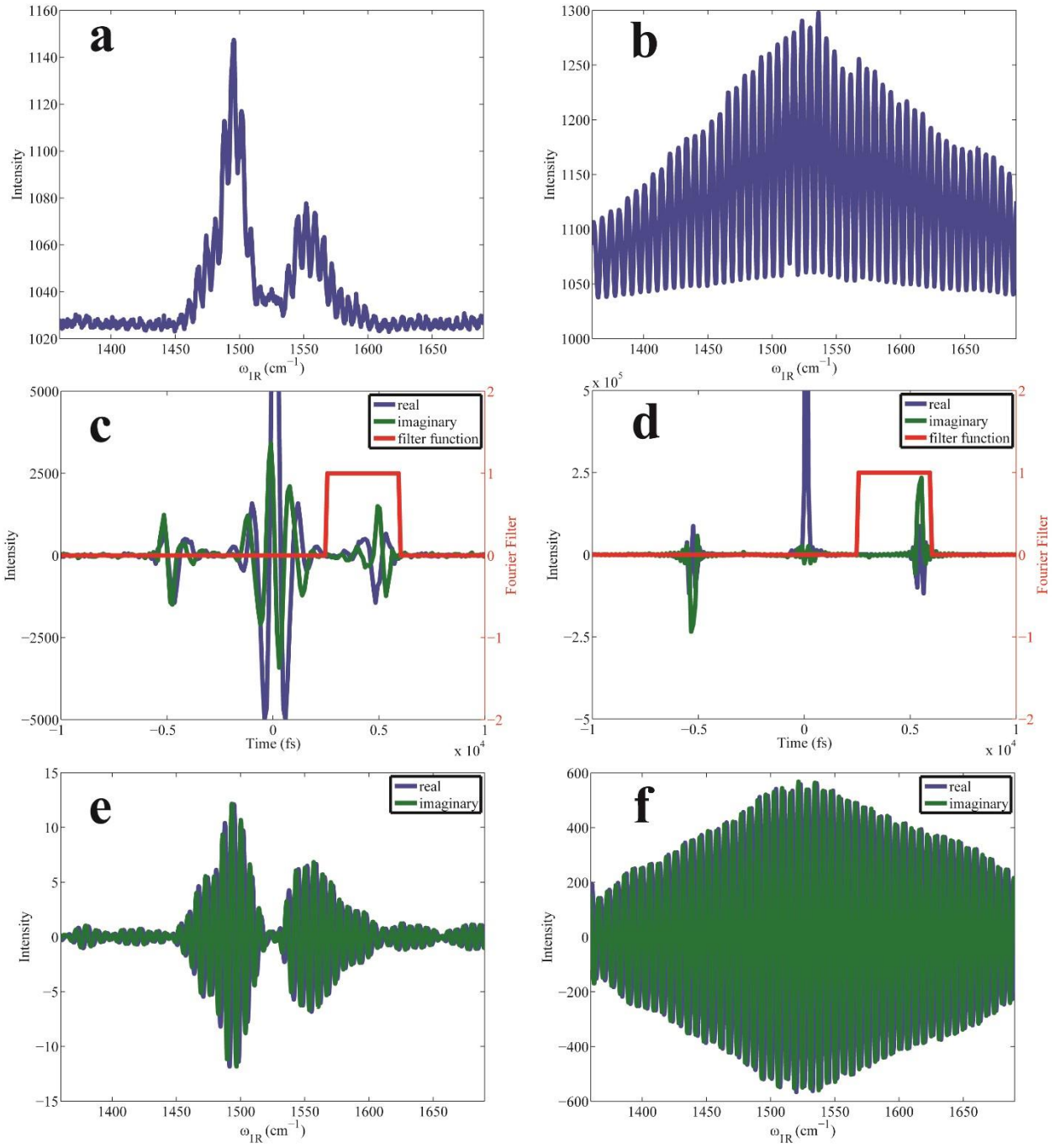

Figure 4.7 Spectra corresponding to the steps involved in Fourier filtering. a) The raw SSP HD-VSFG spectrum of TSPP aggregates on gold. b) The raw PPP HD-VSFG spectrum of bare gold. c) The Fourier transformed time domain spectrum of a with the Fourier filtering function. d) The Fourier transformed time domain spectrum of b with the Fourier filtering function. e) Resulting real (blue) and imaginary (green) spectral interferograms from Fourier filtering the spectra in c. f) Resulting real (blue) and imaginary (green) spectral interferograms from Fourier filtering the spectra in d.

Within a reasonable approximation, the UV-Vis absorption spectrum of the TSPP aggregates can be related to the imaginary part of the complex refractive index:

$$\kappa(\lambda) = 2.303\frac{A(\lambda)\lambda}{4\pi x}$$

Here, $\kappa(\lambda)$ is the imaginary part of the refractive index, $A(\lambda)$is the absorption spectrum, λ is the wavelength, and x is the path length. The real part of the refractive index can be determined via Kramers-Kronig transformation. The phase can then be determined and we have plotted in **Figure 4.8**. This frequency dependent electronic phase can then be applied to the HD-VSFG spectrum. In **Figure 4.9** we plot the resonant electronic phase in the SFG frequency range, which shows that for the vibrations we are concerned with, an applied phase between 90° and 100°. In **Figure 4.10** we show the VSFG spectrum with the frequency-dependent phase applied and the VSFG spectrum with a constant 90° phase applied.

Comparison of the complex spectra show that either treatment of the electronic resonance phase effectively produces similar real and imaginary $\chi^{(1)}$ spectra. Determination of the electronic phase contribution using the UV-vis spectrum of the TSPP aggregate solution (Figure 4.8); the electronic phase contribution determined from the UV-vis spectrum plotted in the HD-VSFG spectral range (Figure 4.9); comparison of the PPP polarized HD-VSFG spectra determined from the electronic phase contribution derived from the UV-vis spectrum and from a constant 90° phase shift.

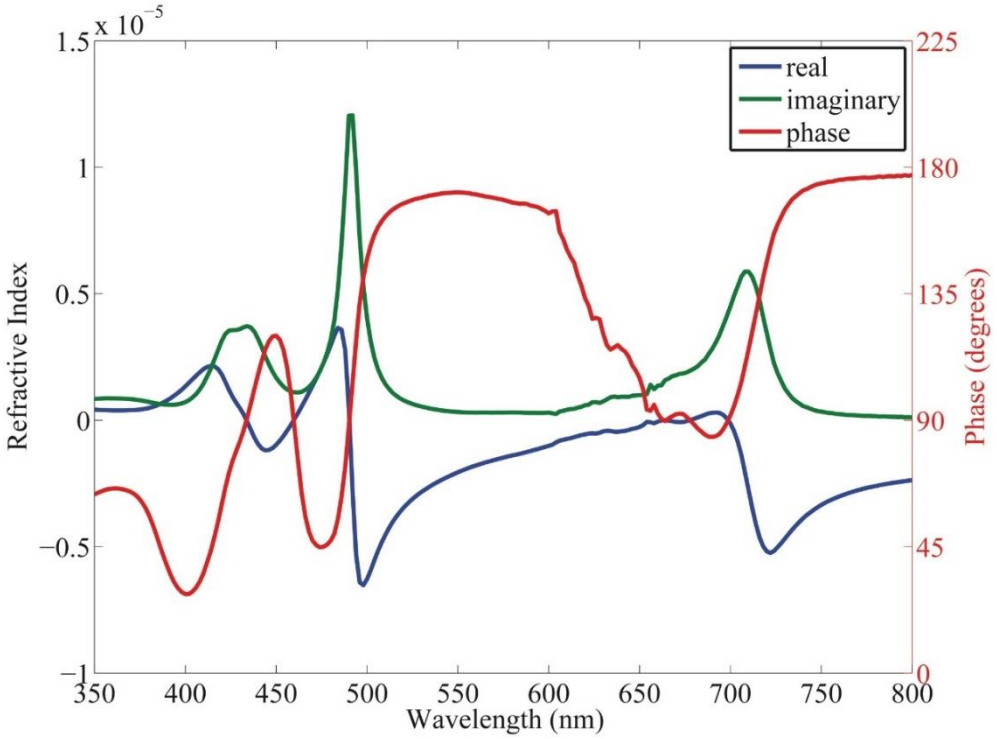

Figure 4.8 Real (blue) and imaginary (green) refractive index spectra of TSPP aggregates in water with corresponding phase (red).

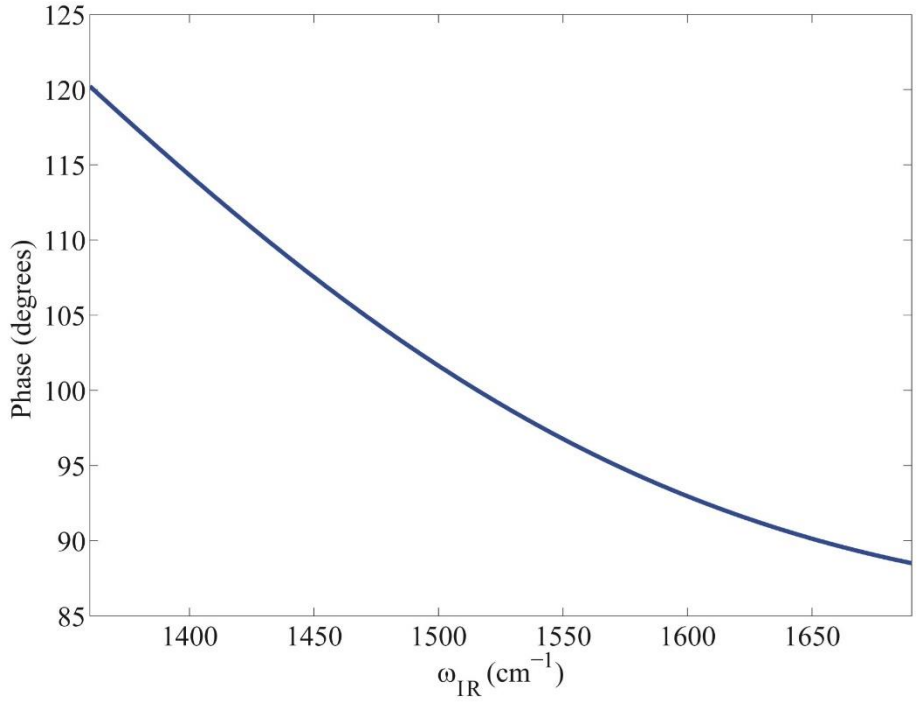

Figure 4.9 Electronic resonance phase spectrum for the frequency range examined in the VSFG spectra in this study.

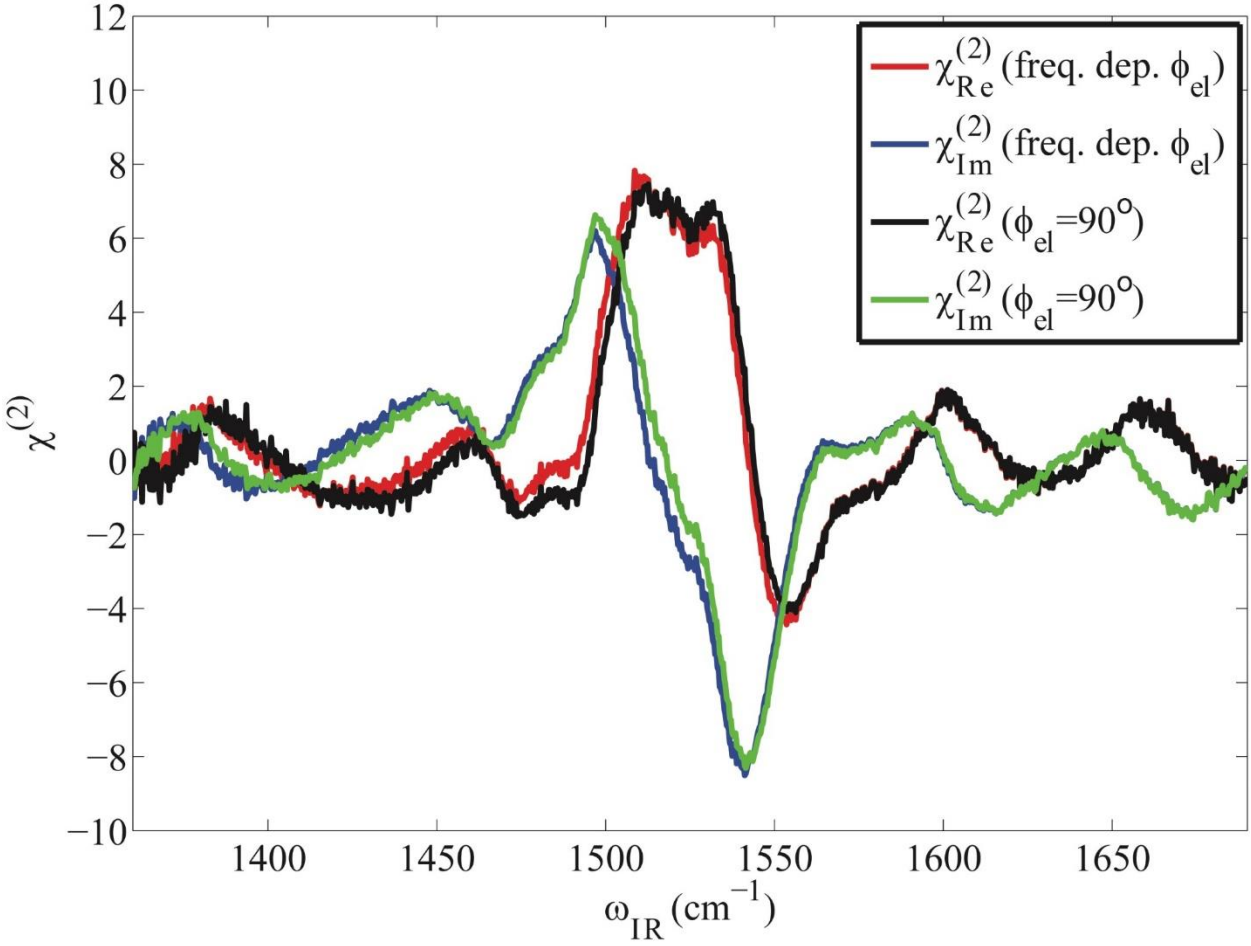

Figure 4.10 Complex $\chi^{(2)}$ spectra determined with the frequency dependent electronic phase determined from the UV-vis absorption spectrum (red and blue for real and imaginary $\chi^{(2)}$, respectively) and with a constant electronic phase of 90° (black and green for real and imaginary $\chi^{(2)}$, respectively).

References

(1) Nihonyanagi, S.; Mondal, J. A.; Yamaguchi, S.; Tahara, T. Structure and Dynamics of Interfacial Water Studied by Heterodyne-Detected Vibrational Sum-Frequency Generation. *Annu. Rev. Phys. Chem.* **2013**, *64*, 579−603.

(2) Stiopkin, I. V.; Jayathilake, H. D.; Bordenyuk, A. N.; Benderskii, A. V. Heterodyne-Detected Vibrational Sum Frequency Generation Spectroscopy. *J. Am. Chem. Soc.* **2008**, *130*, 2271−2275.

(3) Yamaguchi, S.; Tahara, T. Heterodyne-Detected Electronic Sum Frequency Generation: "Up" versus "down" Alignment of Interfacial Molecules. *J. Chem. Phys.* **2008**, *129*, 101102.

(4) Okuno, M.; Ishibashi, T. Heterodyne-Detected Achiral and Chiral Vibrational Sum Frequency Generation of Proteins at Air/ Water Interface. *J. Phys. Chem. C* **2015**, *119*, 9947−9954.

(5) Nihonyanagi, S.; Yamaguchi, S.; Tahara, T. Direct Evidence for Orientational Flip-Flop of Water Molecules at Charged Interfaces: A Heterodyne-Detected Vibrational Sum Frequency Generation Study. *J. Chem. Phys.* **2009**, *130*, 204704.

(6) Laaser, J. E.; Xiong, W.; Zanni, M. T. Time-Domain SFG Spectroscopy Using Mid-IR Pulse Shaping: Practical and Intrinsic Advantages. *J. Phys. Chem. B* **2011**, *115*, 2536−2546.

(7) Pool, R. E.; Versluis, J.; Backus, E. H. G.; Bonn, M. Comparative Study of Direct and Phase-Specific Vibrational Sum-Frequency Generation Spectroscopy: Advantages and Limitations. *J. Phys. Chem. B* **2011**, *115*, 15362−15369.

(8) Vanselous, H.; Petersen, P. B. Extending the Capabilities of Heterodyne-Detected Sum-Frequency Generation Spectroscopy: Probing Any Interface in Any Polarization Combination. *J. Phys. Chem. C* **2016**, *120*, 8175−8184.

(9) Rich, C. C.; Mattson, M. A.; Krummel, A. T. Direct Measurement of the Absolute Orientation of N3 Dye at Gold and Titanium Dioxide Surfaces with Heterodyne-Detected Vibrational SFG Spectroscopy. *J. Phys. Chem. C* **2016**, *120*, 6601−6611.

(10) Weiss, P. A.; Silverstein, D. W.; Jensen, L. Non-Condon Effects on the Doubly Resonant Sum Frequency Generation of Rhodamine 6G. *J. Phys. Chem. Lett.* **2014**, *5*, 329−335.

(11) Wu, D.; Deng, G.-H.; Guo, Y.; Wang, H. Observation of the Interference between the Intramolecular IR−Visible and Visible−IR Processes in the Doubly Resonant Sum Frequency Generation Vibrational Spectroscopy of Rhodamine 6G Adsorbed at the Air/ Water Interface. *J. Phys. Chem. A* **2009**, *113*, 6058−6063.

(12) Moad, A. J.; Simpson, G. J. A Unified Treatment of Selection Rules and Symmetry Relations for Sum-Frequency and Second Harmonic Spectroscopies. *J. Phys. Chem. B* **2004**, *108*, 3548−3562.

(13) Nagahara, T.; Kisoda, K.; Harima, H.; Aida, M.; Ishibashi, T. Chiral Sum Frequency Spectroscopy of Thin Films of Porphyrin J-Aggregates. *J. Phys. Chem. B* **2009**, *113*, 5098−5103.

(14) Raschke, M. B.; Hayashi, M.; Lin, S. H.; Shen, Y. R. Doubly-Resonant Sum-Frequency Generation Spectroscopy for Surface Studies. *Chem. Phys. Lett.* **2002**, *359*, 367−372.

(15) Covert, P. A.; Hore, D. K. Assessing the Gold Standard: The Complex Vibrational Nonlinear Susceptibility of Metals. *J. Phys. Chem. C* **2015**, *119*, 271−276.

(16) Sovago, M.; Vartiainen, E.; Bonn, M. Determining Absolute Molecular Orientation at Interfaces: A Phase Retrieval Approach for Sum Frequency Generation Spectroscopy. *J. Phys. Chem. C* **2009**, *113*, 6100−6106.

(17) Tian, C. S.; Shen, Y. R. Structure and Charging of Hydrophobic Material/water Interfaces Studied by Phase-Sensitive Sum-Frequency Vibrational Spectroscopy. *Proc. Natl. Acad. Sci. U. S. A.* **2009**, *106*, 15148−15153.

(18) Ward, R. N.; Davies, P. B.; Bain, C. D. Orientation of Surfactants Adsorbed on a Hydrophobic Surface. *J. Phys. Chem.* **1993**, *97*, 7141−7143.

(19) de Beer, A. G. F.; Samson, J.-S.; Hua, W.; Huang, Z.; Chen, X.; Allen, H. C.; Roke, S. Direct Comparison of Phase-Sensitive Vibrational Sum Frequency Generation with Maximum Entropy Method: Case Study of Water. *J. Chem. Phys.* **2011**, *135*, 224701.

(20) Fu, L.; Chen, S.-L.; Wang, H.-F. Validation of Spectra and Phase in Sub-1 cm^{-1} Resolution Sum-Frequency Generation Vibrational Spectroscopy through Internal Heterodyne Phase-Resolved Measurement. *J. Phys. Chem. B* **2016**, *120*, 1579−1589.

(21) Xiong, W.; Laaser, J. E.; Mehlenbacher, R. D.; Zanni, M. T. Adding a Dimension to the Infrared Spectra of Interfaces Using Heterodyne Detected 2D Sum-Frequency Generation (HD 2D SFG) Spectroscopy. *Proc. Natl. Acad. Sci. U. S. A.* **2011**, *108*, 20902−20907.

(22) Inoue, K.; Nihonyanagi, S.; Singh, P. C.; Yamaguchi, S.; Tahara, T. 2D Heterodyne-Detected Sum Frequency Generation Study on the Ultrafast Vibrational Dynamics of H_2O and HOD Water at Charged Interfaces. *J. Chem. Phys.* **2015**, *142*, 212431.

(23) Oostergetel, G. T.; van Amerongen, H.; Boekema, E. J. The Chlorosome: A Prototype for Efficient Light Harvesting in Photosynthesis. *Photosynth. Res.* **2010**, *104*, 245−255.

(24) Fujita, T.; Brookes, J. C.; Saikin, S. K.; Aspuru-Guzik, A. Memory-Assisted Exciton Diffusion in the Chlorosome Light-Harvesting Antenna of Green Sulfur Bacteria. *J. Phys. Chem. Lett.* **2012**, *3*, 2357−2361.

(25) Huh, J.; Saikin, S. K.; Brookes, J. C.; Valleau, S.; Fujita, T.; Aspuru-Guzik, A. Atomistic Study of Energy Funneling in the Light- Harvesting Complex of Green Sulfur Bacteria. *J. Am. Chem. Soc.* **2014**, *136*, 2048−2057.

(26) Vlaming, S. M.; Augulis, R.; Stuart, M. C. A.; Knoester, J.; van Loosdrecht, P. H. M. Exciton Spectra and the Microscopic Structure of Self-Assembled Porphyrin Nanotubes. *J. Phys. Chem. B* **2009**, *113*, 2273−2283.

(27) Wan, Y.; Stradomska, A.; Fong, S.; Guo, Z.; Schaller, R. D.; Wiederrecht, G. P.; Knoester, J.; Huang, L. Exciton Level Structure and Dynamics in Tubular Porphyrin Aggregates. *J. Phys. Chem. C* **2014**, *118*, 24854−24865.

(28) Friesen, B. A.; Nishida, K. R. A.; McHale, J. L.; Mazur, U. New Nanoscale Insights into the Internal Structure of Tetrakis(4-Sulfonatophenyl) Porphyrin Nanorods. *J. Phys. Chem. C* **2009**, *113*, 1709−1718.

(29) Rich, C. C.; McHale, J. L. Resonance Raman Spectra of Individual Excitonically Coupled Chromophore Aggregates. *J. Phys. Chem. C* **2013**, *117*, 10856−10865.

(30) Ohno, O.; Kaizu, Y.; Kobayashi, H. J-aggregate Formation of a Water-soluble Porphyrin in Acidic Aqueous Media. *J. Chem. Phys.* **1993**, *99*, 4128−4139.

(31) Leishman, C. W.; McHale, J. L. Light-Harvesting Properties and Morphology of Porphyrin Nanostructures Depend on Ionic Species Inducing Aggregation. *J. Phys. Chem. C* **2015**, *119*, 28167−28181.

(32) Rich, C. C.; McHale, J. L. Influence of Hydrogen Bonding on Excitonic Coupling and Hierarchal Structure of a Light-Harvesting Porphyrin Aggregate. *Phys. Chem. Chem. Phys.* **2012**, *14*, 2362.

(33) Akins, D. L.; Zhu, H.-R.; Guo, C. Aggregation of Tetraaryl- Substituted Porphyrins in Homogeneous Solution. *J. Phys. Chem.* **1996**, *100*, 5420−5425.

(34) Kano, H.; Saito, T.; Kobayashi, T. Dynamic Intensity Borrowing in Porphyrin J-Aggregates Revealed by Sub-5-Fs Spectroscopy. *J. Phys. Chem. B* **2001**, *105*, 413−419.

(35) Friesen, B. A.; Rich, C. C.; Mazur, U.; McHale, J. L. Resonance Raman Spectroscopy of Helical Porphyrin Nanotubes. *J. Phys. Chem. C* **2010**, *114*, 16357−16366.

(36) Dreesen, L.; Humbert, C.; Celebi, M.; Lemaire, J. J.; Mani, A. A.; Thiry, P. A.; Peremans, A. Influence of the Metal Electronic Properties on the Sum-Frequency Generation Spectra of Dodecanethiol Self-Assembled Monolayers on Pt (111), Ag (111) and Au (111) Single Crystals. *Appl. Phys. B: Lasers Opt.* **2002**, *74*, 621−625.

Chapter 5: HD-VSFG Comparison of Racemic- and Chiral-Prepared TSPP Thin Films

5.1 Introduction

The previous chapter discussed in detail the experimental results which demonstrate that HD-VSFG is a highly useful tool for investigation of the TSPP aggregate system. Briefly, heterodyne detection is advantageous because it preserves the complex phase information present in the VSFG signal, which is proportional to the second-order nonlinear susceptibility ($\chi^{(2)}$) of the system. Using these phase relationships and the known phase contributions of gold non-resonant SFG and of double resonance, it was shown that PPP polarization measures vibrational modes coupled with a delocalized TSPP aggregate exciton, whereas SSP polarization measures vibrations indicative of the TSPP monomer (Chapter 4). These observations were made by comparing the phase relationship between the complex real and imaginary components of the experimental HD-VSFG spectra.

5.2 Absorptive and Dispersive Features

Shown in **Figure 5.1** is a simplified HD-VSFG spectrum of a single resonant mode at 1550 cm^{-1} as well as the manner in which the real and imaginary components change when phase offsets are applied. Corresponding Argand diagrams are included with each simple spectrum, where plotting the intensities of the real and imaginary components on the x- and y-axes, respectively, illustrates the connection between phase offsets and the resulting features.

In a spectrum where no experimental phase offset has contributed, as depicted in Figure 5.1 (left), the imaginary component of $\chi^{(2)}$ is absorptive; that is, it peaks at the frequency of

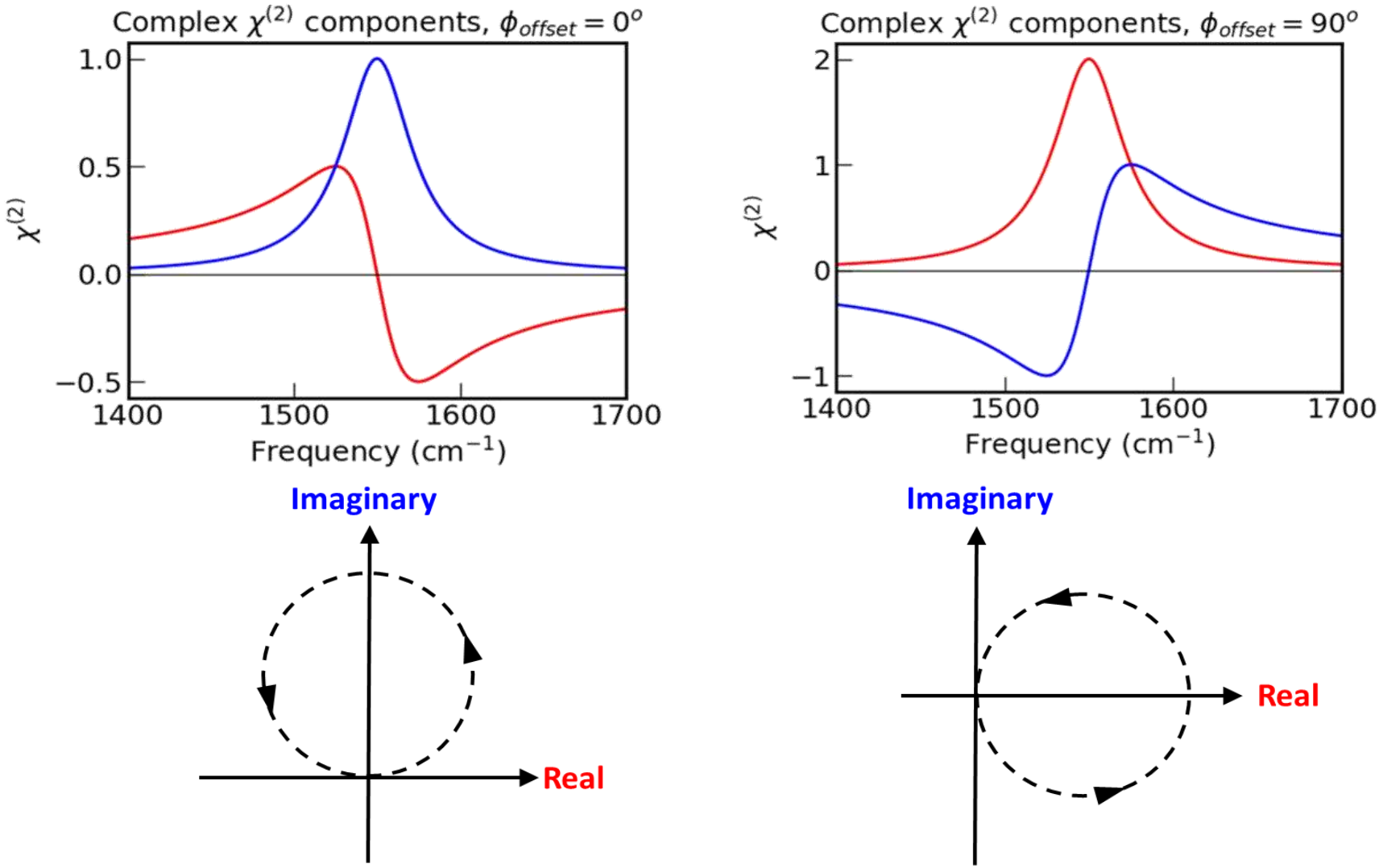

Figure 5.1 Simple HD-VSFG spectra (top) of a single vibrational mode at 1550 cm^{-1} with 0° and 90° phase offsets applied, with corresponding Argand diagrams (bottom). Real = red, blue = imaginary, black dashed =IR wavenumber.

vibrational resonance. In this manner, the imaginary component resembles a linear absorption spectrum. The real component is dispersive; it has a positive peak pre-resonant of the frequency of the vibrational mode, crosses zero at the resonance frequency, and peaks negatively in post-resonance frequencies. The complex features change upon a phase offset of 90°, as shown in Figure 5.1 (right). The real component is now absorptive and identical to the 0°-offset imaginary component. The imaginary component is now the inverse of the dispersive 0°-offset real component; features with this description will henceforth be referred to as inverse-dispersive. Phase offsets of 180° and 270° are shown in **Figure 5.2**. At 180°, the imaginary component is once again absorptive, but in the negative direction; features with this characteristic will henceforth be referred to as negatively-absorptive. The real component is again dispersive. At 270°, the imaginary component is dispersive and the real component is negatively-absorptive. These terms will be used to describe the complex features present in the following experimental HD-VSFG spectra.

5.3 Comparison of Racemic and Chiral Thin Films

This chapter presents further HD-VSFG results on the TSPP aggregate system. In this study, two TSPP thin films were studied: one prepared in the same way as previously studied films, and one prepared to be chiral. TSPP aggregates, due to their helical nature, are inherently chiral.[2,3] There is no preference for dextro- or levo-aggregates when they are prepared in the typical fashion.[4] However, it has been shown that stirring of the sample while aggregates form induces a reproducible handedness in the overall sample.[5] Thus, the two films were prepared to investigate potential differences between HD-VSFG spectra of racemic and chiral mixtures of

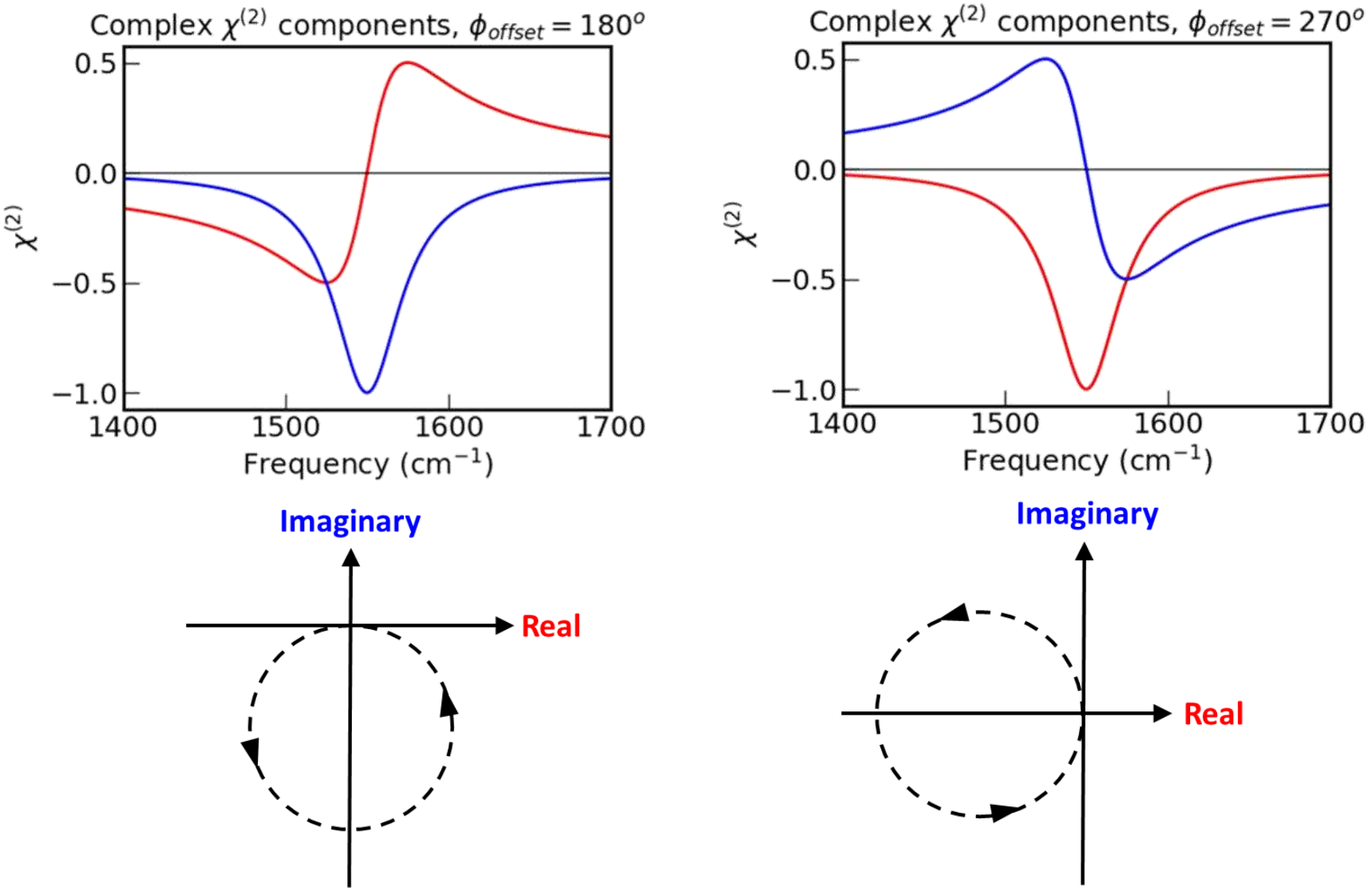

Figure 5.2 Simple HD-VSFG spectra (top) of a single vibrational mode at 1550 cm^{-1} with 180° and 270° phase offsets applied, with corresponding Argand diagrams (bottom). Real = red, blue = imaginary, black dashed =IR wavenumber.

the TSPP aggregates. In addition to the PPP and SSP polarizations used in the previous study, PSP polarization was also used. PSP is a chiral polarization scheme; it probes components of the $\chi^{(2)}$ tensor present only in chiral systems.[6]

Sample preparation for the thin films is detailed in Chapter 2. Both films were drop-cast onto the same gold mirror; a sample-free spot on the mirror was used as a reference. Experimental changes between spectral acquisitions were limited to moving the sample stage between the two films, and all spectra were acquired in succession to minimize outside contribution to differences in the spectra. All spectra were processed via the Fourier filtering method described in Chapter 2 using the custom Python code in Appendix A.

The resulting complex PPP, SSP, and PSP $\chi^{(2)}$ spectra of the racemic and chiral thin films are presented in **Figures 5.3-5**. For all $\chi^{(2)}$ spectra: $\chi^{(2)}_{Re}$ components are in red, $\chi^{(2)}_{Im}$ components are in blue, and $\left|\chi^{(2)}\right|^2$ are in dashed black. The spectra have multiple vibrational features, each of which can have a different phase and several of which overlap with each other. The resulting spectra are complicated and will require computational fitting to extract quantitative $\chi^{(2)}$ information. The spectra do, however, have distinct differences obvious by simple qualitative analysis. The $\left|\chi^{(2)}\right|^2$ spectra, which visually resemble more familiar linear absorption spectra, are included with their complex counterparts. While they do not have complex phase information, the peak locations in the $\left|\chi^{(2)}\right|^2$ spectra are helpful for analyzing each peak's behavior in the corresponding complex spectrum. Qualitative analysis was generally restricted to the most prominent features in each spectrum. While some smaller features are also included, it is worth noting that, even though many of the smaller features are visually obscured by neighboring stronger features, they are undoubtedly worth investigation with a more rigorous quantitative approach as they still contain valuable information on the system.

5.4 HD-VSFG Results & Discussion

In the complex TSPP PPP spectra (**Figure 5.3**), the 1551 cm^{-1} and 1567 cm^{-1} peaks in the racemic and chiral films, respectively, both display absorptive imaginary (Im) features and dispersive real (Re) features, suggesting that the phase of this vibrational mode is not affected by the sample chirality. The racemic film 1530 cm^{-1} mode appears to have a negatively-absorptive Im feature and an inversely-dispersive Re feature. The chiral film, on the other hand, has an approximately 1530 cm^{-1} shoulder with an absorptive Im feature and dispersive Re feature; at this mode, the two films are offset by a phase of 180°. The same is true for the racemic 1506 cm^{-1} and the chiral 1505 cm^{-1} modes. Finally, a strong 1487 cm^{-1} mode is seen in the chiral film with an absorptive Re feature and an inversely-dispersive Im feature. Unlike in the chiral film, the racemic counterpart mode at approximately 1483 cm^{-1} appears as a weak shoulder, but it does share the same apparent complex phase pattern. While this mode in the racemic sample is much weaker, its phase does not appear to differ from that seen in the chiral mode.

The complex SSP spectra are shown in **Figure 5.4**. In the SSP polarization, the vibrational features in the two $\left|\chi^{(2)}\right|^2$ spectra are very similar; the corresponding complex features, however, are not. Both the racemic and chiral films have a small peak at 1554 cm^{-1}, a peak which was also noted in the SSP spectrum in Chapter 4 as indicating a more monomer-like vibrational signature. While present in both films here, the complex 1554 cm^{-1} features differ: racemic shows an absorptive Im feature and a dispersive Re feature, while chiral shows a more obscured negatively-absorptive Re feature and inversely-dispersive Im feature, indicating a 180° phase difference between the two films. At 1525 cm^{-1}, the racemic peak corresponds to an absorptive Re feature and, though difficult to discern visually, likely a dispersive Im feature. The same mode in the chiral spectrum appears to have an absorptive Im feature and a dispersive Re

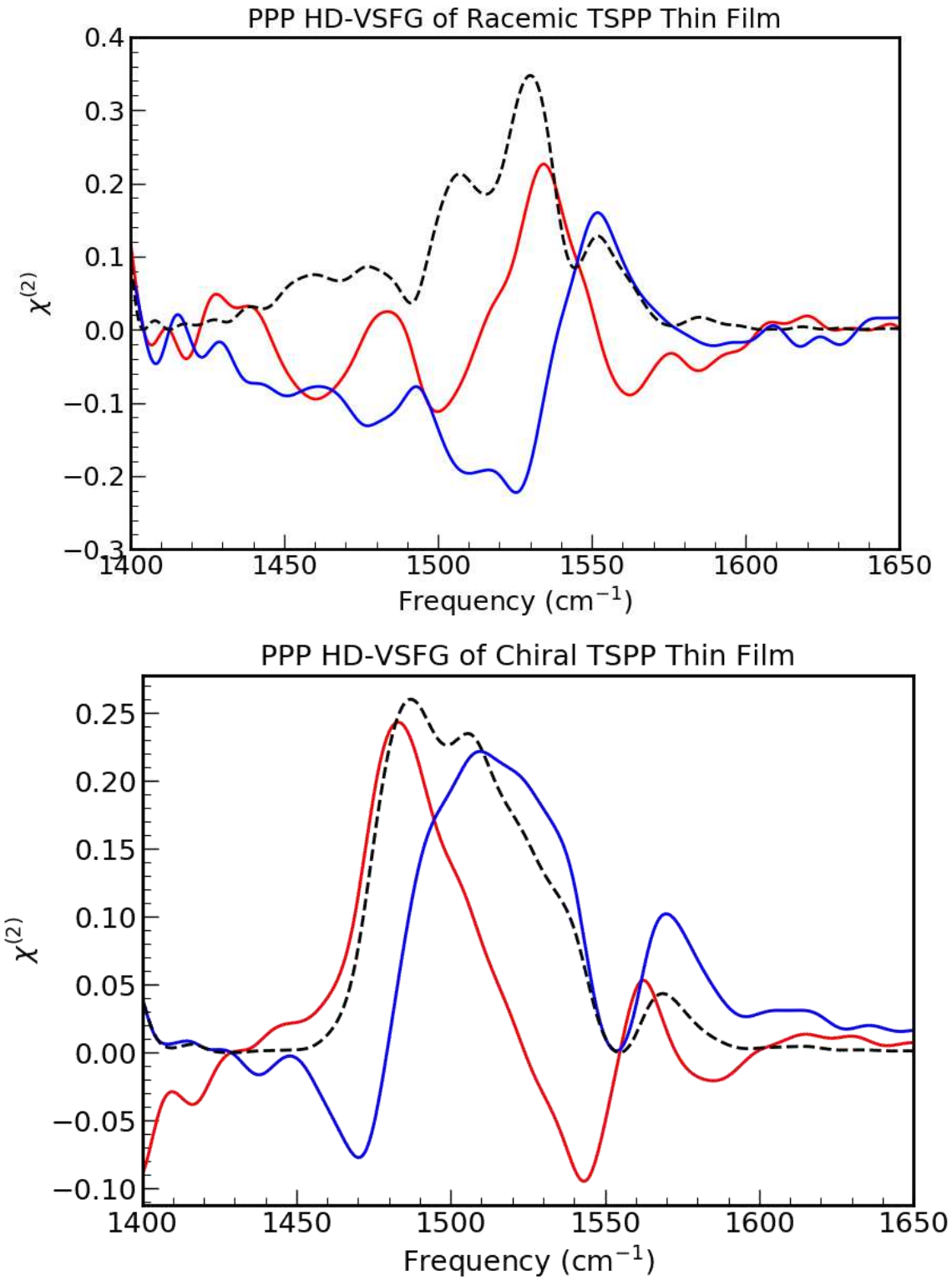

Figure 5.3 Complex PPP-polarized $\chi^{(2)}$ spectra of TSPP racemic (top) and chiral (bottom) thin films. Real component (red), imaginary component (blue). $|\chi^{(2)}|^2$ spectra are in black dashed lines and multiplied by a factor of 5 (top) and 4 (bottom) for clarity.

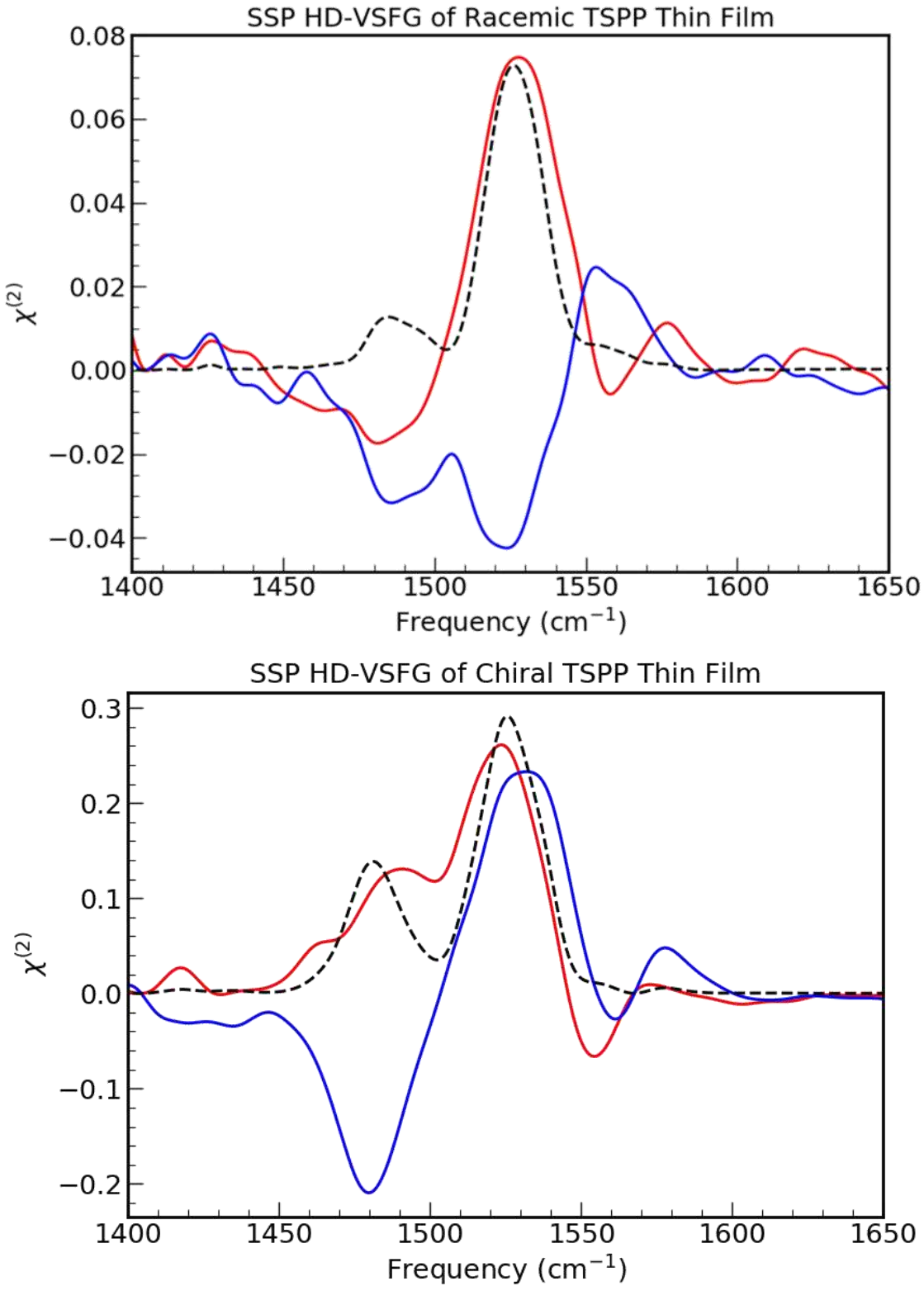

Figure 5.4 Complex SSP-polarized $\chi^{(2)}$ spectra of TSPP racemic (top) and chiral (bottom) thin films. Real component (red), imaginary component (blue). $|\chi^{(2)}|^2$ spectra are in black dashed lines and multiplied by a factor of 10 (top) and 2.5 (bottom) for clarity.

feature; this suggests that the 1525 cm^{-1} modes are offset 90° from each other in the racemic and chiral films. The 1493 cm^{-1} mode, which was also noted as vibrationally monomer-like in the previous chapter, is a weak shoulder in the racemic spectrum; its complex features are difficult to discern but are likely a negatively-absorptive Im feature and an inversely-dispersive Re feature. This mode is either not present in the chiral film or is hidden beneath a stronger neighboring mode. Lastly, the racemic and chiral spectra have modes at 1484 cm^{-1} and 1480 cm^{-1}, respectively. In this case, both modes appear to have negatively-absorptive Im features and inversely-dispersive Re features, indicating that the same phase offset contributes to this mode in both samples.

The complex PSP spectra are presented in **Figure 5.5**. Uniquely, there is a small peak in the chiral PSP spectrum at 1628 cm^{-1} which is not present in any other spectrum in this experiment, including in the PSP racemic spectrum. It shows a negatively-absorptive Im feature and a dispersive Re feature. There is IR vibrational activity in this region as shown in the ATR-FTIR in Chapter 3; this region is not, however, commonly investigated in Raman experiments, making it difficult to determine if there is a Raman-active mode at this frequency. This peak is worth further investigation to determine if it arises from error or artifacts in the data or if it is, in fact, genuine. Beyond this peak, the racemic and chiral PSP spectra are very similar. Both the racemic peak at 1570 cm^{-1} and the chiral peak at 1569 cm^{-1} display absorptive Re features and inversely-dispersive Im features. The middle prominent modes are the most different in terms of frequency: in the racemic sample there is a 1514 cm^{-1} peak while the chiral sample has a 1528 cm^{-1} peak. Upon closer inspection of the complex spectral features, additional modes obscured by these peaks can be discerned in both spectra. The racemic complex spectrum appears to have a contribution very close to 1528 cm^{-1}, the same frequency as the more

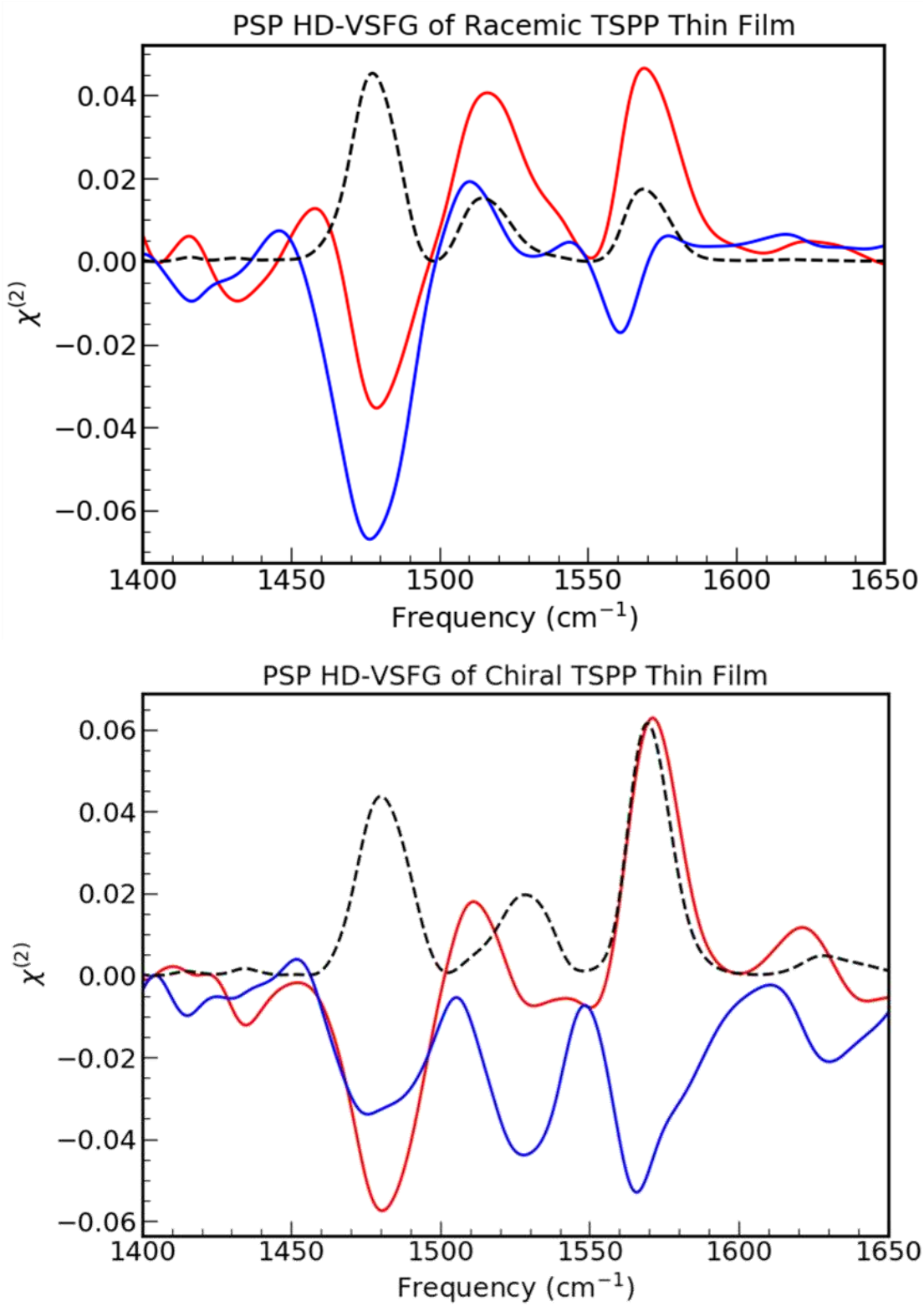

Figure 5.5 Complex PSP-polarized $\chi^{(2)}$ spectra of TSPP racemic (top) and chiral (bottom) thin films. Real component (red), imaginary component (blue). $|\chi^{(2)}|^2$ spectra are in black dashed lines and multiplied by a factor of 8 (top) and 10 (bottom) for clarity.

prominent peak in the chiral sample. Similarly, the complex chiral spectrum has a notable contribution at approximately 1512 cm^{-1}, comparable to the racemic 1514 cm^{-1} mode. Due to the closely-overlapping and relatively weak modes, it is impossible to determine with complete confidence the behavior of the complex components in these cases without quantitative analysis, but an attempt has been made by visual analysis. In both films, the 1528 cm^{-1} mode seems to have a negatively-absorptive Im feature and a dispersive Re feature. Likewise, the complex features seen in the 1512 cm^{-1} and 1514 cm^{-1} modes have absorptive Re features and dispersive Im features. Finally, the 1477 cm^{-1} racemic mode and the 1480 cm^{-1} chiral mode both have negatively-absorptive Re features and likely inversely-dispersive Im features, though the latter is difficult to discern.

In summary, the HD-VSFG spectra discussed here display notable differences in both vibrational mode location and complex phase. Aside from the highest-frequency modes, the PPP spectra appear to have similar vibrational modes, though they do vary in intensity. The phase of the lowest-frequency mode is the same in both the racemic and chiral films; the others, however, are offset by 180^{o} from each other. The SSP spectra have very similarly-located vibrational modes which also have similar intensities and resemble the monomer-like vibrational modes shown in the previous chapter. Between the two films, the lowest-frequency modes have the same phase while the others are all offset from each other. The PSP spectra are the most similar; each mode (apart from the unique 1628 cm^{-1} mode seen only in the chiral PSP spectrum) has a close counterpart in the opposing spectrum, and each pair seem to share the same phase.

5.5 Conclusion

These results indicate that PPP and SSP polarization schemes both report distinct differences between the phases of the vibrational modes in racemic- versus chiral-prepared thin films, whereas the PSP polarization scheme reports the same complex phases in the spectra of both films. In terms of vibrational mode location, best seen by comparison of the $\left|\chi^{(2)}\right|^2$ spectra in **Figure 5.6** (racemic film spectra in black and chiral in red), the SSP spectra are most like one another in comparison to other polarization schemes. The PSP spectra are also similar in the frequencies of their modes, although the two central modes differ significantly in intensity. The modes in the PPP spectra are the most different by visual analysis, particularly at the high- and low-frequency ends of the spectra.

It is not necessarily surprising that there should be differences between the HD-VSFG spectra of racemic- and chiral-prepared thin films of TSPP. Chiral HD-VSFG has been shown to detect a 180^o phase difference between the Im components observed in R- and S-BINOL $\chi^{(2)}$ spectra.[7] Furthermore, homodyne-detected chiral SFG has been used to distinguish between dextro- and levo-TSPP chirality in thin films prepared by addition of chiral tartaric acids, another method for producing aqueous chiral TSPP solutions.[8] These methods have not, however, reported a difference in vibrational mode frequencies or complex phases of individual modes between dextro and levo samples. To our knowledge, this is the first report of chiral HD-VSFG on TSPP aggregate thin films and presents new insights into the phase and structural sensitivity of this nonlinear technique. The $\chi^{(2)}$ tensor information present in these spectra will need to be extracted with a more rigorous computational fitting approach;[9] quantitative values for $\chi^{(2)}$, combined with aggregate modeling techniques, are the next step in deciphering the molecular structure of these aggregates and how phase is dependent on that structure. It will also be

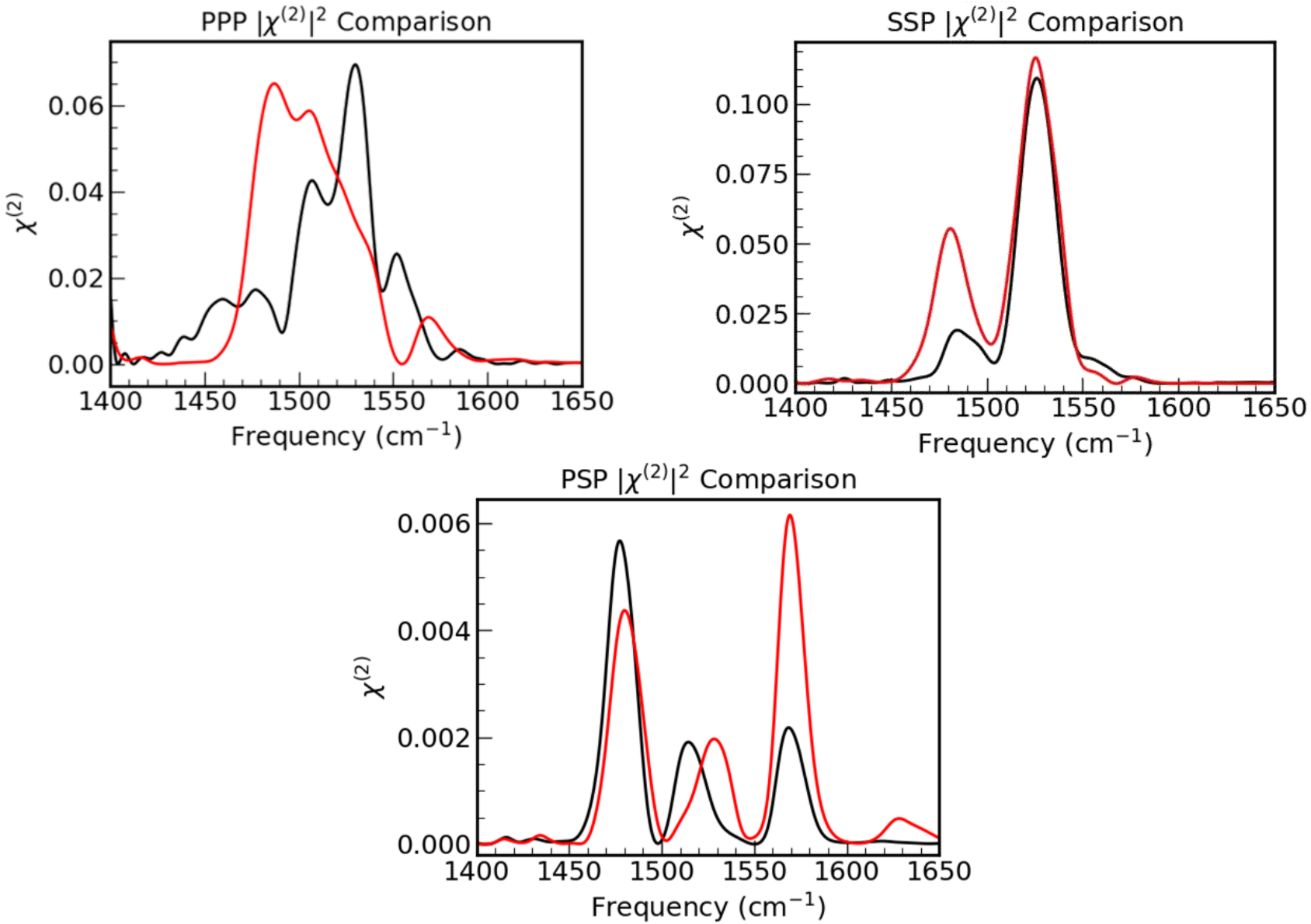

Figure 5.6 $|\chi^{(2)}|^2$ spectra of TSPP racemic (black) and chiral (red) thin films. SSP racemic spectrum multiplied by a factor of 15 for clarity.

important to repeat and expand this experiment. Stirring in the opposite direction has been shown to induce the opposite chirality in TSPP samples;[5] HD-VSFG of an oppositely-stirred chiral thin film should help to further the analysis started here. Further experimentation, modeling, and analysis is necessary to fully glean the useful information from these data; nevertheless, this study presents novel information on the sensitivity of HD-VSFG to chirality in TSPP thin films.

References

(1) Lambert, A. G.; Davies, P. B.; Neivandt, D. J. Implementing the Theory of Sum Frequency Generation Vibrational Spectroscopy: A Tutorial Review. *Appl. Spectrosc. Rev.* **2005**, *40*, 103–145.

(2) Rich, C. C.; McHale, J. L. Influence of Hydrogen Bonding on Excitonic Coupling and Hierarchal Structure of a Light-Harvesting Porphyrin Aggregate. *Phys. Chem. Chem. Phys.* **2012**, *14* (7), 2362.

(3) El-Hachemi, Z.; Escudero, C.; Acosta-Reyes, F.; Casas, M. T.; Altoe, V.; Aloni, S.; Oncins, G.; Sorrenti, A.; Crusats, J.; Campos, J. L.; et al. Structure vs. Properties — Chirality, Optics and Shapes — in Amphiphilic Porphyrin J-Aggregates. *J. Mater. Chem. C* **2013**, *1* (20), 3337.

(4) Rubires, R.; Farrera, J. a; Ribó, J. M. Stirring Effects on the Spontaneous Formation of Chirality in the Homoassociation of Diprotonated Meso-Tetraphenylsulfonato Porphyrins. *Chemistry* **2001**, *7* (2), 436–446.

(5) Ohno, O.; Kaizu, Y.; Kobayashi, H. J-Aggregate Formation Aqueous Media of a Water-Soluble Porphyrin in Acidic. *J. Chem. Phys.* **1993**, *99* (September), 4128.

(6) Yan, E. C. Y.; Wang, Z.; Fu, L. Proteins at Interfaces Probed by Chiral Vibrational Sum Frequency Generation Spectroscopy. *J. Phys. Chem. B* **2015**, *119* (7), 2769–2785.

(7) Okuno, M.; Ishibashi, T. A. Sensitive and Quantitative Probe of Molecular Chirality with Heterodyne-Detected Doubly Resonant Sum Frequency Generation Spectroscopy. *Anal. Chem.* **2015**, *87* (19), 10103–10108.

(8) Nagahara, T.; Kisoda, K.; Harima, H.; Aida, M.; Ishibashi, T. Chiral Sum Frequency Spectroscopy of Thin Films of Porphyrin J-Aggregates. *J. Phys. Chem. B* **2009**, 5098–5103.

(9) Vlaming, S. M.; Augulis, R.; Stuart, M. C. A.; Knoester, J.; Van Loosdrecht, P. H. M. Exciton Spectra and the Microscopic Structure of Self-Assembled Porphyrin Nanotubes. *J. Phys. Chem. B* **2009**, *113* (8), 2273–2283.

Appendix: Python Scripts

Codes used for processing linear and nonlinear spectral data were written in Python 3.6 using the Spyder integrated development environment (IDE) within Anaconda Navigator.

ATR-FTIR & UV-Vis Spectral Processing

Description: The linear processing code is used for simple linear spectroscopy data processing. Numpy and Pyplot (matplotlib.pyplot) Python libraries are required.

User specifies: linear spectroscopic technique, either 'IR' (FTIR) or 'UV' (UV-Vis); directory where sample file is located; name, including extension, of sample data file; and sample name to be used in figure title. Data is self-normalized and plotted with the appropriate units, "Frequency (cm^{-1})" for FTIR and "Wavelength (nm)" for UV-Vis.

FTIR data is assumed to have a comma delimiter; UV-Vis data is assumed to have four leading lines of experimental information that does not need to be loaded.

Linear processing code:

```
import numpy as np
import matplotlib.pyplot as plt

spec = 'UV' # Specify linear spectroscopy used to acquire data;  'IR' for FTIR or 'UV' for UV-Vis

directory = 'C:\\DataFolder\\' # Specify location of folder containing sample files

file = 'data.txt' # File name of sample txt file located in directory specified above, ex. 'data.txt'

name = 'Sample Name' # Name of sample for figure title, ex. 'TSPP pH 0.39'

def linear(spec, directory, file, name): # Define function to load and plot either FTIR or UV-Vis data
    if spec == 'IR':
        data = np.loadtxt(directory + file, delimiter = ',') # Load FTIR data
        data[:, 1] = data[:, 1] / max(data[: ,1]) # Normalize FTIR data
```

```
        plt.figure() # Plot normalized FTIR data
        plt.title(name + ' FTIR')
        plt.plot(data[:, 0], data[:, 1], 'k', linewidth = 1)
        plt.xlabel('Frequency $(cm^{-1})$')
        plt.ylabel('Normalized Absorbance')
        plt.minorticks_on()
        plt.show()

        return data

    if spec == 'UV':
        data = np.loadtxt(directory + file, skiprows=4) # Load UV-Vis data
        data[:, 1] = data[:, 1] / max(data[: ,1]) # Normalize UV-Vis data

        plt.figure() # Plot normalized UV-Vis data
        plt.title(name + ' UV-Vis')
        plt.plot(data[:, 0], data[:, 1], 'k', linewidth = 1)
        plt.xlabel('Wavelength (nm)')
        plt.ylabel('Normalized Absorbance')
        plt.minorticks_on()
        plt.show()

        return data

data = linear(spec, directory, file, name) # Run linear processing function according to
parameters set in first section
```

HD-VSFG Fourier Filtering

Description: The Fourier filtering code takes a raw HD-VSFG spectrum and returns a Fourier-filtered, reference-normalized, baseline-corrected complex χ^2 spectrum. Numpy and Pyplot Python libraries are required.

User specifies: directory where sample and reference data files are located; name, including extension, of sample and reference data files; sample and reference names to be used in figure titles; t_{min} and t_{max} for the Fourier filtering window; phase, ϕ_{offset}, to account for sample and reference phase offset; whether to display only sample figures or both sample and reference figures; and indices of the frequency points at which the spectrum is to be baseline corrected.

The Fourier filtering function plots: raw frequency-domain spectra; temporal interferograms with Fourier filtering windows; Fourier-filtered frequency-domain spectra; real components of the Fourier-filtered reference and sample spectra for visual phase comparison; pre-normalization absolute-square ($\left|\chi^{(2)}\right|^2$) spectra; normalized sample $\chi^{(2)}$ complex spectrum components; and normalized sample $\left|\chi^{(2)}\right|^2$ spectrum.

Spectra are typically first processed with a ϕ_{offset} of 0°; the appropriate ϕ_{offset} is determined by visual comparison of the filtered reference and sample spectra and re-processing of the data with adjusted values for ϕ_{offset} until phase alignment is reached. Baseline correction points are selected by inspecting the normalized spectra for two frequency points devoid of absorption features, then finding the corresponding indices in the x-axis array.

Fourier filtering code:

```
import numpy as np
import matplotlib.pyplot as plt
from numpy import pi

directory = 'C:\\DataFolder\\' # Specify location of folder containing sample and reference files

samplefile = 'Data.txt' # File name of sample txt file located in directory specified above, ex. 'data.txt'

samplename = 'Name of Sample' # Name of sample for figure titles, ex. 'TSPP PPP' or 'N3 on Gold'

reffile = 'Reference.txt' # File name of reference txt file located in directory specified above, ex. 'ref.txt'

refname = 'Reference Name' # Name of reference for figure titles, ex. 'Gold' or 'Quartz'

tmin = 3400 # Beginning of Fourier Filtering window in femtoseconds

tmax = 7200 # End of Fourier Filtering window in femtoseconds

phi = np.radians(0) # Phase (in degrees) for adjustment of offset between sample and reference filtered spectra
```

```
showref = 0 # Set as 0 to only plot figures for the sample; set as 1 to plot figures for both sample and reference

ilo = 951 # x-axis index for high-frequency baseline correction point

ihi = 93 # x-axis index for low-frequency baseline correction point

#%% Define Fourier filtering function

def rawFF(directory, samplefile, samplename, reffile, refname, tmin, tmax, phi, showref):

    spath = directory + samplefile # Set path for sample .txt data file

    sraw = np.loadtxt(spath, skiprows = 1) # Extract data from .txt file, excluding header row
    Nr1 = sraw.shape[0]
    Nc1 = sraw.shape[1]
    wn = np.zeros(shape = (Nr1, 1))
    wn = sraw[:, 0] # Set first column from raw data as wavenumber array

    if Nc1 % 2 == 0: # For data with an even number of rows
        sint = np.zeros(shape = (Nr1, int(Nc1 / 2)))
        sint = sraw[:, 1:Nc1:2] # Extract intensity columns from raw data

        sample = np.zeros(shape=(Nr1, ))
        sample = np.mean(sint, axis = 1) # Average sample intensity columns

    elif Nc1 % 2 == 1: # For data with an odd number of rows
        sint = np.zeros(shape = (Nr1, int(Nc1 - 1)))
        sint = sraw[:, 1:Nc1] # Extract intensity columns from raw data

        sample = np.zeros(shape = (Nr1,))
        sample = np.mean(sint, axis = 1) # Average sample intensity columns

    rpath = directory + reffile # Set path name for reference .txt data file

    rraw = np.loadtxt(rpath, skiprows = 1) # Extract data from .txt file, excluding headers
    Nr2 = rraw.shape[0]
    Nc2 = rraw.shape[1]

    if Nc2 % 2 == 0: # For data with an even number of rows
        rint = np.zeros(shape = (Nr2, int(Nc2 / 2)))
        rint = rraw[:, 1:Nc2:2] # Extract intensity columns from raw data

        ref = np.zeros(shape = (Nr2,))
        ref = np.mean(rint, axis = 1) # Average reference intensity columns
```

```
    elif Nc2 % 2 == 1: # For data with an odd number of rows
        rint = np.zeros(shape = (Nr2, int(Nc2 - 1)))
        rint = rraw[:, 1:Nc2] # Extract intensity columns from raw data

        ref = np.zeros(shape = (Nr2,))
        ref = np.mean(rint, axis= 1 ) # Average sample intensity columns

    plt.figure(samplename + ' 01') # Figure 1: Raw sample spectrum
    plt.title(samplename + ', Raw Spectrum')
    plt.plot(wn, sample, 'k', linewidth = 1)
    plt.xlabel('Frequency $(cm^{-1})$')
    plt.ylabel('Intensity')
    plt.minorticks_on()
    plt.show()

    if showref == 1: # Figure 2: Raw reference spectrum
        plt.figure(samplename + ' 02')
        plt.title(refname + ', Raw Spectrum')
        plt.plot(wn, ref, linewidth = 1)
        plt.xlabel('Frequency $(cm^{-1})$')
        plt.ylabel('Intensity')
        plt.minorticks_on()
        plt.show()

    # Compute time axis and FFT of sample and reference; return sample and reference temporal
interferograms

    dt = 1 / (((wn[0] - wn[1]) * 2.998e10) * (Nr1 - 1)) # Calculate spacing between time points

    t = np.zeros(Nr1,) # Generate time axis in femtoseconds according to number of sample points
    for n in range(0, Nr1):
            if Nr1 == 1024:
                t[n] = ((-511 * dt) + (n - 1) * dt) * (10**15)
            elif Nr1 == 1023:
                t[n] = ((-512 * dt) + (n - 1) * dt) * (10**15)

    sti = np.zeros(Nr1,)
    rti = np.zeros(Nr1,)
    sti = np.fft.fftshift(np.fft.fft(np.fft.ifftshift(sample))) # FFT sample data into time domain
    rti = np.fft.fftshift(np.fft.fft(np.fft.ifftshift(ref))) # FFT reference data into time domain

    #Set Fourier Filtering window, apply window to sample and reference time domain arrays,
IFFT filtered arrays back to frequency domain; return spectral interferogram and absolute square
plots
```

```
    ff = np.zeros(Nr1,) # Create array of ones between tmin and tmax and all else zeros
    for n in range(0, Nr1):
        if t[n] < tmin:
            ff[n] = 0
        elif t[n] > tmax:
            ff[n] = 0
        else:
            ff[n] = 1

    sff = np.zeros(Nr1,) # Apply Fourier Filtering window to sample and reference time domain
data
    rff = np.zeros(Nr1,)
    sff = sti * ff
    rff = rti * ff

    plt.figure(samplename + ' 03') # Figure 3: Plot sample temporal interferogram
    plt.title(samplename + ', Temporal Interferogram')
    plt.plot(t, ff * 30000, 'k', label = 'Filter Function')
    plt.plot(t, np.real(sti), 'r', label = 'Real')
    plt.plot(t, np.imag(sti), 'b', label='Imag')
    plt.xlabel('Time (fs)')
    plt.ylabel('Intensity')
    plt.legend()
    plt.minorticks_on()
    plt.show()

    if showref==1:
        plt.figure(samplename + ' 04') #Figure 4: Plot reference temporal interferogram
        plt.title(refname + ', Temporal Interferogram')
        plt.plot(t, ff * 150000, 'k', label = 'Filter Function')
        plt.plot(t, np.real(rti), 'r', label = 'Real')
        plt.plot(t, np.imag(rti), 'b', label = 'Imag')
        plt.xlabel('Time (fs)')
        plt.ylabel('Intensity')
        plt.legend()
        plt.minorticks_on()
        plt.show()

    sfilt = np.zeros(Nr1,) #Inverse FFT filtered sample and reference time domain data back to
frequency domain
    rfilt = np.zeros(Nr1,)
    sfilt = np.fft.ifftshift(np.fft.ifft(np.fft.fftshift(sff)))
    rfilt = np.fft.ifftshift(np.fft.ifft(np.fft.fftshift(rff)))

    plt.figure(samplename + ' 05') #Figure 5: Plot sample filtered spectral interferogram
    plt.title(samplename + ', Filtered')
```

```
    plt.plot(wn, np.real(sfilt), 'r', label = 'Real')
    plt.plot(wn, np.imag(sfilt), 'b', label = 'Imag')
    plt.xlabel('Frequency $(cm^{-1})$')
    plt.ylabel('Intensity')
    plt.legend()
    plt.minorticks_on()
    plt.show()

    if showref == 1:
        plt.figure(samplename + ' 06') # Figure 6: Plot reference filtered spectral interferogram
        plt.title(refname + ', Filtered')
        plt.plot(wn, np.real(rfilt), 'r', label = 'Real')
        plt.plot(wn, np.imag(rfilt), 'b', label = 'Imag')
        plt.xlabel('Frequency $(cm^{-1})$')
        plt.ylabel('Intensity')
        plt.legend()
        plt.minorticks_on()
        plt.show()

    sfilt = sfilt * np.exp(1j * phi) # Apply phase to account for ref and sample offset

    plt.figure(samplename + ' 07') # Figure 7: Plot Real Ref and Real Sample filtered spectra for
phase offset comparison
    plt.title(samplename + ', Ref and Sample Real phase comparison')
    plt.plot(wn, (np.real(rfilt) / max(abs(np.real(rfilt)))), 'k', label = 'Reference', linewidth = 0.75)
    plt.plot(wn, (np.real(sfilt) / max(abs(np.real(sfilt)))), 'g', label = 'Sample', linewidth = 0.75)
    plt.xlabel('Frequency $(cm^{-1})$')
    plt.ylabel('Intensity')
    plt.legend()
    plt.minorticks_on()
    plt.show()

    plt.figure(samplename + ' 08') # Figure 8: Plot sample absolute square spectrum
    plt.title(samplename + ', Absolute Square')
    plt.plot(wn, sfilt * np.conj(sfilt), 'k')
    plt.xlabel('Frequency $(cm^{-1})$')
    plt.ylabel('Intensity')
    plt.title(samplename + ', Absolute Square')
    plt.minorticks_on()
    plt.show()

    if showref == 1:
        plt.figure(samplename + ' 09') # Figure 9: Plot reference absolute square spectrum
        plt.title(refname + ', Absolute Square')
        plt.plot(wn, rfilt * np.conj(rfilt), 'k')
        plt.xlabel('Frequency $(cm^{-1})$')
```

```
        plt.ylabel('Intensity')
        plt.minorticks_on()
        plt.show()

    # Normalize sample spectrum to reference spectrum; return HDVSFG and Chi2^2 spectra

    norm = np.zeros(Nr1,) # Divide filtered sample spectrum by filtered reference spectrum
    norm = sfilt / rfilt

    plt.figure(samplename + ' 10') # Figure 10: Plot real and imaginary normalized HD-VSFG
spectrum components
    plt.title(samplename + ', HD-VSFG')
    plt.plot(wn, np.real(norm), 'r', label = 'Real')
    plt.plot(wn, np.imag(norm), 'b', label = 'Imag')
    plt.xlabel('Frequency $(cm^{-1})$')
    plt.ylabel('$\chi^{(2)}$')
    plt.legend()
    plt.minorticks_on()
    plt.show()

    plt.figure(samplename + ' 11') # Figure 11: Plot Chi2^2 spectrum
    plt.title(samplename + ', $|\chi^{(2)}|^2$')
    plt.plot(wn, abs(norm)**2, 'k', linewidth = 1)
    plt.xlabel('Frequency $(cm^{-1})$')
    plt.ylabel('$|\chi^{(2)}|^2$')
    plt.minorticks_on()
    plt.show()

    return wn, norm

def bascor(x, y, ilo, ihi): # Define baseline correction function. Input: x = x-axis array; y =
Fourier Filtered sample y-axis array; ilo = index in x array of low-frequency baseline correction
point; ihi = index in x array of high-frequency baseline correction point
    yr = np.real(y) # Separate y-array real and imaginary components
    yi = np.imag(y)

    mr = (yr[ihi]-yr[ilo])/(x[ihi]-x[ilo]) # Calculate slope of real linear fit
    mi = (yi[ihi]-yi[ilo])/(x[ihi]-x[ilo]) # Calculate slope of imaginary linear fit

    br = yr[ihi] - mr * x[ihi] # Calculate y-intercept of real linear fit
    bi = yi[ihi] - mi * x[ihi] # Calculate y-intercept of imaginary linear fit

    linr = mr * x + br # Calculate real linear fit
    lini = mi * x + bi # Calculate imaginary linear fit

    yr2 = yr - linr # Subtract real linear fit from real data
```

```
    yi2 = yi - lini # Subtract imaginary linear fit from imaginary data

    y2 = yr2 + 1j * yi2 # Recombine real and imaginary baseline-corrected data

    plt.figure()
    plt.title(samplename + ', Baseline Corrected HD-VSFG')
    plt.plot(x, np.real(y2), 'r', label = 'Real')
    plt.plot(x, np.imag(y2), 'b', label = 'Imag.')
    plt.xlabel('Frequency $(cm^{-1})$')
    plt.ylabel('$\chi^{(2)}$')
    plt.legend()
    plt.minorticks_on()
    plt.show()

    return y2

#%% Run Fourier filter function using parameters set in first section
x, y = rawFF(directory, samplefile, samplename, reffile, refname, tmin, tmax, phi, showref)

y = bascor(x, y, 951, 93) # Baseline correct using ihi and ilo parameters set in first section
```

List of Selected Abbreviations

AFM – atomic force microscopy

BBO – beta barium borate (BaB_2O_2)

CCD – charge-coupled device

CW – continuous wave

FFT – fast Fourier transform

FTIR – Fourier-transform infrared (spectroscopy)

FWHM – full width at half maximum

HD-VSFG – heterodyne-detected vibrational sum frequency generation (spectroscopy)

HOMO – highest occupied molecular orbital

LUMO – lowest unoccupied molecular orbital

MCT – mercury cadmium telluride (HgCdTe)

OPA – optical parametric amplifier/amplification

PPP – P-polarized SFG, P-polarized visible, P-polarized infrared

PSP – P-polarized SFG, S-polarized visible, P-polarized infrared

PRC – photosynthetic reaction center

SSP – S-polarized SFG, S-polarized visible, P-polarized infrared

STM – scanning tunneling microscopy

TEC – thermoelectric cooler

TSPP – tetra(4-sulfonatophenyl)porphyrin

UV-Vis – ultraviolet-visible (spectroscopy)